NASA/TM-20250003317

Test Results, Analysis, and Fluid and Structural Modeling of Noncontacting Finger Seals

Margaret P. Proctor, Maria A. Kuczmarski, James C. Johnston, and Amy R. Stalker
Glenn Research Center, Cleveland, Ohio

May 2025

NASA STI Program Report Series

Since its founding, NASA has been dedicated to the advancement of aeronautics and space science. The NASA scientific and technical information (STI) program plays a key part in helping NASA maintain this important role.

The NASA STI program operates under the auspices of the Agency Chief Information Officer. It collects, organizes, provides for archiving, and disseminates NASA's STI. The NASA STI program provides access to the NTRS Registered and its public interface, the NASA Technical Reports Server, thus providing one of the largest collections of aeronautical and space science STI in the world. Results are published in both non-NASA channels and by NASA in the NASA STI Report Series, which includes the following report types:

- TECHNICAL PUBLICATION.
  Reports of completed research or a major significant phase of research that present the results of NASA programs and include extensive data or theoretical analysis. Includes compilations of significant scientific and technical data and information deemed to be of continuing reference value. NASA counterpart of peer-reviewed formal professional papers but has less stringent limitations on manuscript length and extent of graphic presentations.

- TECHNICAL MEMORANDUM.
  Scientific and technical findings that are preliminary or of specialized interest, e.g., quick release reports, working papers, and bibliographies that contain minimal annotation. Does not contain extensive analysis.

- CONTRACTOR REPORT.
  Scientific and technical findings by NASA-sponsored contractors and grantees.

- CONFERENCE PUBLICATION.
  Collected papers from scientific and technical conferences, symposia, seminars, or other meetings sponsored or cosponsored by NASA.

- SPECIAL PUBLICATION.
  Scientific, technical, or historical information from NASA programs, projects, and missions, often concerned with subjects having substantial public interest.

- TECHNICAL TRANSLATION.
  English-language translations of foreign scientific and technical material pertinent to NASA's mission.

Specialized services also include organizing and publishing research results, distributing specialized research announcements and feeds, providing information desk and personal search support, and enabling data exchange services.

For more information about the NASA STI program, see the following:

- Access the NASA STI program home page at http://www.sti.nasa.gov

NASA/TM-20250003317

Test Results, Analysis, and Fluid and Structural Modeling of Noncontacting Finger Seals

Margaret P. Proctor, Maria A. Kuczmarski, James C. Johnston, and Amy R. Stalker
Glenn Research Center, Cleveland, Ohio

National Aeronautics and
Space Administration

Glenn Research Center
Cleveland, Ohio 44135

May 2025

This work was sponsored by the Advanced Air Vehicles Program
at the NASA Glenn Research Center.

Level of Review: This material has been technically reviewed by technical management.

This report is available in electronic form at https://www.sti.nasa.gov/ and https://ntrs.nasa.gov/

NASA STI Program/Mail Stop 050
NASA Langley Research Center
Hampton, VA 23681-2199

Test Results, Analysis, and Fluid and Structural Modeling of Noncontacting Finger Seals

Margaret P. Proctor, Maria A. Kuczmarski, James C. Johnston, and Amy R. Stalker
National Aeronautics and Space Administration
Glenn Research Center
Cleveland, Ohio 44135

Summary

The noncontacting finger seal (NCFS) is an advanced seal concept with potential to reduce specific fuel consumption in gas turbine engines by 2 to 3 percent with little to no wear of the seal or rotor. Static performance tests and bind-up tests of eight different NCFS configurations were conducted in air at pressure differentials up to 689.4 kPa and temperatures up to 922 K. Four of the seals tested were designed to have lift pads concentric to a herringbone-grooved rotor, which generates hydrodynamic lift when rotating. The remaining seals were tested with a smooth rotor; to create hydrodynamic lift during rotation, one seal had a circumferential taper, and one had an axial taper on the lift pad inner diameter (ID). The effects of the aft finger axial thickness and of the forward finger ID on leakage performance were investigated as well and compared to analytical predictions. Dynamic performance tests were conducted on four of the seals at 300 K. One seal was tested at a 69-kPa pressure differential at temperatures up to 922 K and surface speeds up to 366 m/s. Computational fluid dynamics (CFD) and structural models of this seal were validated by measured leakage performance and wear results, giving insight into the behavior and design considerations of NCFSs and their suitability for gas turbine engines with high overall pressure ratios.

Nomenclature

A	seal leakage area, m^2
C	radial clearance, mm
D_{seal}	outside diameter of the seal rotor, m
$\dot{m}$	air leakage flow rate, kg/s
P_u	air pressure upstream of seal, MPa
T_{avg}	average seal inlet air temperature, K
T_u	upstream air temperature, K
ΔP	pressure drop across seal, kPa
ϕ	flow factor, kg-$K^{0.5}$/MPa-m-s
$\phi_{leveled}$	leveled flow factor, kg-$K^{0.5}$/MPa-m-s
ϕ_{max}	maximum flow factor, kg-$K^{0.5}$/MPa-m-s

Introduction

Low-leakage, long-life seals have been an overarching goal for seals research at NASA Glenn Research Center for several decades. Over the years, gas turbine engine system studies have shown that use of advanced low-leakage seals has the potential to reduce specific fuel consumption by 2 to 3 percent and reduce direct operating costs (Ref. 1). In 2014, NASA's Aeronautics Advanced Air Transport

Technology Program identified technical challenges associated with high-overall-pressure-ratio (OPR) engines. One of those challenges was a noncontacting seal capable of 1,089 K for high-OPR engines. Early system studies indicated that the high-OPR engines would have a small core and that the pressure loads and temperatures would be substantially higher than current gas turbine engines. Further, the small core size meant leakage losses using current state-of-the art (SOA) seals would be a larger percentage of the primary flow, resulting in lower efficiency. Contacting seals such as brush seals and finger seals have leakage rates 50 percent lower than typical labyrinth seals, but they wear, generate frictional heating, and are limited to 922 K—at which brush seals exhibit bristle tip melting (Refs. 2 and 3). Furthermore, contacting seals are not practical because the rubbing contact generates heat that affects not only the seal, but also downstream components that are already near the limit of their temperature capability. Hence, a research effort to study low-leakage, long-life, high-temperature seals that focused on development of compliant, noncontacting designs was undertaken as part of the Compact Gas Turbine Subproject—Hot Section Materials. One of several compliant, noncontacting seal designs is the noncontacting finger seal (NCFS), which is the subject of this report.

Development of the NCFS can be traced back to 1998, when AlliedSignal patented the NCFS with hydrodynamic foot portion (Ref. 4) that has lift pads extending axially upstream and downstream from the forward and aft finger elements, respectively. In 2004, NASA patented a NCFS (Ref. 5) that has lift pads only extending axially downstream from the downstream fingers. With NASA support, the University of Akron did some analysis and ambient rig testing of the NCFS (Refs. 6 to 8) and subsequently patented a NCFS with lift pads extending from both forward and aft fingers in the downstream direction only (Ref. 9).

Preliminary testing of the NASA baseline NCFS on a herringbone-groove rotor at 300 K and 5,000 rpm demonstrated noncontacting operation at pressures from 14 to 241 kPa and no measurable wear after 93 min of rotation. During static testing, it was found that an excessive pressure differential caused the seal to bind the shaft (Ref. 10). A subsequent study was undertaken to investigate how certain geometry changes affect the leakage performance and the pressure differential capability of the NCFS. Both experimentation and computational fluid dynamics (CFD) and structural modeling were conducted to measure and predict leakage performance and the pressure differential capability of the NCFS designs. The results of the entire study, which concluded in September 2017, are documented in this report. The experimental research is presented first, and then the CFD and structural models, their results, and comparisons to experimental data are presented and discussed, followed by conclusions. A 2018 presentation highlights some results comparing performance test data to the CFD and structural models (Ref. 11).

Experimental Research

This report presents the bind-up and static performance test results of the NASA NCFS designs at 294, 533, 700, and 922 K inlet air temperature for eight different versions, or builds, of the seal (Ref. 12). In addition, dynamic leakage performance and wear results are presented for four builds of the seal for which dynamic testing was conducted. The purpose of the bind-up test was to ascertain the pressure differential at which the fingers deflect sufficiently to contact the rotor with enough load to make turning the rotor by hand difficult. Presumably, at this pressure differential contact, forces would likely result in unfavorable wear of the seal or rotor in a dynamic test. These results were considered when determining test conditions for dynamic testing. The initial room-temperature static performance tests provided a baseline leakage rate of the seal. This was used for comparison to subsequent room-temperature static performance tests run to assess if other tests changed the seal performance and hence the seal, whether from deformation due to high temperature or wear due to dynamic testing. Static tests at the higher

temperature levels provide data for comparison to other seal designs, although comparisons are not made in this report. Dynamic tests were conducted to assess the lift-off capability produced by hydrodynamic features of the seal designs and to measure the seal leakage performance over a range of surface speeds at pressure differentials relevant to advanced gas turbine engines.

Ideally, a well-performing NCFS would have seal leakage that is less than half that of a labyrinth seal and exhibit little to no hysteresis; that is, the leakage performance is consistent and independent of the sequence of pressure loading. Pressure applied to the seal generally moves the fingers radially inward. Hysteresis occurs when frictional forces within the seal prevent the fingers from moving until the pressure load is removed. As a result, the leakage performance curve when the pressure drop across the seal is increasing is greater than the leakage performance curve when the pressure drop is decreasing. In addition to low leakage, a well-performing NCFS would have little to no wear. Hydrodynamic features do require shaft rotation to generate lift-off forces, so some small amount of wear may result during rotation starts and stops. It is prudent to minimize pressure loads during rotation start and stop to reduce contact forces and wear, should contact occur. After the test hardware and apparatus and procedures are described, the static leakage performance test results are presented, discussed, and compared to analytical predictions. The static test results and discussion of the bind-up pressure, hardware inspections, and conclusions from static testing follow. Then the dynamic leakage performance and wear results are presented and discussed.

Test Hardware

Noncontacting Finger Seal Baseline Design

The NCFS baseline design (Figure 1) comprises forward (upstream) and aft (downstream) finger elements sandwiched between forward and aft spacers as well as front and back cover plates. The assembly is held together with 20 screws. Typical production finger seals would be fastened together by rivets ground flush with the front and back plates. Also, the back plate would typically be about the same thickness as the front plate. This seal was designed with a much thicker back plate to accommodate fastening components with screws so that different finger elements could be tested without replacing all the individual seal components.

The finger elements are thin washers with a series of curved slots all around the inner diameter (ID), which form the fingers. The two finger elements are oriented so that the fingers of one element cover the gaps between the fingers of the other element. The fingers act as cantilever beams, flexing in response to rotor dynamic motion and radial growth of the rotor due to centrifugal and thermal forces. This compliant feature permits operation at clearances much smaller than fixed-clearance seals, resulting in lower leakage rates.

The aft finger element has lift pads that extend axially downstream from each finger at the seal ID and that are concentric to the rotor at build. The lift pads ride above herringbone grooves on the outer surface of the rotor. Each lift pad has a circumferential groove on the ID (Figure 2). This groove defines the end of the seal land just upstream of it. The circumferential grooves, which create a flow path to the low-pressure region between the lift pads downstream of the aft finger stick, are assumed to be at low pressure. Thus, the portion of the lift pad downstream of the circumferential groove has low pressure on all four sides. The seal is positioned so that the upstream edge of the herringbone groove is located at the middle of the circumferential groove on the lift pad ID. During rotation, the grooves pump air inward towards the center of the lift pads to create a hydrodynamic lifting force to prevent contact with the rotor.

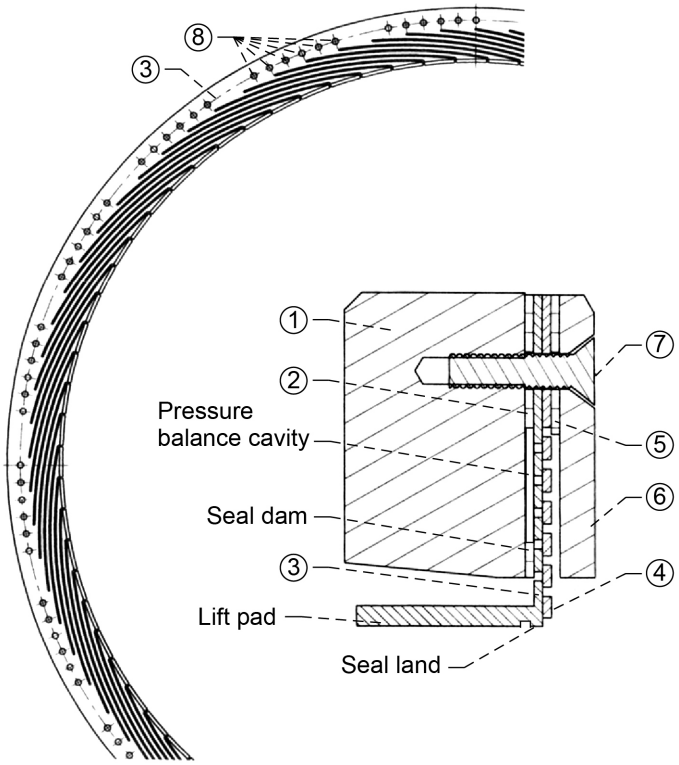

Figure 1.—Noncontacting finger seal design: 1, back plate; 2, aft spacer; 3, aft finger element; 4, forward finger element; 5, forward spacer; 6, front plate; 7, screw; 8, indexing and screw holes.

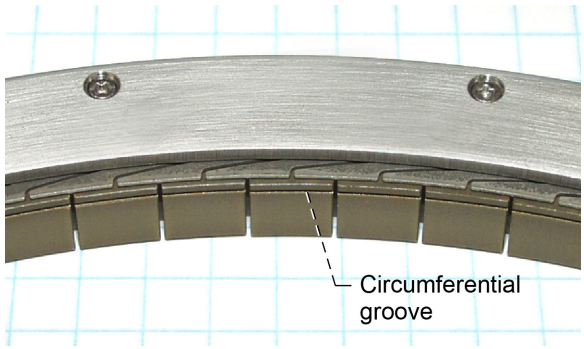

Figure 2.—NCFS ID, pretest.

Another difference between the forward and aft finger elements is that the high-pressure finger element has an ID that is 0.762 mm larger than the low-pressure finger element. This was done to ensure that the high-pressure finger element, which has no lift pads, would not touch the rotor due to pressure blowdown effects. Applying a pressure differential across a finger seal generates a suction force that draws the fingers inwards towards the rotor because of the lower pressure under the finger pads. It may be possible to reduce the high-pressure finger element ID to match the low-pressure finger element if there is sufficient friction between the two elements to keep them moving together. Evidence that this is the case can be found in References 6, 7, and 8.

The forward spacer extends radially inward from the outer diameter (OD) of the seal to the root of the finger stick. The aft spacer forms the pressure balance cavity between the aft finger element, the back plate, and seal dam. High-pressure air on the upstream side of the seal flows into the pressure balance cavity through a series of slots in the spacers and holes in the finger elements to counteract some of the axial pressure force on the fingers. The pressure balance cavity reduces the normal force, and hence the friction force, at the seal dam. This is essential to reducing hysteresis in the seal.

The NCFSs are made of Haynes-188, a solid-solution-strengthened superalloy, for operations at temperatures up to 1,089 K. The baseline design, Build 1, dimensions are shown in Table I, as well as the dimensions for the seven other builds.

Builds 2 to 7

The other builds were designed to test the effect of certain features on leakage performance and the range of conditions at which noncontacting operation is achieved. Specifically, Build 2 has a forward finger element that has nearly the same ID as the aft finger element. The Build 3 aft finger element has double the axial finger thickness than the baseline seal does. Build 4 combines the features of Builds 2 and 3. Build 5a is the baseline design, Build 1, on a smooth rotor. Build 5b is Build 3 on a smooth rotor. Two of the NCFS designs were tested on a smooth rotor and relied on hydrodynamic features in the lift pads to increase the pressure under the lift pads during rotation and prevent rubbing contact with the rotor. Specifically, Build 6 has a lift pad with a 0.0127-mm circumferential taper that creates a clearance that converges in the direction of rotation and Build 7 has a lift pad with a 0.0127-mm axial taper that converges with the axial direction of flow. Builds 6 and 7 do not have a circumferential groove. A graphical summary of Builds 1 to 7, shown in Figure 3, illustrates the differences between the builds. Because of wear that occurred in dynamic testing of Builds 2 and 3, new forward and aft finger elements were used for Build 4. These new elements were fabricated by a different manufacturer to the same specifications. However, one notable difference is that the new finger elements had visible milling machine marks on their faces, unlike the original finger elements used in static testing.

Test Rotors

The seal test rotors have an OD of 21.6 cm, nominally, and are made of Grainex Mar-M-247, a nickel-based superalloy with excellent high-temperature properties. The seal runner surface on the OD is coated with chrome carbide (CrC) applied by high-velocity oxygen fuel (HVOF) thermal spraying and ground to a 0.2 μm surface finish. The baseline NCFS design uses a rotor with herringbone grooves. The herringbone groove pattern (Figure 4) was machined by plunge electrical discharge machining (EDM) to a design depth of 0.0127 to 0.0254 mm. A pretest photo of the grooves is shown in Figure 5. Pretest inspection measurement with a profilometer shows the groove depth was 0.020 mm. The inspected diameters of the rotors are shown in Table I along with the resulting radial clearances for each build.

TABLE I.—KEY DIMENSIONS OF NONCONTACTING FINGER SEALS TESTED

NCFS build		Aft finger element			Finger pad	Forward finger element		Rotor		Radial clearance		Circumferential groove		
No.	Description	Inner diameter (ID), mm	Axial finger thickness, mm	Lift pad axial length at ID, mm	Circumferential length at ID, mm	ID, mm	Axial finger thickness, mm	OD, mm	Finish[a]	Aft, mm	Forward, mm	Depth, mm	Axial length, mm	Location from upstream edge, mm
1	Baseline	215.93	0.419	8.08–8.10	7.92	216.66–216.69	0.419	215.88	HB	0.024	0.3962	0.318	0.79	0.84
2	Baseline with same ID[b]	215.93	0.419	8.08–8.10	7.92	215.92	0.432	215.88	HB	0.024	0.0190	0.318	0.79	0.84
3	Baseline with 2× aft finger thickness	215.92	0.775	8.23	7.98[c]	216.66–216.69	0.419	215.88	HB	0.02	0.3962	0.356	0.76	1.14
4	Baseline with 2× aft finger thickness and same ID[b]	215.92	0.775	8.23	7.98[c]	215.92	0.432	215.88	HB	0.02	0.0190	0.356	0.76	1.14
5a	Build 1 on smooth rotor	215.93	0.419	8.08–8.10	7.92	216.66–216.69	0.419	215.9	Smooth	0.015	0.3873	0.318	0.79	0.84
5b	Build 3 on smooth rotor	215.92	0.775	8.23	7.98[c]	216.66–216.69	0.419	215.9	Smooth	0.0089	0.3873	0.356	0.76	1.14
6	0.0127-mm circumferential taper	215.91	0.394	8.23	7.98[c]	215.92	0.432	215.9	Smooth	0.0025	0.0102			
7	0.0127-mm axial taper -Upstream edge -Downstream edge	 215.91 215.88	0.394	8.23	7.98[c]	215.92	0.432	215.9 215.9 215.9	Smooth	 0.0025 –0.0102	0.0102			

[a]Rotor finish HB has herringbone grooves.

[b]Forward and aft finger elements have same ID.

[c]Calculated from $\frac{(\text{inspected ID})\pi}{81 \text{ fingers}}$ – (design gap between fingers of 0.41 mm).

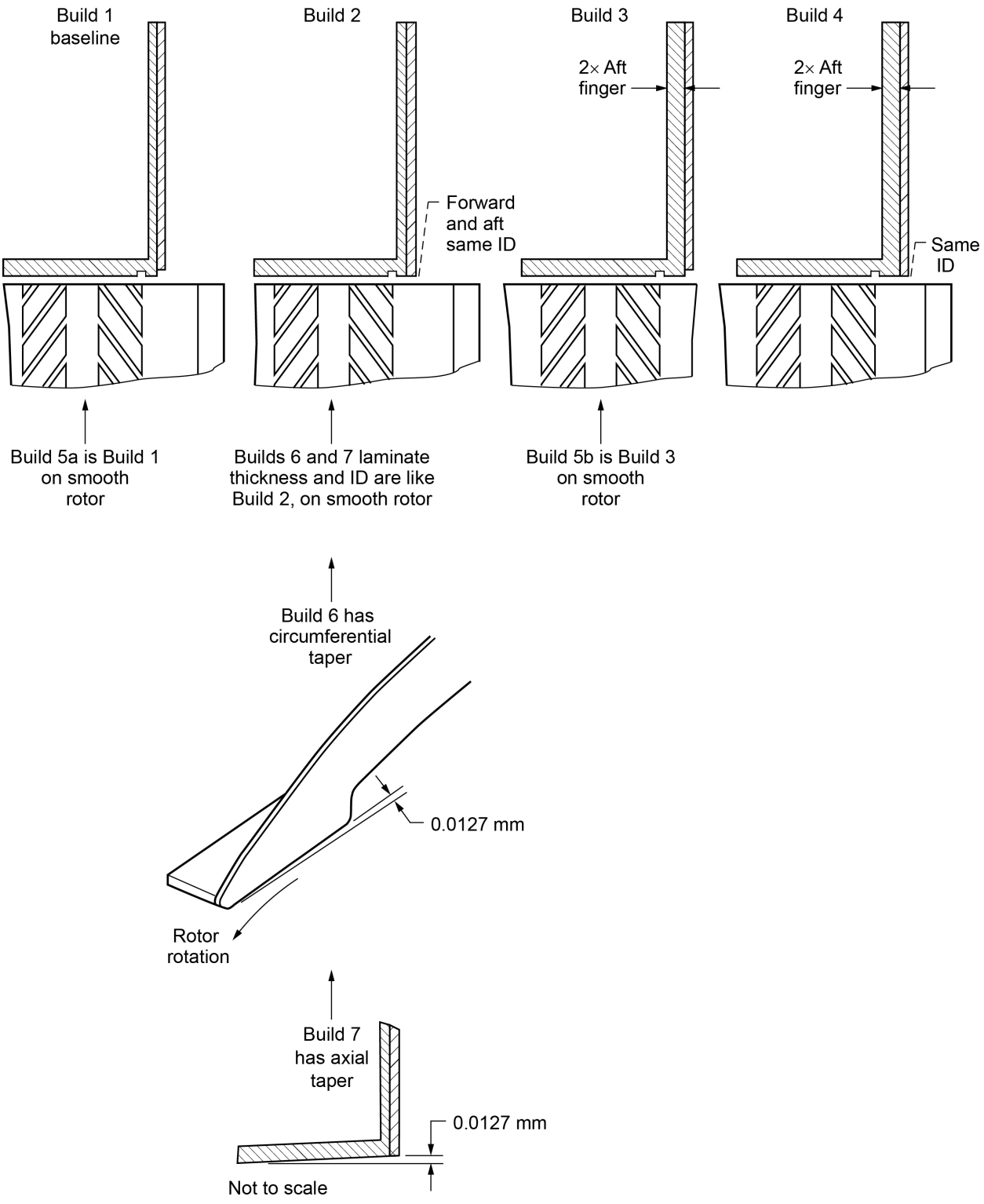

Figure 3.—Differences in NCFS Builds 1 to 7.

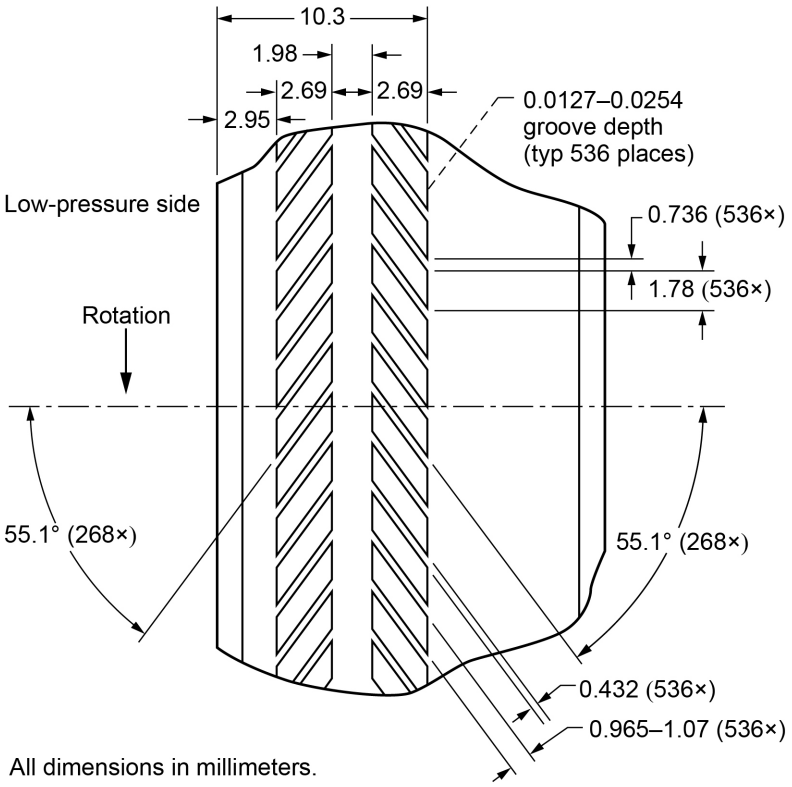

Figure 4.—NCFS herringbone groove design.

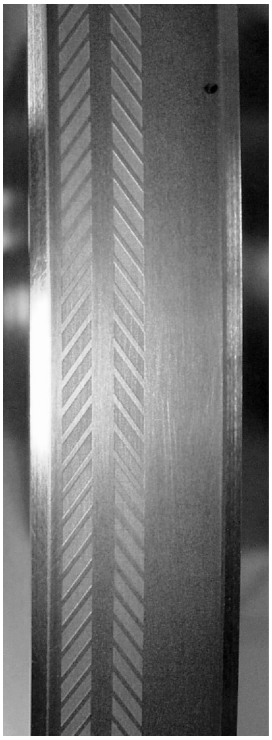

Figure 5.—Herringbone grooves on NCFS test rotor, pretest.

Flow Areas

In a simplified model of the NCFS to predict leakage rate (Ref. 10), three seal leakage flow paths were considered as shown in Figure 6. The first flow path goes from high pressure through the slots in the spacers and holes in the finger elements into the pressure balance cavity and then exits through the finger slots at the seal dam. The second flow path goes through the pinholes created by the high-pressure finger element ID, the rotor OD, and the circumferential gaps between the lift pads. The third flow path goes under the lift pads. The sum of the areas for each of these three flow paths equals the seal leakage area. The flow rate of each of these paths is a function of the pressure differential, flow area, and length of the flow path. From this perspective, the effect of dimensional differences between builds of the NCFS on flow areas and leakage rate are considered.

The axial length of the seal land on Builds 1 and 2 is 0.84 mm and on Builds 3 and 4 it is 1.14 mm. A longer seal land creates more resistance to the flow. Therefore, the flow under the lift pads (Flow 3) for Builds 3 and 4 should be less than it is for Builds 1 and 2 because of the longer seal land. Further, the radial clearance between the lift pad and rotor for Builds 3 and 4 is 6.4 μm smaller than it is for Builds 1 and 2, which should also result in lower leakage under the lift pads for Builds 3 and 4 than for Builds 1 and 2.

The pinhole leakage flow rate under the forward fingers and between the aft fingers (Flow 2) should be lower for Builds 2 and 4 than for Builds 1 and 3 since the radial clearances for the forward fingers are lower: 0.019 mm versus 0.3962 mm.

The radially inward flow rate through the slots between the fingers at the seal dam (Flow 1) should be greatest for Builds 3, 4, and 5b since the axial thickness of the aft fingers is approximately double that of Builds 1, 2, 5a, 6, and 7.

For each seal, the sum of the flow rates through these three flow paths is the total flow rate through the seal. The question is, which of these flow paths dominates? To address this, one can look at the areas and the percentage of the total areas. Table II shows the flow areas of the three different leakage paths at build. The areas at the seal dam are not expected to change when pressure is applied to the seal. However, the areas of the pinholes and under the lift pads will decrease because the resulting pressure differential draws the fingers radially inward. So, it is reasonable to assume the leakage flow rate will not be any less than the flow going through slots at the seal dam. Table III ranks the builds from highest to lowest flow areas. Assuming the finger pads remain concentric to the rotor, the fingers do not deflect downstream, and the herringbone grooves do not affect the static leakage rate, then one may expect the leakage performance of the builds to have the same ranking.

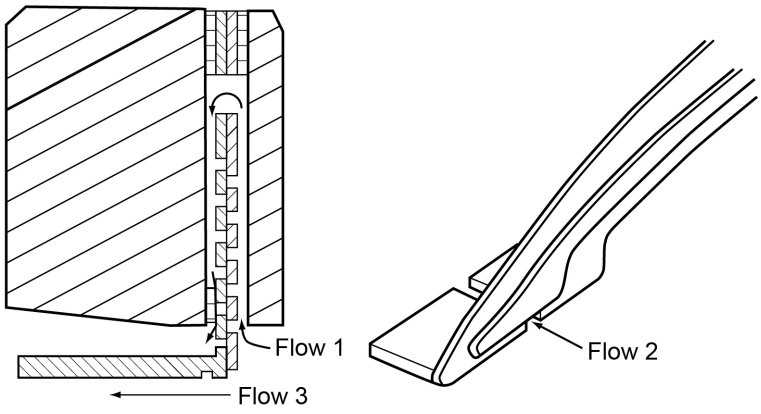

Figure 6.—Leakage flow paths included in simplified NCFS flow model of Reference 10.

TABLE II.—AS-BUILT FLOW AREAS OF NONCONTACTING FINGER SEALS TESTED

NCFS build		Flow areas, mm^2			Total flow area, mm^2
No.	Description	At seal dam	Pin holes	Under lift pads	
1	Baseline	13.8	13.0	15.6	42.4
2	Baseline with same ID[a]	13.8	0.6	15.6	30.0
3	Baseline with 2× aft finger thickness	25.5	13.0	11.5	50.0
4	Baseline with 2× aft finger thickness and same ID[a]	25.5	0.6	11.5	37.6
5a	Build 1 on smooth rotor	13.8	12.8	9.8	36.4
5b	Build 3 on smooth rotor	25.5	12.8	5.7	44.0
6	0.0127-mm circumferential taper	13.0	0.3	1.6	14.9
7	0.0127-mm axial taper	13.0	0.3	1.6	14.9

[a]Forward and aft finger elements have same ID.

TABLE III.—RANKING OF AS-BUILT FLOW AREAS OF NONCONTACTING FINGER SEALS TESTED

NCFS build	Total area at build, mm^2
3	50.0
5b	44.0
1	42.4
4	37.6
5a	36.4
2	30.0
6	14.9
7	14.9

Test Apparatus

Turbine Seal Test Rig

Testing was conducted in the NASA High-Temperature, High-Speed Turbine Seal Test Rig shown in Figure 7 and located at the NASA Glenn Research Center in Cleveland, Ohio. The turbine seal test rig consists of a 21.6-cm-diameter test rotor mounted on a shaft in an overhung configuration. The shaft is supported by two oil-lubricated bearings. A balance piston controls the axial thrust load on the bearings from the pressure loads on the test rotor. An air turbine drives the test rig. A torquemeter is located between the air turbine and the test rig and is connected to each by a quill shaft. The test seal is clamped into the Grainex Mar-M-247 seal holder as shown in Figure 8. A C-seal located at the holder-test seal interface prevents flow from bypassing the test seal at its OD. The seal holder is heated to approximately match the thermal growth of the rotor and prevent a damaging change in radial clearance. Heated, filtered air enters the bottom of the test rig and passes through an inlet plenum that directs the heated air axially toward the seal-rotor interface. The hot air either leaks through the test seal to the seal exhaust line or exits the rig before the test seal through a controlled bypass line at the top of the rig. If seal leakage is low, the bypass line must be open to maintain sufficient flow through the test rig to keep the rig hot.

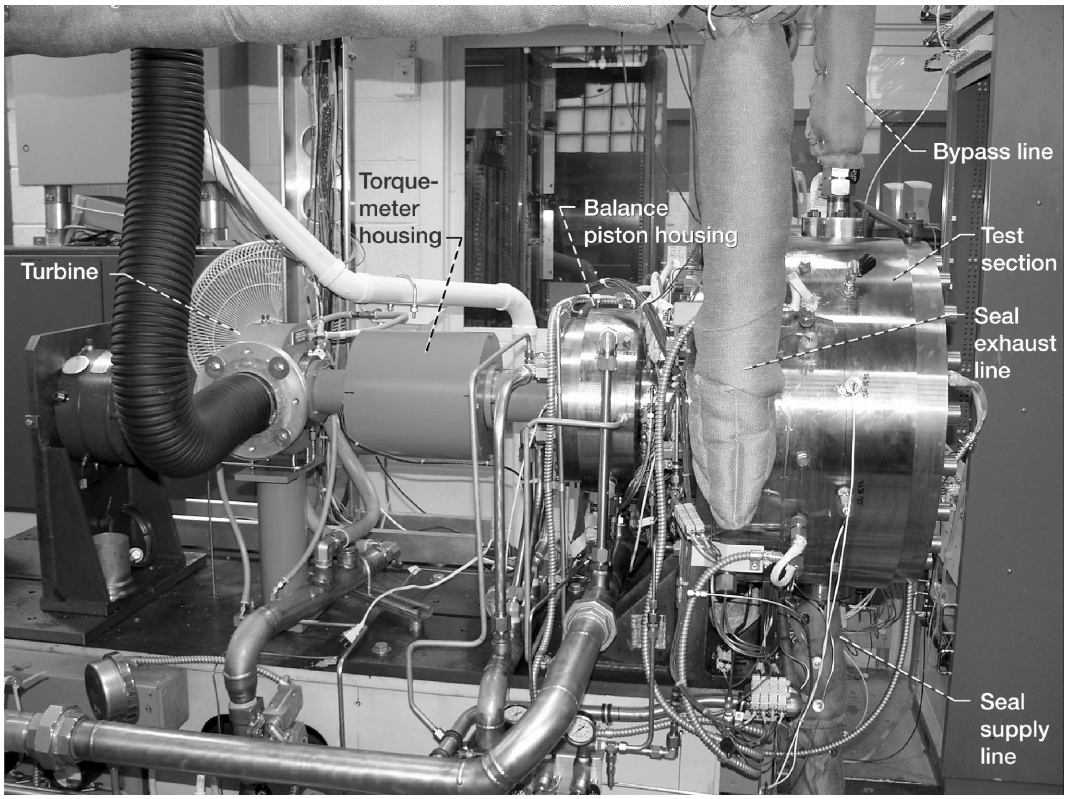

Figure 7.—High-Temperature, High-Speed Turbine Seal Rig.

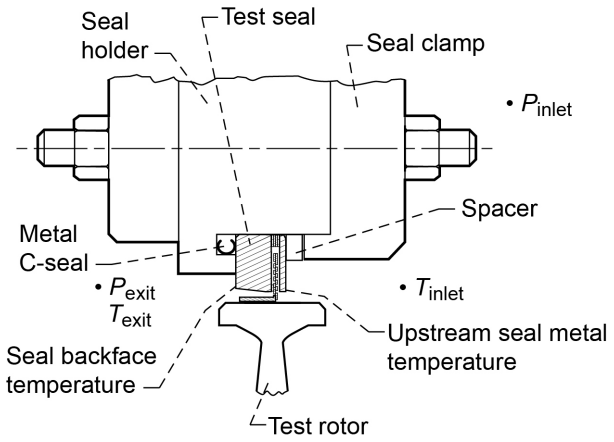

Figure 8.—Test seal configuration and location of research measurements.

Instrumentation

Seal inlet and exit temperatures (T) and static pressures (P), seal upstream metal temperature, and seal backface temperatures were measured at the locations shown in Figure 8. For each measurement there were three probes equally spaced around the circumference, except for the upstream seal metal temperature for which two thermocouples were located at the 90° and 180° positions (0° is top dead center). Type-K thermocouples with Inconel sheath were used. Those used to measure the seal inlet air temperature were 1.57 mm, closed ball, and those used to measure the seal exit air temperature

were 3.2 mm, closed ball. The thermocouples used to measure the seal metal and the seal backface temperatures were 1.57 mm, open ball.

Venturi flow meters were used to measure the flow rates of the hot air supplied to the rig and the air exiting the rig through the bypass line. The seal leakage rate $\dot{m}$ is the difference between these two flow measurements and is used to calculate the flow factor ϕ, which is defined as

$$\phi = \frac{\dot{m}\sqrt{T_{avg}}}{P_u \times D_{seal}} \tag{1}$$

where T_{avg} is the average seal inlet air temperature, P_u is the air pressure upstream of the seal, and D_{seal} is the outside diameter of the seal rotor. The flow factor can be used to compare the leakage performance of seals with different diameters and with different operating conditions. The accuracy of the measured flow factor is ±1.5 percent.

Test Procedure

The static test sequence for each build of the NCFSs was to conduct a room-temperature static test, bind-up test, repeat room-temperature static test, static test with bigger clearance, static test at 533 K, static test at 700 K, and static test at 922 K. This was the test sequence for Builds 1 to 4, 6, and 7. Only the room-temperature static test, bind-up test, and repeat room-temperature static test were conducted for Builds 5a and 5b. Dynamic tests were conducted on Builds 2, 7, 3, and 4, in that order. Dynamic tests consisted of a room-temperature lift-off test and a room-temperature performance test for each of these four builds. In addition, performance tests of the NCFS Build 4 were conducted at a 69-kPa pressure differential and 558 to 645 K and 700 K and 922 K, then at a 172-kPa pressure differential and 294 K.

Room-Temperature Static Test (Initial and Repeat)

At 0 rpm and in room-temperature air, data were recorded at pressure differentials across the seal of 0, 13.8, 27.6, 41.4, 55.2, 68.9, 103.4, 137.9, 172.4, 206.8, 275.8, 344.7, 413.7, 517, 552, 621, and 689.5 kPa. Each pressure condition was held for approximately 30 to 60 s. The pressure ramp up and down was repeated twice for a total of three cycles.

Bind-Up Test

The bind-up test was also conducted at room temperature. The end cap on the turbine drive was removed to access the drive shaft. Starting at 0 kPa across the seal and at incremental steps of 14 kPa, a wrench was placed on the turbine nut and used to check the ease of turning the shaft. Once the shaft became difficult to turn by hand, no further attempts were made to turn the shaft to prevent damage to the rotor coating and seal. The pressure was then increased to the maximum differential to record data at that condition. Then the pressure differential was decreased to 0 kPa. Data were recorded at each step of the pressure differential, and in some cases, data were continuously recorded throughout the test.

Static Test With Bigger Clearance

A static test with a bigger clearance was conducted by flowing ambient air to the seal at a constant pressure differential and turning on the heaters in the seal holder, thus changing the seal clearance. Data were continuously recorded but are not discussed in this report.

Static Tests at 533, 700, and 922 K

These tests were conducted in the same fashion as the room-temperature static tests, except that the inlet air temperature and seal holder temperature were set to 533, 700, and 922 K. It should be noted that the rig had to be heated to these conditions, which requires substantial air flow and time. Once test conditions were achieved, the pressure differential across the seal was reduced to zero and held for approximately 1 min to reset the seal before the test began. Doing this caused the inlet air temperature to drop approximately 28 to 56 K. The temperature recovered as the pressure drop across the seal increased. The actual temperature variation is noted in the results.

Room-Temperature Lift-Off Test

The purpose of the lift-off test was to determine if the hydrodynamic features of the seal prevented rubbing contact between the seal and the rotor. In this test, the pressure differential across the seal was set to 13.8 kPa, and then the shaft speed was quickly increased to 5,000 rpm while watching for a rapid increase in the seal backface temperature that would indicate rubbing contact. If a rapid temperature rise was observed, the speed was increased to 7,500 rpm and held for 30 s to reassess the seal backface temperature for evidence of rubbing contact. If lift-off was still not achieved, the speed was increased to 10,000 rpm and held for 30 s to again reassess if lift-off had occurred. If the seal backface temperatures indicated windage heating only, the speed was held constant for 5 min. Then the speed was quickly reduced to 0 rpm and the seal removed, inspected for wear indicating rubbing contact, and photographed. Data were continuously recorded during this test.

Room-Temperature Performance Test

While data were continuously recorded, the pressure differential across the seal was increased to 13.8 kPa. Then the speed was increased to the lift-off speed and then held for 30 s or until the temperature stabilized. Then the pressure differential was increased in 13.8 kPa increments to 138 kPa, holding for 30 s, or until temperatures stabilized, at each increment. In the event of a rapid temperature rise, the pressure differential would be decreased or the speed shut down. At 69 kPa the speed was cycled up and down three times obtaining about 1 min of data at each step of the following speeds: 0; 5,000; 10,000; 16,177; 20,000; 24,266; 30,000; 32,355; 35,000; and 40,444 rpm. While testing Build 2, a high-vibration turbine shutdown occurred on the first two speed cycles at approximately 38,000 and 40,000 rpm. On the third cycle, the maximum speed was reduced to 35,000 rpm to avoid a speed trip so the speed could be reduced in steps. At this point Build 2 was removed for inspection.

For Build 7, the room-temperature performance test at 69 kPa was conducted to maximum speeds of 32,500 rpm on cycle 1, 40,000 rpm on cycle 2 (when a high-vibration turbine shutdown occurred), and 38,000 rpm on cycle 3. The seal and test rotor were then removed for inspection and reinstalled. Next, the NCFS Build 7 was tested at 5,000 rpm, and the pressure differential was incrementally increased in small steps of 13.8 to 200 kPa, at which point the pressure differential was increased to 556 kPa because of operator error. While correcting the pressure differential back down to 138 kPa, a turbine shutdown occurred from a loss of tachometer signal. At this point, the pressure differential was reduced to zero, and the cover over the end of the turbine shaft was removed to verify that the shaft could still be turned by hand, which it could. Then operations resumed, and a 13.8-kPa pressure differential across the seal was applied and the speed was increased to 5,000 rpm. At that speed, the pressure differential was increased by several steps to 276 kPa and then back down by several steps to 13.8 kPa. Then speed was reduced to 0 rpm. The seal was then removed for inspection. Next, three speed cycles were conducted at 172 kPa. The procedure was to first set the pressure differential to 13.8 kPa and increase the speed to 5,000 rpm. Then the pressure differential was increased to 138 kPa and from there increased in 13.8 kPa steps to

172 kPa. Then the speed was increased and decreased in steps as before. In cycle 1, a high vibration caused a turbine shutdown at 38,000 rpm. In cycle 2, a maximum speed of 38,000 rpm was attained, and a high-vibration signal tripped a turbine shutdown while decreasing the speed to 32,500 rpm. Cycle 3 was conducted a week later, and the speed was successfully increased and decreased in steps to a maximum of 35,000 rpm. Next, three speed cycles were conducted at a 276-kPa pressure differential and maximum speed of 35,000 rpm. On cycles 1 and 2 while decreasing the speed, a low-oil-level alarm triggered a turbine shutdown. Cycle 3 was completed without any shutdowns. The seal and rotor were then removed for inspection.

For Build 3, the room-temperature performance test at 69 kPa was conducted as described above, except that on cycle 1, the maximum speed was 24,266 rpm because at that speed the seal backface temperature seemed high and it was decided to reduce speed and examine data before proceeding. Cycles 2 and 3 were conducted about 1 week later, with cycle 2 having a maximum speed of 25,000 rpm and a turbine shutdown. On cycle 3, the maximum speed was approximately 40,500 rpm, and a turbine shutdown occurred while decreasing speed at approximately 24,300 rpm because of a low-lubricant-level alarm.

At this point, issues with the lubrication system needed to be addressed, and several modifications were made to relieve operational difficulties.

Performance Tests for NCFS Build 4 With New Finger Laminates

The test sequence for the NCFS Build 4, with new finger elements fabricated by a different vendor, is different than the other builds tested. First, a room-temperature static performance test was conducted, followed by the lift-off test. Then a repeat room-temperature static test was conducted, followed by a room-temperature performance test at a 69-kPa pressure differential and two speed cycles between 5,000 and 30,355 rpm. Then the seal was checked for bind-up at pressure differentials of 69, 172, and 276 kPa. Next, a performance test was conducted at average inlet air temperatures from 558 to 645 K and a pressure differential of 69 kPa, with two cycles of increasing and decreasing speed incrementally between 5,000 and 32,355 rpm. The seal was removed for inspection and reinstalled. Then also at 69 kPa pressure differential, three speed cycles up and down between 0 and 32,355 rpm were conducted at 700 K and then at 922 K average seal inlet air temperatures. At this point the seal was removed for visual inspection and reinstalled. Next, a room-temperature performance test was conducted at a 172-kPa pressure differential. Speed was increased in steps as before to 20,000 rpm, at which point it appeared the seal backface temperature was increasing while speed was decreasing, so a quick decision was made to reduce speed to 10,000 rpm and then to 0 rpm. To try to assess the seal condition, one cycle of the room-temperature static performance test was conducted, and then one speed cycle from 0 to 32,355 rpm was conducted with a 69-kPa pressure differential across the seal. Then three speed cycles from 0 to 32,355 rpm were conducted with a 172-kPa pressure differential across the seal. The seal and rotor were then removed for inspection.

Static Test Results and Discussion

Leakage Performance at 294 K

A review of the initial room-temperature static performance test data revealed that the flow factor decreased with each cycle of pressure differential increasing and decreasing. It was also observed that the flow factors for each pressure differential increase/decrease cycle in the repeat room-temperature static test were in much better agreement compared to the initial test. Presumably, this is the result of the pressure cycles and hand rotation during the bind-up test helping the fingers to move into better position. Consequently, the initial room-temperature performance test results are not presented.

The repeat room-temperature static performance test results are shown in Figure 9 to Figure 16 for Builds 1, 2, 3, 4, 5a, 5b, 6, and 7, respectively, which show the measured flow factor as a function of the pressure drop across the seal. In all cases, there is hysteresis between the increasing and decreasing pressure differential portions of each cycle. The flow factor is higher when the pressure is being increased than when it is being decreased. This is because the pressure pushes the seal closed, and frictional forces hold it in that position. The pressure differential must be reduced to zero to release the seal position. Note that the flow factors level out at pressure differentials above approximately 90 kPa, which indicates choked flow.

Table IV shows the measured maximum flow factor and the value at which it levels out for each build and inlet air temperature. For all builds, the flow factor increases with increased average seal inlet air temperature. This is due to the seal material having a higher coefficient of thermal expansion than the rotor material, which results in the radial seal clearance increasing with temperature. For example, if the seal-rotor interface was a line-to-line fit at 215.9 mm (8.5 in.) diameter at 294 K (70 °F), a temperature increase to 700 K (800 °F) would result in 0.0356 mm (0.0014 in.) of radial clearance.

Comparing the repeat room-temperature flow factors for each build results in the following ranking of the builds from highest to lowest maximum flow factor: 3, 7, 5a, 6, 5b, 1, 2, and 4. This does not match the ranking of the flow areas shown in Table III. The ranking of builds from highest to lowest leveled flow factor is 5a, 1, 5b, 3, 2, 7, 4, and 6, which also does not match the ranking of the flow areas in Table III. This means flow areas in the seal are different from the build geometry when pressure is applied. It is known from previous studies of finger seals that the fingers draw in towards the rotor when pressure is applied. Further, pressure loads may cause the fingers to deflect axially. Both deflections would change the flow areas and affect the concentricity of the lift pads to the rotor.

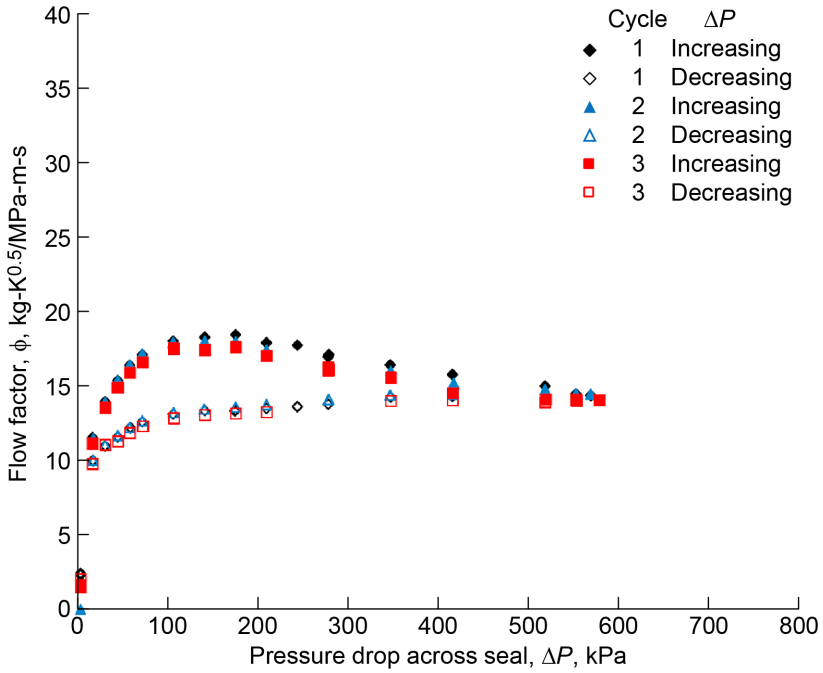

Figure 9.—Static leakage performance of baseline NCFS Build 1 at 276 to 294 K average inlet air temperature.

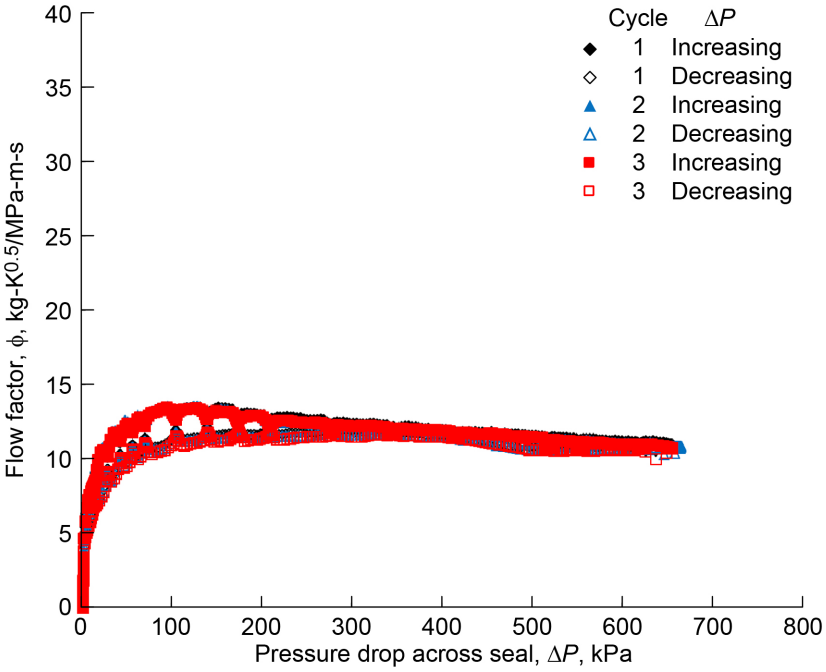

Figure 10.—Static leakage performance of NCFS Build 2 at 297 to 299 K average inlet air temperature.

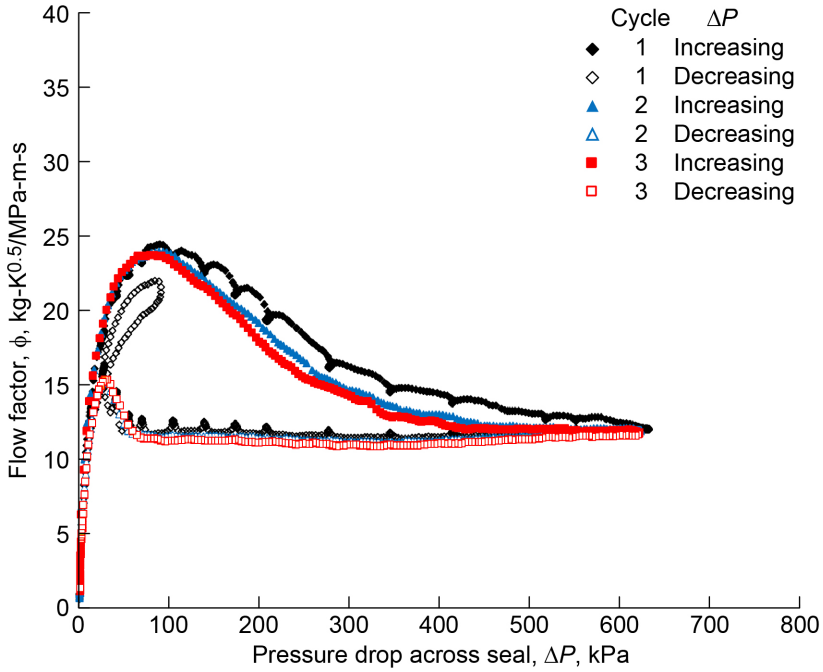

Figure 11.—Static leakage performance of NCFS Build 3 at 301 to 303 K average inlet air temperature.

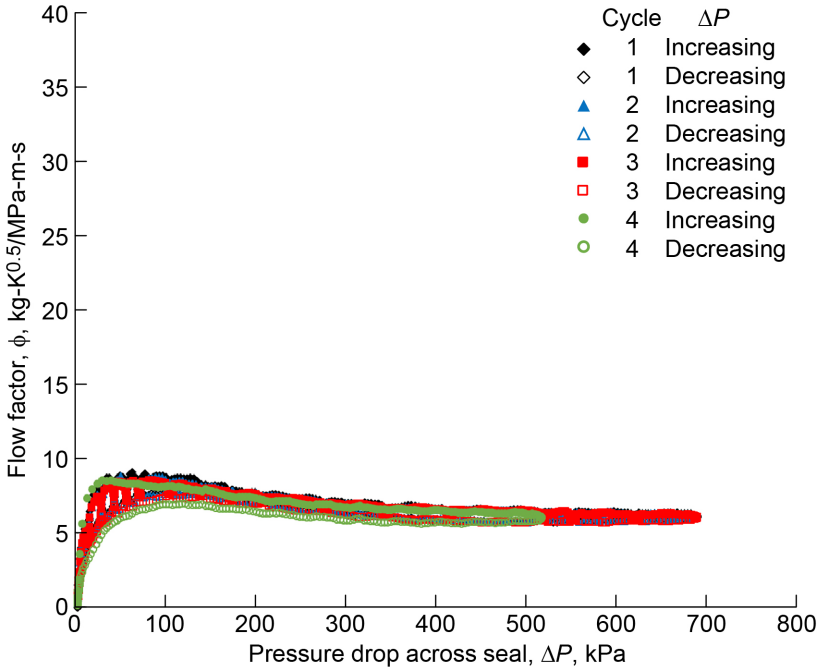

Figure 12.—Static leakage performance of NCFS Build 4 at 303 to 304 K average inlet air temperature.

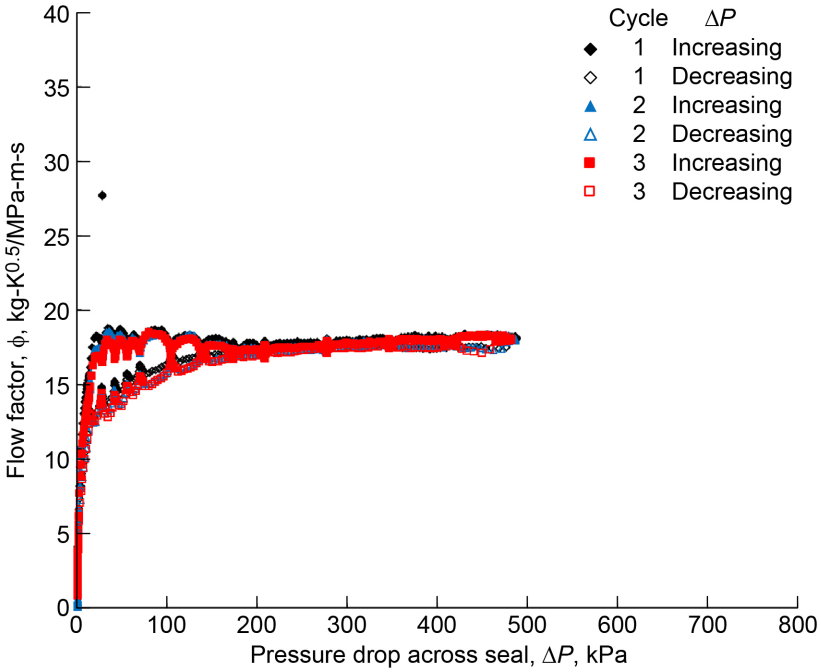

Figure 13.—Static leakage performance of NCFS Build 5a at 280 to 292 K average inlet air temperature.

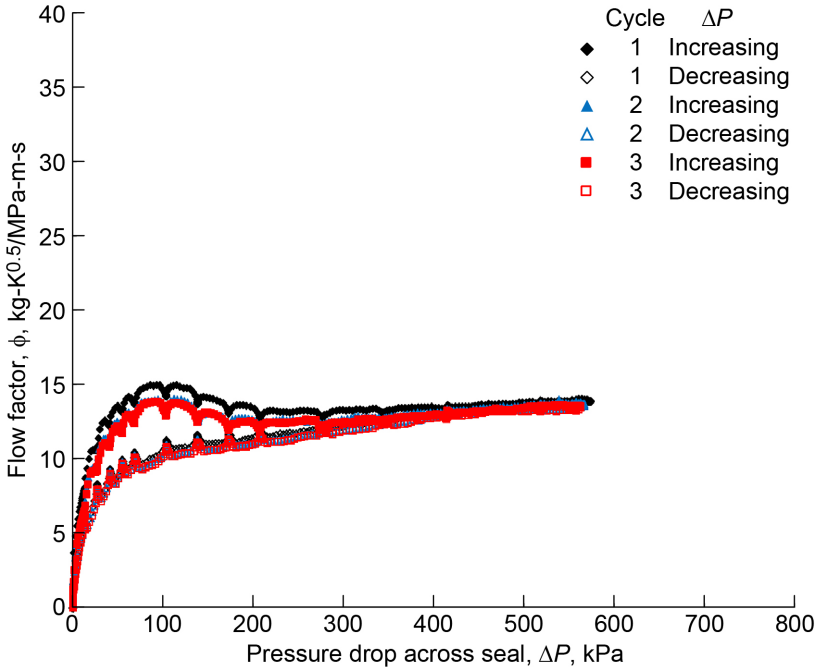

Figure 14.—Static leakage performance of NCFS Build 5b at 282 to 289 K average inlet air temperature.

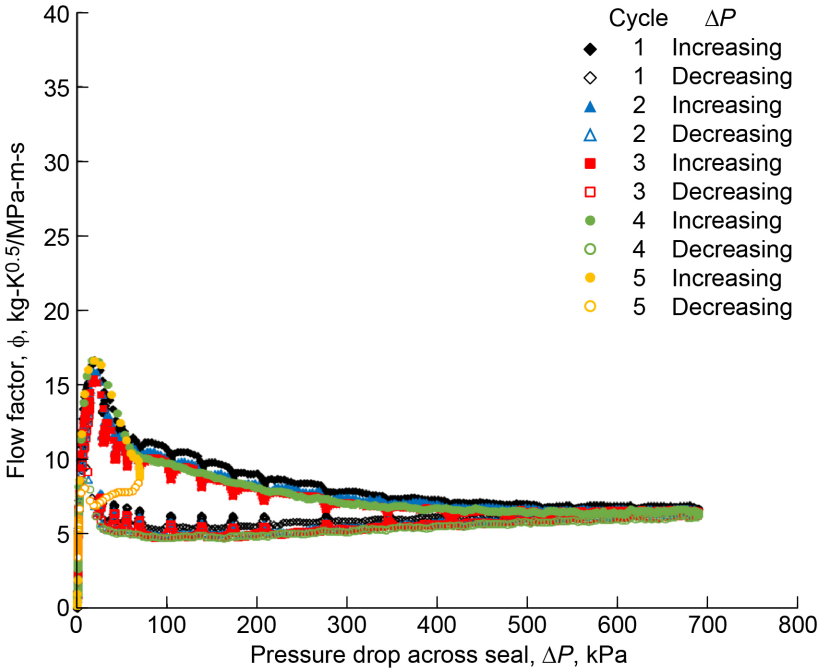

Figure 15.—Static leakage performance of NCFS Build 6, with circumferential taper, at 283 to 294 K average inlet air temperature.

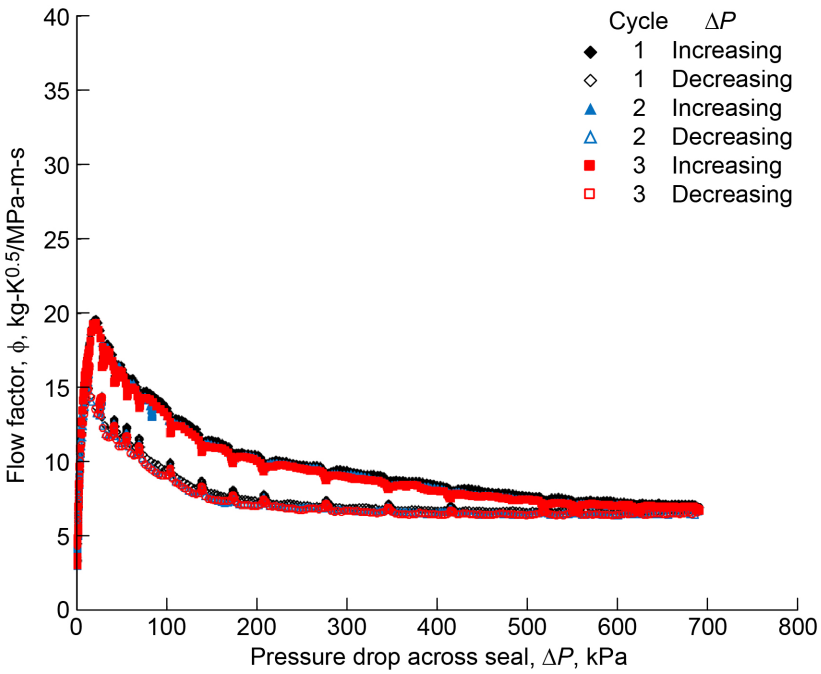

Figure 16.—Static leakage performance of NCFS Build 7, with axial taper on lift pad, at 275 to 298 K average inlet air temperature.

Comparison of Builds 1 and 2 seal leakage performance (Figure 9 and Figure 10, respectively) shows the effect of blocking the pinholes between the aft fingers; as expected, the flow factor for Build 2 is less than that of Build 1. Also, Build 2, which nearly completely blocks the gaps between the aft fingers, has less hysteresis than Build 1. Similarly, by comparing Figure 11 and Figure 12, one can see that Build 4, which also nearly completely blocks the gaps between the aft fingers, has lower leakage and less hysteresis than Build 3.

The effect of the axial thickness of the aft finger on leakage performance can be seen by comparing the leakage performance of Build 3 to Build 1 (Figure 11 and Figure 9, respectively). Build 3, which has an axial aft finger thickness nearly twice that of Build 1, shows much more leakage and hysteresis at the lower pressure differentials. However, for decreasing pressure differential, the Build 3 flow factor was less than that measured for Build 1. In Figure 11, the peak at ~35 kPa when decreasing the pressure differential for Build 3 is of particular interest. Also, the loop in cycle 2 resulted from an operator error that increased pressure differential when it should have been further decreased. Having an aft finger axial thickness nearly double that of Build 1, the Build 3 aft finger radial stiffness is twice that of Build 1, and the axial stiffness is 8 times greater. This greater finger stiffness may explain the Build 3 behavior. As pressure is first applied, the higher stiffness of Build 3 fingers would more greatly resist the pressure closing force than Build 1 and would result in higher flow factors. Once the pressure load moves the fingers to their closed or bound positions, frictional forces hold them in place. When the pressure is then decreased to the point that frictional forces are overcome, the higher spring rate of the finger causes a greater opening of the seal. The lower flow factor with decreasing pressure differential may be attributed to the smaller radial clearance for the aft finger in Build 3 compared to Build 1. The as-built radial clearance of the aft finger is 6.35 μm smaller for Build 3 than Build 1. Additionally, the axial length of the seal land on the lift pads of Build 3 is 1.36 times that of Build 1. From laminar flow theory it is known that the mass leakage rate is inversely proportional to the length of the seal land. Thus, the seal with the longer land would leak less.

TABLE IV.—SUMMARY OF STATIC LEAKAGE PERFORMANCE FLOW FACTORS OF NONCONTACTING FINGER SEALS AT DIFFERENT TEMPERATURES

NCFS build	294 K	533 K	700 K	922 K	Parameter
1	18.4	25.7	26.6	27.4	ϕ_{max}
	14	20–25	19.8	21	$\phi_{leveled}$
	276–294	508–685	664–709	867–925	T_{avg}
2	13.5	20.4	23.7	24	ϕ_{max}
	10.6	14.4	17.7	17.5	$\phi_{leveled}$
	297–299	520–549	665–697	867–907	T_{avg}
3	24.4	23.4	27.3	37.7	ϕ_{max}
	10.9	19.2	21–21.5	23, 25.7	$\phi_{leveled}$
	301–303	525–559	671–706	852–923	T_{avg}
4	9	16.3	18.5	25.5	ϕ_{max}
	5.7	9.5	12.6	15.8	$\phi_{leveled}$
	303–304	530–616	683–719	862–911	T_{avg}
5a	18.8–27.7	----------	----------	----------	ϕ_{max}
	17.5	----------	----------	----------	$\phi_{leveled}$
	280–292	----------	----------	----------	T_{avg}
5b	15	----------	----------	----------	ϕ_{max}
	13.2	----------	----------	----------	$\phi_{leveled}$
	282–289	----------	----------	----------	T_{avg}
6	16.6	26.5	27.9	31.1	ϕ_{max}
	4.8	11.1	9.6-10.6	16.8	$\phi_{leveled}$
	283–294	537–641	663–697	859–921	T_{avg}
7	21.7	28.3	29.3	33.3	ϕ_{max}
	6.9	11.6	11.5	16.2	$\phi_{leveled}$
	275–298	546–605	673–704	866–908	T_{avg}

Comparing the leakage performance of Build 2 to Build 4 (Figure 10 and Figure 12, respectively) also should reveal the effect of the aft finger axial thickness on leakage performance. Similar to the comparison of Builds 3 and 1, the at-build radial clearance of the aft finger is 6.35 μm smaller for Build 4 than Build 2, the aft axial finger thickness of Build 4 is nearly twice that of Build 2, and the axial length of the seal land on the lift pads of Build 4 is 1.36 times that of Build 2. Noting that the total flow area (Table II) for Build 4 is greater than for Build 2, one would expect the flow factors for Build 4 to be greater than those for Build 2. In fact, the data show the opposite. This result is attributed to the smaller aft finger radial clearance and longer seal land of Build 4. Further, the greater stiffness of the aft fingers likely reduces axial deflections or twisting that could change the flow area.

It is easy to see the effect of the forward finger ID on the leakage performance by comparing the leveled flow factors for the room-temperature repeat static tests for Build 1 to Build 2 and Build 3 to Build 4, shown in Table IV. In both cases, the seal with the forward finger ID nearly the same as the aft finger ID leaked less. For the seals with the baseline aft finger, Builds 1 and 2, the flow factor was reduced 24 percent by reducing the forward finger diameter. For the seals with the thicker aft finger,

Builds 3 and 4, the flow factor was reduced 48 percent by reducing the forward finger diameter. This is largely due to reducing the pinhole areas between the aft fingers bounded by the rotor OD and the forward finger ID. Also, by reducing the forward finger ID to nearly that of the aft finger, the axial leading edges of the aft fingers are exposed to a lower pressure. One could consider the forward fingers as an extension of the seal land, the length of which is inversely proportional to leakage.

Comparing Figure 9 for Build 1 to Figure 13 for Build 5a gives insight to the effect of the herringbone grooves since Build 5a is the same seal as Build 1, but on a smooth rotor. Note that the radial clearances for Build 5a are smaller than for Build 1. Despite this, Build 5a leakage levels out at a higher flow factor than Build 1 and has less hysteresis at about 150 kPa differential pressure than Build 1. The higher flow factors for Build 5a result because the smooth rotor has less resistance compared to the relatively rough herringbone grooves.

Similarly, comparison of the leakage performance of Builds 3 and 5b (Figure 11 and Figure 14, respectively) should give insight into the effect of the herringbone grooves. Again, Build 5b has slightly lower radial clearances than Build 3. Build 5b shows much less hysteresis than Build 3. Further, the curve for decreasing pressure differential of Build 5b has greater slope than that of Build 3, and above 275 kPa the flow factor of Build 5b is greater than that of Build 3. Again, the higher flow factor can be attributed to the reduced flow resistance of the smooth rotor compared to the one with relatively rough herringbone grooves.

Build 4 leakage performance (Figure 12) shows very little hysteresis and has the lowest flow factor of all the builds. Builds 6 and 7 (Figure 15 and Figure 16, respectively) have very similar levels of flow factor above a pressure differential of 300 kPa compared to that of Build 4. However, the leakage performance of Builds 6 and 7 has more hysteresis and a different curve shape at the lower pressure differentials, with a peak at approximately 20 kPa. This is surprising since Builds 6 and 7 both have at-build flow areas that are less than half that of Build 4. The peak at low pressure differential suggests that the fingers move away from the test rotor initially. One can be certain that the fingers move with pressure loading and thus change the flow areas. One thing that is different about the lift pads of Builds 6 and 7 is that neither has a circumferential groove. Hence, the whole axial length of the lift pad acts as a seal land. The effectiveness of these seal lands is affected by the changing clearance due to the circumferential and axial tapers.

Comparison to Analytically Predicted Leakage

Predictions of room-temperature static leakage performance were made for Builds 1 through 4 using the leakage model described in Reference 10 and the assumption of isentropic flow. It is also assumed that the geometry is fixed, the lift pads remain concentric to the rotor, and that the fingers are held tightly against each other and the seal dam so that there is no leakage between the contacting areas. The seal radial clearance is an input parameter. The predictions for the NCFS Build 4 using a discharge coefficient of 1.0 are shown in Figure 17. Comparing the predictions to the room-temperature static performance results for Build 4 (Figure 12), the predicted flow factors for radial clearance of 0.0127 to 0.0254 mm most closely match the test data. Table V shows the choked flow factors for several clearances for each of the Builds 1 to 4 for comparison. It is interesting to note that the predicted flow factors for Builds 1 and 4 are nearly the same. As expected, Build 3 has the largest predicted flow factor of these builds, and Build 2 has the lowest predicted flow factor.

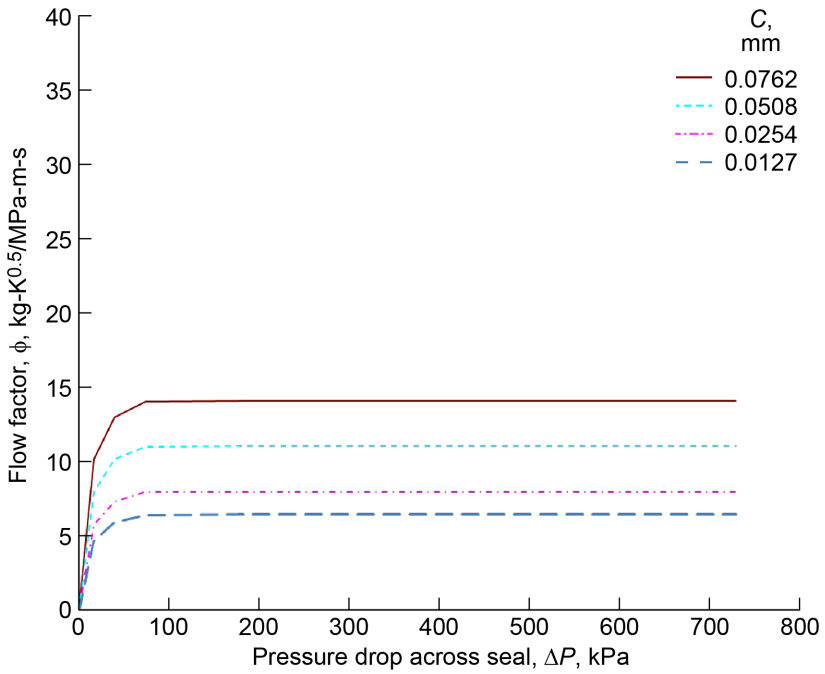

Figure 17.—Predicted static leakage performance for NCFS Build 4, assuming isentropic choked flow and a discharge coefficient of 1.0, for various radial clearances, *C*.

TABLE V.—PREDICTED FLOW FACTORS, ASSUMING ISENTROPIC CHOKED FLOW, FOR SEVERAL RADIAL CLEARANCES BETWEEN LIFT PAD AND ROTOR

[In kg-K$^{0.5}$/MPa-m-s.]

NCFS build	Clearance, mm			
	0.0127	0.0254	0.0508	0.0762
1	6.5	8.1	11.1	14.1
2	4.2	5.8	8.8	11.9
3	8.7	10.2	13.3	16.4
4	6.4	8.0	11.0	14.1

Leakage Performance at 922 K

The seal static leakage performance test results at 922 K (1,200 °F) are shown in Figure 18 to Figure 23 for Builds 1, 2, 3, 4, 6, and 7, respectively. In all cases, the flow factor at 922 K is higher than at room temperature. The shapes of the data curves for Builds 1, 2, 3, and 4 at 922 K are similar to data taken at room temperature. However, for Builds 6 and 7 (Figure 22 and Figure 23), the shape of the curve for decreasing pressure differential is different at 922 K compared to that at room temperature (Figure 15 and Figure 16). Specifically, the flow factor decreases once the pressure differential is reduced lower than 200 kPa rather than tracking the data curve for increasing pressure differential. Explanation of this observation is speculative, but likely is due to clearance changes and thermal effects.

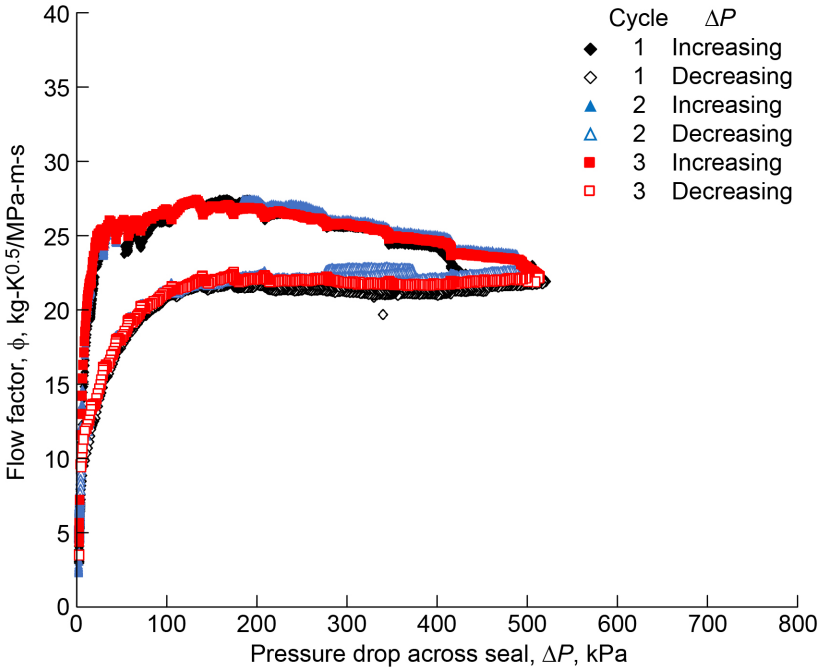

Figure 18.—Static leakage performance of baseline NCFS Build 1 at 867 to 925 K average inlet air temperature.

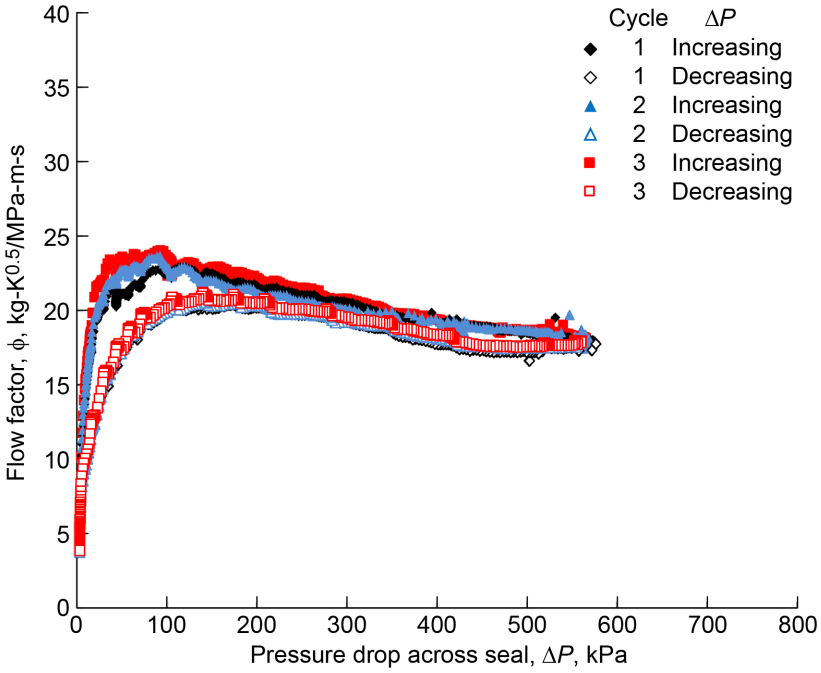

Figure 19.—Static leakage performance of NCFS Build 2 at 867 to 907 K average inlet air temperature.

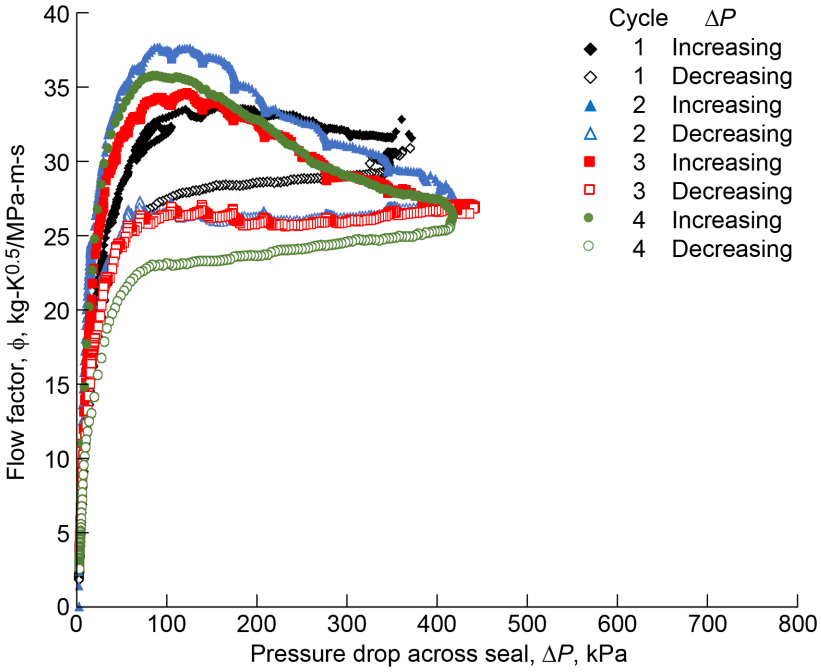

Figure 20.—Static leakage performance of NCFS Build 3 at 852 to 923 K average inlet air temperature.

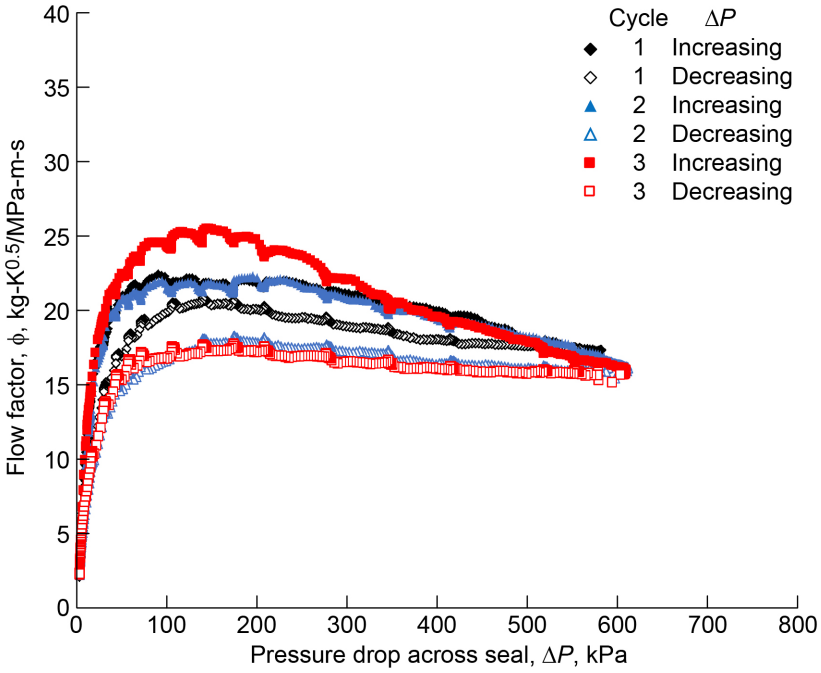

Figure 21.—Static leakage performance of NCFS Build 4 at 862 to 911 K average inlet air temperature.

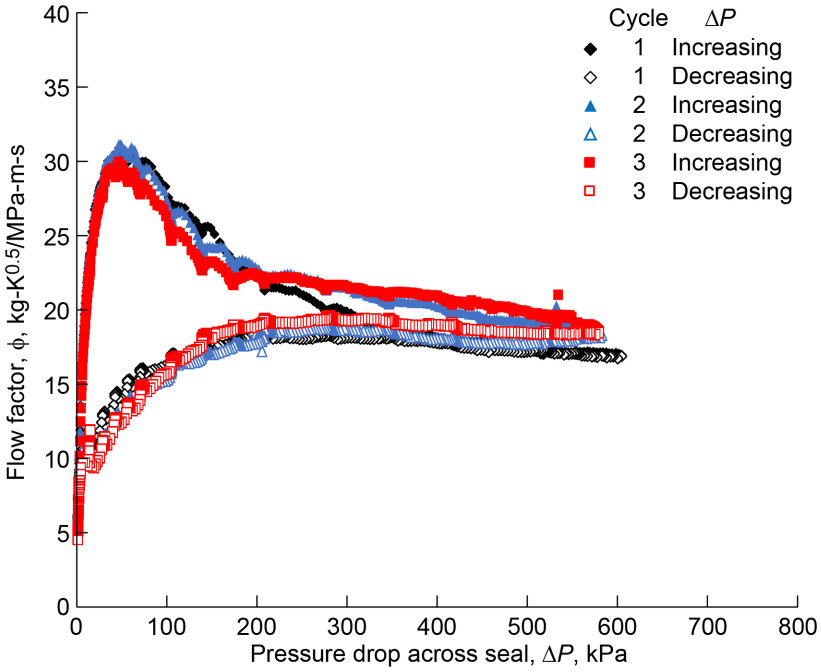

Figure 22.—Static leakage performance of NCFS Build 6, with circumferential taper on lift pad, at 859 to 921 K average inlet air temperature.

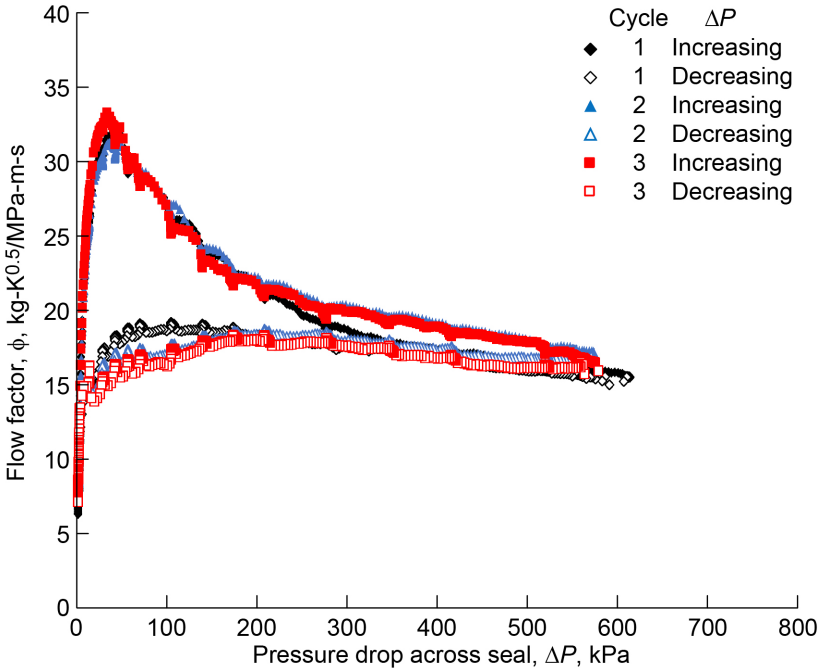

Figure 23.—Static leakage performance of NCFS Build 7, with axial taper on lift pad, at 866 to 908 K average inlet air temperature.

Bind-Up Pressure

Results of the bind-up tests are summarized in Table VI, which shows the pressure differential at which the free-wheeling decreased, stopped, and at which bind-up occurred. In a few cases, a faint metallic squeak could be heard, indicating rubbing contact. Also, in some cases, a torque wrench was used to measure the bind-up torque.

Comparing the bind-up pressure differentials for Builds 1 and 2, it is observed that a greater pressure differential is needed to cause bind-up for Build 1 than for Build 2. The Build 1 seal has a larger radial clearance between the forward finger and the rotor than does Build 2, and it is reasonable that Build 1 would require more of a pressure differential to draw those fingers into the rotor than Build 2. A similar finding is evident when comparing Builds 3 and 4, which have the same aft finger element, but Build 3 has a larger radial clearance between the forward fingers and rotor than Build 4 does. Note in Table VI that a bind-up test for Build 4 was conducted at 672 K (750 °F), which found that bind-up occurred at higher pressure differentials than it did at room temperature. This is due to the seal material having a higher coefficient of thermal expansion than the rotor, which increases the seal clearance.

Builds 1 and 3 have the same forward finger element, but Build 3 has an aft finger axial thickness approximately double that of the Build 1 seal. With the greater axial finger thickness, Build 3 would have greater stiffness and require a higher pressure differential to draw it into the rotor. The bind-up test results are consistent with this expectation, with Build 3 binding up at 386 kPa compared to Build 1 binding up at 248 kPa.

Comparing Builds 1 and 5a, which are the same seal, but on the herringbone-grooved rotor and smooth rotor, respectively, one can see that bind-up for Build 5a occurred at a much higher pressure differential than for Build 1. This is surprising since the radial clearances for Build 5a are smaller than for Build 1.

Comparing Builds 3 and 5b, which are, again, the same seal, but on the herringbone-grooved rotor and smooth rotor, respectively, the bind-up pressure for Build 5b is found to be lower than for Build 3. This is as expected since the Build 5b seal has a smaller clearance than Build 3 does.

TABLE VI.—BIND-UP TEST RESULTS: PRESSURE DIFFERENTIAL ACROSS SEAL

NCFS build	Pressure differential, kPa			
	Less free wheeling	Free wheeling stopped	Tight	Comment
1	83	124	248	2 N-m torque, faint squeak at 248 kPa
2	55	83	165–248	Light squeak at 248 kPa
3	96.5	317	386	
4	96.5	303	344	Very hard to turn at 517 kPa
4 (672 K)	317	358	414	
5a	68.9	262	372	
5b	83	138	345	6.8 N-m torque at 150 kPa
6	83	248	414	4 N-m torque at 414 kPa
7	96.5	276	317	Faint squeak at 317 kPa

Comparing Builds 6 and 7, which have 0.0127-mm (0.0005-in.) circumferential and axial tapers, respectively, on a smooth rotor, to Build 2, it is seen that both Builds 6 and 7 bind up at higher pressures than Build 2 does, even though they have smaller radial clearances than Build 2. This could be explained by the fact that the lift pads of Builds 6 and 7 do not have circumferential grooves. It is possible that without the circumferential groove, the pressure gradient under the lift pad is more gradual, resulting in a higher pressure under the lift pads to counteract the closing forces.

There is no intention to imply that the circumferential groove is bad. Rather, the circumferential groove is critical to the concept that uses the herringbone-grooved rotor. The circumferential groove, if designed properly, isolates the hydrodynamic lifting features from the hydrostatic effects and ensures that there is low pressure on all four sides of the area on the lift pads where the herringbone grooves pump. It may be possible to increase the bind-up pressure for this seal by increasing the radial clearance. The tapers on Builds 6 and 7 change the average clearance, making it a little bigger. The bind-up pressure depends on the pressure profile on the lift pads. For the lift pads with the tapers, it is possible that the hydrodynamic lift generated by shaft rotation may get overwhelmed by axial hydrostatic flows at high pressure differentials.

Hardware Inspection

Figure 24 shows a photograph of the herringbone-grooved rotor OD surface after the static performance test of the NCFS Build 1 at 922 K. This rotor was previously used for lift-off testing during which a continuous burnished track of no measurable depth was generated upstream of the herringbone grooves, presumably during startup and shutdown of rotation. Within this track, there are periodic shiny rub spots that resulted from the bind-up test in which a light squeak was heard. It shows that only a portion of each finger pad touched the rotor with enough force to cause damage. The location of the rub spots within the track suggests contact occurred at the leading edge of the aft fingers. Also, there is a heat pattern on the rotor OD that corresponds to the air flow.

Figure 25 shows a photograph of a sector of the ID surface of the NCFS Build 1 aft finger lift pads. Several lift pads have a shiny area on the upstream edge near the heel of the finger, which confirms the point of contact that caused the damage to the rotor in the bind-up test. The pattern in the discoloration is like that on the rotor OD in Figure 24. The pattern resembles a spreading flow from a point source near the center of the upstream edge of each lift pad that fans out circumferentially as it moves axially downstream. Of course, that point-source location corresponds to the gap between the forward fingers. It does appear that for some of the pads there is a second triangular shape in the color that originates with a point nominally in the middle of the lift pad that fans out to the downstream edge of the lift pad. This second pattern is probably due to the land between the two rows of grooves on the rotor and the flow going through a smaller clearance at that point.

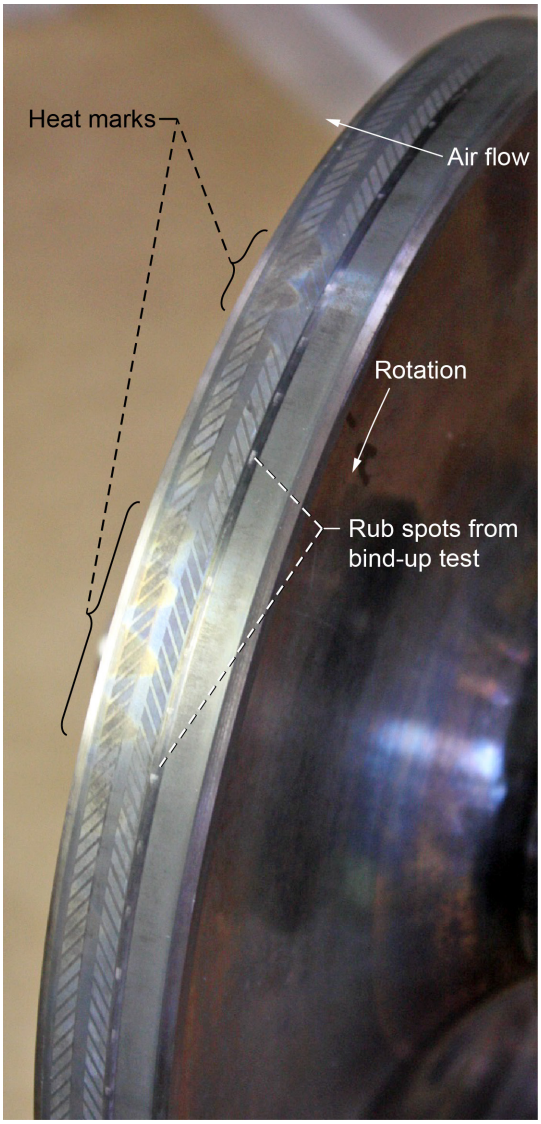

Figure 24.—Herringbone-grooved rotor OD after static performance test of NCFS Build 1 at 922 K.

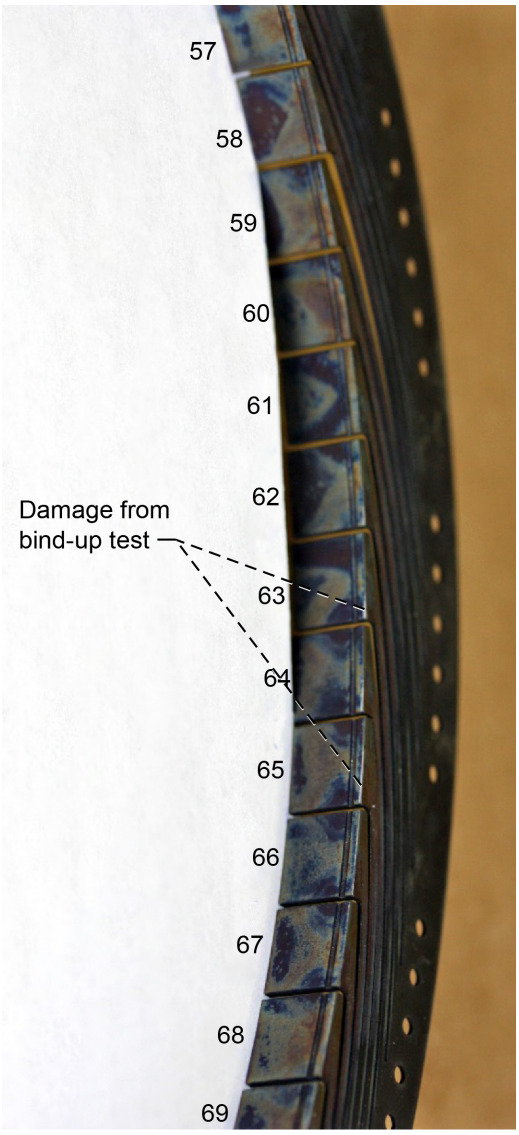

Figure 25.—NCFS Build 1 aft finger lift pads ID surface after static performance testing at 922 K.

Conclusions From Static Testing

- The application of both pressure differential across the seal and some rotation is needed to optimally seat the seal for repeatable flow measurements.
- Bind-up of the NCFS results from the pressure differential across the seal, deflecting the fingers to contact the rotor. This contact occurs at the heel of the aft finger. Given the axial width of the wear mark on the rotor caused by bind-up and the narrow burnish mark on the aft finger leading edge, it is possible that the aft finger deflects axially and twists slightly and/or some of the upstream finger contacts the rotor as well. The pressure differential at which bind-up occurs increases with increased radial clearance.
- Completely covering the gaps between the fingers by matching IDs of the forward and aft fingers significantly reduces the leakage.

- Longer seal lands as found in the tapered lift pads can cause more leakage with increasing pressure differential because of lifting of the fingers. The taper provides a path for more high pressure to get to the lift pad ID, and there is more area for the pressure to act compared to lift pads with a circumferential groove.
- The maximum pressure capability of the NCFSs tested at static conditions was between approximately 100 and 300 kPa at 0 rpm. With centrifugal growth of the rotor affecting the seal clearance, the maximum pressure capability should be adjusted downward as speed is increased.
- The NCFS with the axially thick finger and the same ID of the forward and aft fingers (Build 4) had the lowest leakage flow factor at approximately 7 kg-$K^{0.5}$/MPa-m-s and the least hysteresis.
- Performance testing below the maximum pressure capability is needed to determine if the hydrodynamic lifting forces will prevent contact as the shaft grows with rotation.

Dynamic Test Results and Discussion

Leakage Performance

Build 2

The time history of the speed, average test seal inlet and exit air temperatures, and the average seal backface temperature during the lift-off test is shown in Figure 26. The seal backface temperature initially rises from 296 K to about 300 K, or about 4 K, over 100 s while the speed was increased from 0 to 5,000 rpm. It then continues to climb another 0.8 K even though the speed was constant to approximately 300.8 K, just before the speed was decreased. The heating observed is due to windage, and the continued increase in temperature at constant speed is expected since the test chamber is insulated. If rubbing wear occurred there would have been an initial spike in temperature followed by a decrease in temperature once the interference was worn away.

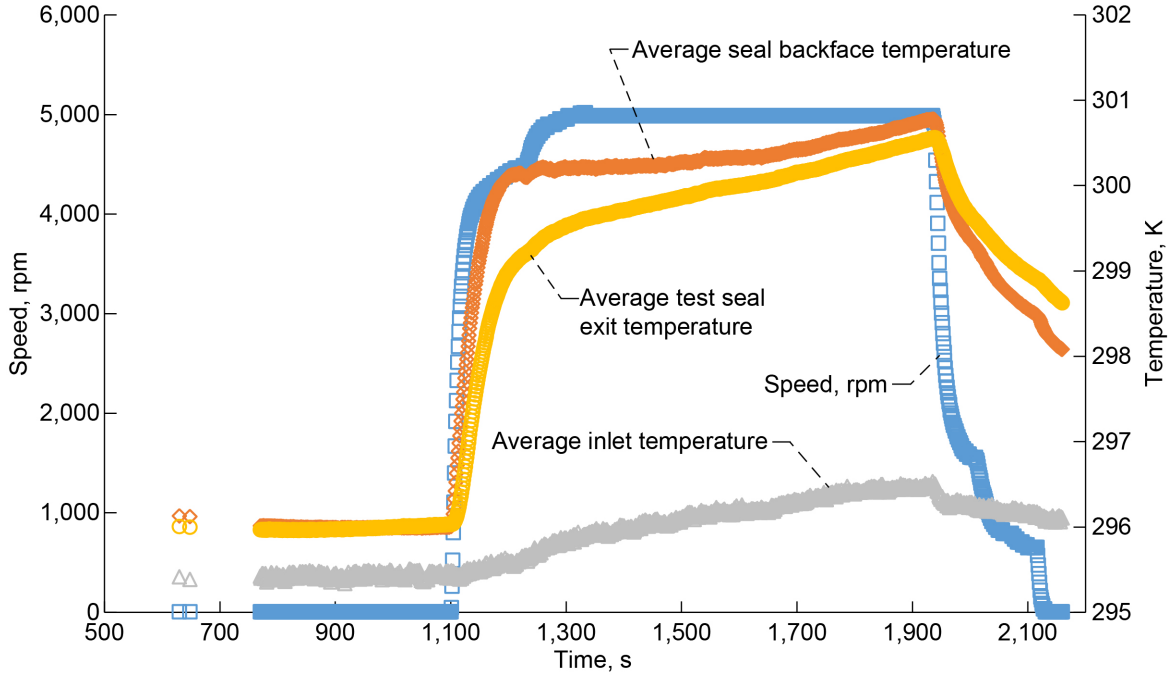

Figure 26.—Time history of speed and temperatures during lift-off test for NCFS Build 2.

The leakage performance of NCFS Build 2 at 69 kPa is shown in Figure 27. The flow factor for cycle 1 with increasing speed is approximately 8 kg-$K^{0.5}$/MPa-m-s, which is lower than the other cycles. Also, in this part of cycle 1 there are spikes in the flow factor at speeds of approximately 315, 360, and 425 m/s. As speed decreases a smaller peak appears between 270 to 280 m/s. For the other cycles the flow factor is approximately 12.5 kg-$K^{0.5}$/MPa-m-s. The spikes and the higher flow factor may indicate that wear has occurred. There is a slight decrease in flow factor as speed increases, which is likely the result of centrifugal growth of the rotor and a slight reduction in clearance. Average seal inlet air temperature increased over time, ranged from 295 to 397 K, and on average was 327 K.

Build 7

In the lift-off test for Build 7 the average seal backface temperature increases by less than 1.1 K. Results of the room-temperature leakage performance test of the NCFS Build 7 are shown in Figure 28. In cycle 1, as the speed increases, the flow factor decreases from 13.4 kg-$K^{0.5}$/MPa-m-s at 55 m/s to 7 kg-$K^{0.5}$/MPa-m-s at 374 m/s. In cycle 1, as the speed decreases, the seal shows hysteresis as evidenced by the resulting lower flow factor of 8.7 kg-$K^{0.5}$/MPa-m-s at 0 rpm. Cycle 2, at both increasing and decreasing speeds, has flow factors close to the level of cycle 1 with decreasing speed. Flow factors for cycle 3 closely match those of cycle 1 and show the same hysteresis. This may be due to the pressure differential across the seal being reduced to 0 kPa between the second and third cycles for operational reasons, thus removing the pressure closing forces. The flow factor is 6.9 kg-$K^{0.5}$/MPa-m-s at the maximum speed of 446 m/s. Spikes in the flow factor are seen in the data at speeds of approximately 100, 275 to 290, and 315 m/s.

Figure 29 shows the flow factor measured during a test conducted at 5,000 rpm while the pressure differential was increased and decreased. Although the intent was to hold speed constant at 5,000 rpm, fluctuations in speed did occur in cycle 1 while increasing the pressure differential to 206 kPa. As the pressure differential was increased, the speed fell by about 200 rpm until the controller readjusted. At 206 kPa an operator error caused the pressure differential across the seal to increase to 556 kPa. During this climb there was a loss of tachometer signal that caused a turbine shutdown. Thus, the data shown for cycle 1 with decreasing pressure differential actually is at 0 rpm. In cycle 2, this seal also exhibits hysteresis since the flow factor for decreasing pressure differential is less than for increasing pressure differential. This indicates that once the pressure differential is applied, frictional forces hold the seal fingers in position.

The leakage performance of NCFS Build 7 at 172 kPa pressure differential is shown in Figure 30. At 0 rpm the flow factor is approximately 8 kg-$K^{0.5}$/MPa-m-s and generally decreases when speed increases, as the flow factor at 430 m/s is 20 to 25 percent lower. A notable exception to this is seen in the peaks in flow factor that occur at 312 m/s for cycle 1 when increasing speed, 272 to 276 m/s for cycles 1 and 2 when decreasing speed, and 289 m/s for cycle 3 when decreasing speed. The largest peaks in flow factor are nearly identical for cycles 1 and 2 when decreasing speed and have a value of 12 kg-$K^{0.5}$/MPa-m-s, which is 50 percent greater than the flow factor at 0 rpm. The peak in flow factor for cycle 3 when decreasing speed is slightly less at 10.6 kg-$K^{0.5}$/MPa-m-s. The maximum speed attained in cycle 3 is 396 m/s, a little less than the 430 m/s attained in cycles 1 and 2. All three speed cycles started with an initial average inlet air temperature of 295 K. It is interesting to note that the average seal backface temperature rose by 217, 182, and 147 K at maximum speed for cycles 1, 2, and 3, respectively, and that the rise in temperature was less for each subsequent cycle. This temperature increase is due to windage heating and is affected by the length of time of rotation between 0 and the maximum speed, which was 3,375; 1,928; and 2,142 s for cycles 1, 2, and 3, respectively. The fact that the time of rotation for speed increasing for cycle 3 is greater than cycle 2, and yet the rise in seal backface temperature was less for cycle 3 than cycle 2, points to possible wearing away of the seal.

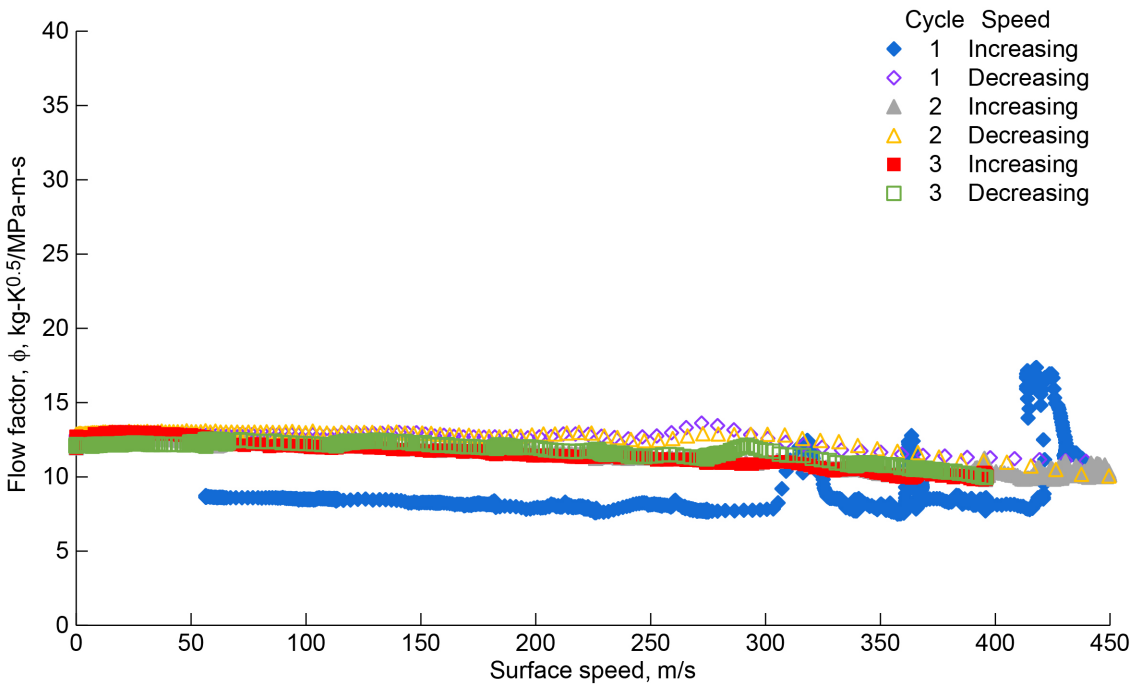

Figure 27.—Leakage performance of NCFS Build 2 at 69 kPa pressure differential and average seal inlet air temperature of 327 K.

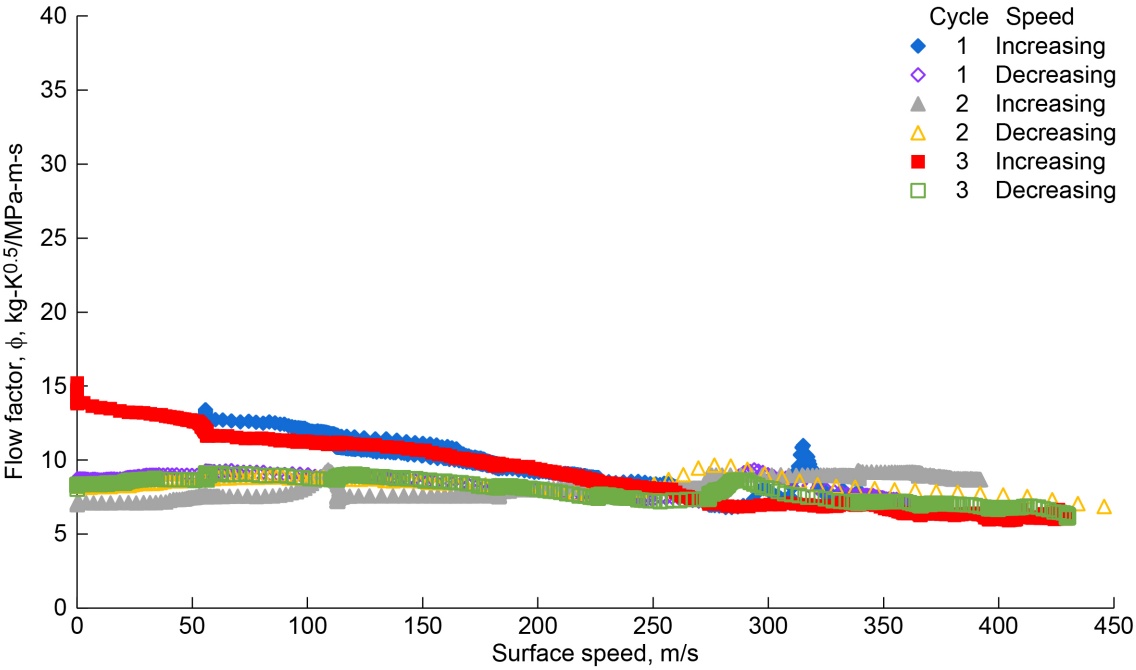

Figure 28.—Leakage performance of NCFS Build 7 at average seal inlet air temperature, which ranged from 296 to 421 K, and on average was 341 K and pressure differential of 69 kPa.

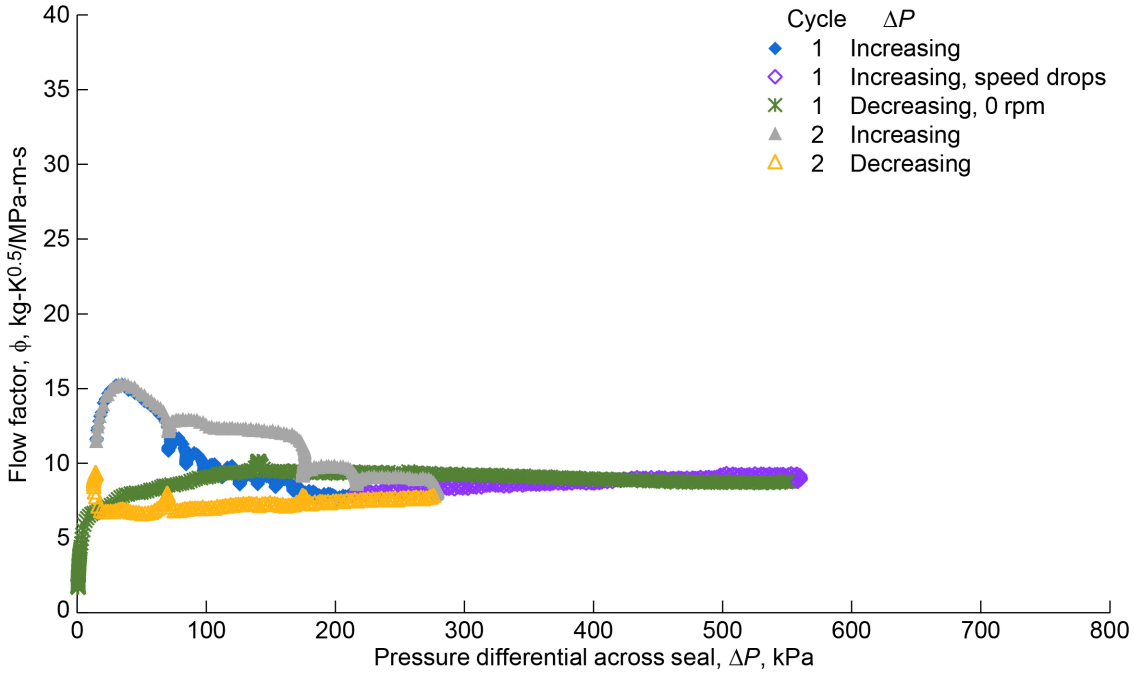

Figure 29.—Leakage performance of NCFS Build 7 at 5,000 rpm and average seal inlet air temperature of 291 K.

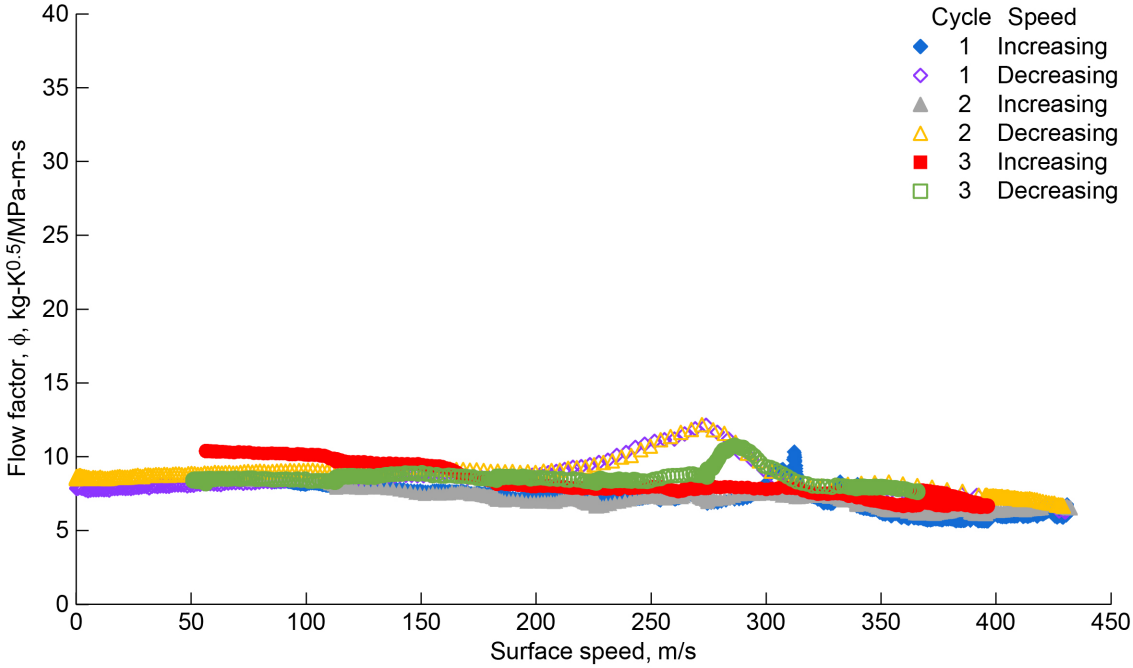

Figure 30.—Leakage performance of NCFS Build 7 at pressure differential of 172 kPa and initial average seal inlet air temperature of 296 K.

Next, three speed cycles at 276 kPa pressure differential were conducted, which resulted in the leakage performance shown in Figure 31. The flow factor in cycle 1 starts at 8.8 kg-$K^{0.5}$/MPa-m-s and remains fairly level until speed increases to 270 m/s. At this speed the flow factor starts increasing with increasing speed to 12 kg-$K^{0.5}$/MPa-m-s at 396 m/s, which is a 36-percent increase in flow factor. Then as speed decreases, the flow factor continues to increase, peaking at 17.6 kg-$K^{0.5}$/MPa-m-s at 266 m/s, and then decreases to a level of about 15 kg-$K^{0.5}$/MPa-m-s. Cycle 2 starts at a slightly higher flow factor of 15.7 kg-$K^{0.5}$/MPa-m-s at 0 m/s and decreases as speed increases to 12.6 kg-$K^{0.5}$/MPa-m-s at 395 m/s. Again, flow factor increases as speed decreases, peaking at 16.6 kg-$K^{0.5}$/MPa-m-s and 289 m/s before leveling out to the flow factor at which this cycle started. Cycle 3 starts at a flow factor of 18.6 kg-$K^{0.5}$/MPa-m-s at 56 m/s, and then as speed increases, it decreases to 13.5 kg-$K^{0.5}$/MPa-m-s at 395 m/s. As speed decreases in cycle 3, the flow factor is higher than in cycle 2 with decreasing speed, peaking at 17.6 kg-$K^{0.5}$/MPa-m-s at 289 m/s, and coming back down to approximately 16.3 kg-$K^{0.5}$/MPa-m-s at a surface speed of 7 m/s. The initial average seal inlet air temperature for speed cycle 1 was 293 K, and for cycles 2 and 3 it was 286 K. The average seal backface temperature rose by 112, 111, and 107 K at maximum speed during cycles 1, 2, and 3, respectively; there was nearly the same temperature rise for each cycle, unlike the test at 172 kPa pressure differential.

Build 3

During the room-temperature lift-off test of the NCFS Build 3, the average seal backface temperature rose by 1.9 K, which did not raise suspicion of rubbing contact. The leakage performance of NCFS Build 3 is shown in Figure 32. The flow factor decreases from 15 kg-$K^{0.5}$/MPa-m-s at zero speed to 9.5 kg-$K^{0.5}$/MPa-m-s at 307 m/s. Cycles 1 and 2 are very similar and show little to no hysteresis. Cycle 3 with speed increasing follows cycles 1 and 2 quite closely until about 300 m/s. At that point the flow factor becomes more erratic and ranges between 7.8 at 460 m/s and 11.9 kg-$K^{0.5}$/MPa-m-s at 340 m/s. During cycle 3 with decreasing speed, the flow factor is as much as 35 percent larger than cycles 1 and 2 at 340 m/s but returns to the same level as cycles 1 and 2 at 0 rpm.

The cause of the erratic behavior in cycle 3 may be due to fluctuations in the pressure differential across the seal, which started during cycle 3 while increasing speed at 30,000 rpm and had an amplitude of ±1.4 to ±3.4 KPa. This leads to the question, “what started the pressure fluctuations?” While decreasing speed in cycle 3, there was a low lubricant level that tripped a turbine speed shutdown. Investigation of the low lubricant level found the oil was gurgling up the vent stack. The vent from the bearing drain cavity carries away purge air from the labyrinth seals on either side of the bearing cavity. Since some of the air from the test end labyrinth seal exits the rig through the test seal exhaust cavity, it is possible that the pressure fluctuations in the vent stack affected the pressure differential across the seal. Although the turbine shutdown did not occur until speed was decreasing, the gurgling of oil in the vent stack takes time to develop and would precede that event. Alternatively, it could be that the fingers do not respond quickly enough to rotor dynamics. In any event, the problems with the lubrication system had to be addressed.

The primary changes to the lubrication system were that a new and larger reservoir with baffles and proper returns was installed to better handle the amount of air returning to the reservoir, and the reservoir was vented through a breather into the room. Previously, the reservoir was vented through a smoke eliminator that was also connected to the bearing drain cavity vent. When the low-oil-level alarm was activated and the oil was gurgling in the vent stack, it was necessary to turn off the labyrinth seal purge air to get the oil to drain back into the oil reservoir. The modifications to the lubrication system appeared effective, and subsequent tests of Build 4 with new finger elements were conducted without incident.

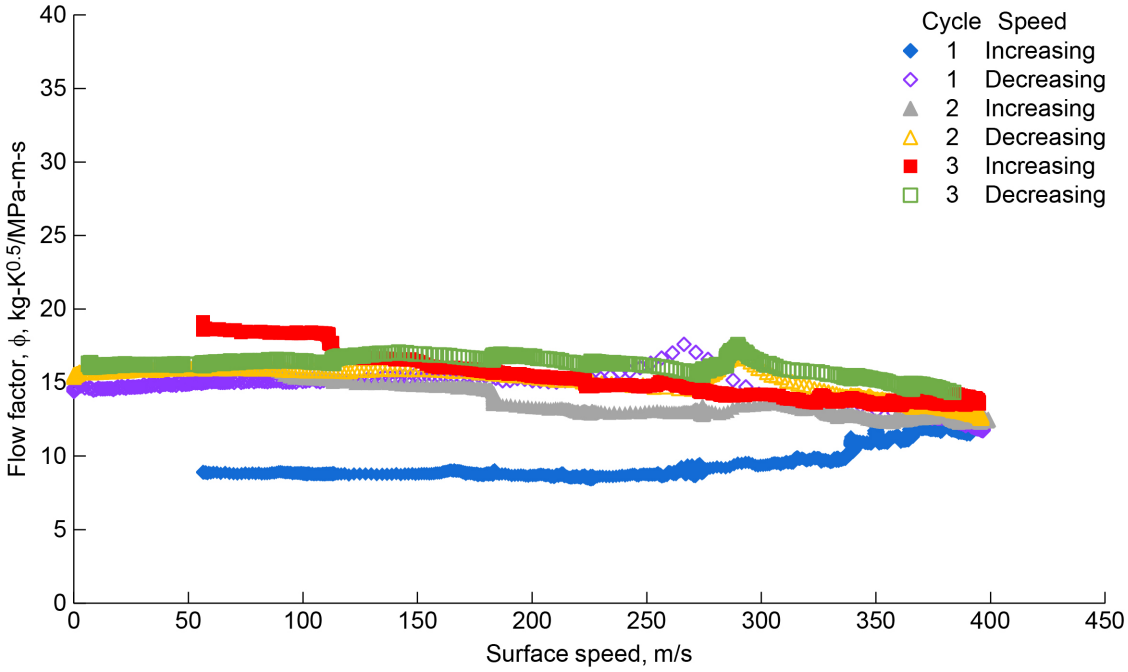

Figure 31.—Leakage performance of NCFS Build 7 at pressure differential of 276 kPa and initial average seal inlet air temperature of 286 to 293 K.

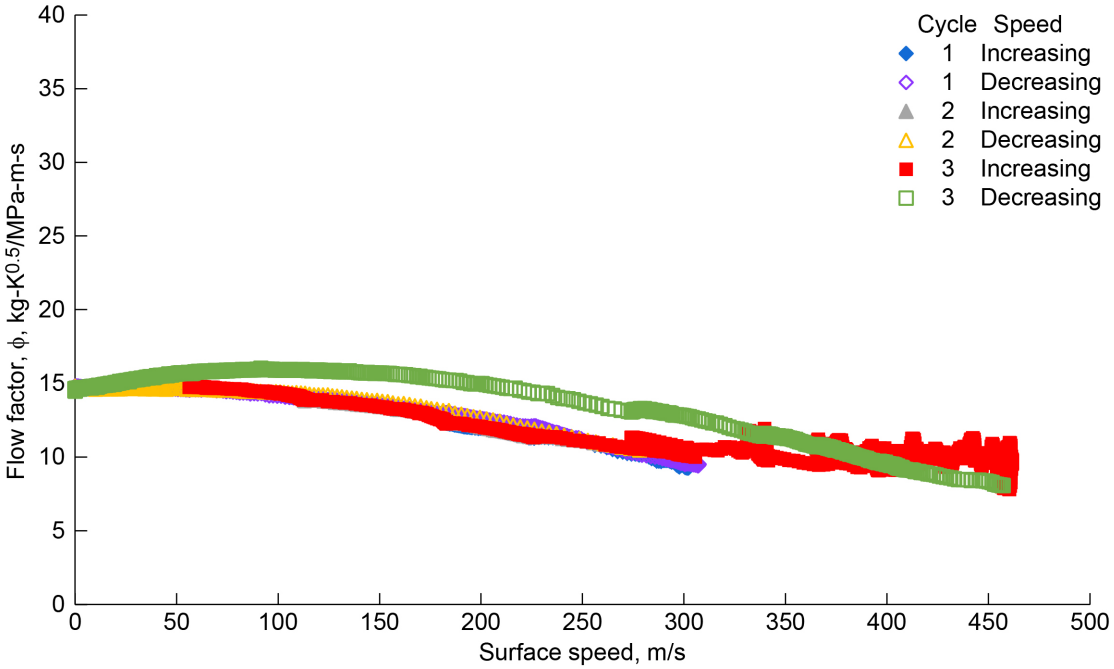

Figure 32.—Leakage performance of NCFS Build 3 at pressure differential of 69 kPa and average seal inlet air temperature of 304 K.

Build 4 With New Finger Elements

The room-temperature static leakage performance of the NCFS Build 4 with new finger elements is shown in Figure 33. The three cycles of increasing and decreasing pressure differential are in good agreement. This seal had a small amount of hysteresis, and the flow factor is approximately 10 kg-$K^{0.5}$/MPa-m-s at pressure differentials of 69 kPa and higher. This is about 75 percent more than the first NCFS Build 4 presented in Figure 12.

69 kPa tests

The leakage performance of the NCFS Build 4 with new finger elements at pressure differentials of 69 kPa and average inlet air temperatures of 287, 631, 689, and 882 K are shown in Figure 34 to Figure 37, respectively.

For the room-temperature results shown in Figure 34, the average seal backface temperature rose 143 K in the 2,699 s it took to go from 56 m/s to a maximum speed of 366 m/s in cycle 1. In cycle 2 the average seal backface temperature rose 110 K, but it only took 1,454 s to accomplish the increasing speed cycle so it makes sense that the temperature rise would be less. The spikes in flow factor in the cycle 1 increasing speed data occur at 263 and 328 m/s. At these same speeds in the cycle 1 increasing speed data there are spikes in the mass leakage rate and in the average seal backface temperature. The average seal backface temperature spike is about 6 K and drops—even as speed continues to increase. Although the spike in seal backface temperature could indicate a rubbing contact occurred, the fact that the flow factor and leakage rate spiked indicates an opening up of the seal, perhaps due to slow response of the seal to a resonant frequency of the rotor. There were no spikes in seal backface temperature for the high-temperature data taken at 69-kPa pressure differential.

The flow factor at 631 K average seal inlet air temperature and 69 kPa pressure differential (Figure 35), ranges from 18.5 kg-$K^{0.5}$/MPa-m-s at 56 m/s to 6 kg-$K^{0.5}$/MPa-m-s at 365 m/s. Cycle 1 has substantial hysteresis, while cycle 2 shows very little difference between the increasing and decreasing portions of the speed cycle. The initial temperature in cycle 1 was 592 K and increased by 54 K at the maximum speed. The variation in temperature was about a third of that in subsequent speed cycles.

For average seal inlet air temperature of 689 K and 69 kPa pressure differential (Figure 36), the flow factor ranges from 22.4 kg-$K^{0.5}$/MPa-m-s at 56 m/s to 7.6 kg-$K^{0.5}$/MPa-m-s at 366 m/s. Again, cycle 1 has more hysteresis than the subsequent cycles. The flow factors in cycles 2 and 3 are very nearly the same.

At 882 K average seal inlet air temperature and 69 kPa pressure differential (Figure 37), the flow factor ranges from 25.5 kg-$K^{0.5}$/MPa-m-s at 56 m/s to 9.3 kg-$K^{0.5}$/MPa-m-s at 370 m/s. As at lower temperatures, cycle 1 has more hysteresis than cycles 2 and 3. It is interesting to note that all three cycles have little hysteresis and are very much in agreement with each other at speeds of 275 m/s and above. A comparison of Figure 33 to Figure 36 shows that the flow factor increases as the temperature increases, which indicates the seal clearance increases with temperature. In addition, it is interesting to note that the effect of speed on the leakage rate is greater at the high temperatures than at room temperature.

172 kPa test

Figure 38 shows the leakage performance of the NCFS Build 4 with new finger elements at 315 K average seal inlet air temperature and 172 kPa pressure differential across the seal. The flow factor ranges from 9.1 kg-$K^{0.5}$/MPa-m-s at 56 m/s to 5.6 kg-$K^{0.5}$/MPa-m-s at 364 m/s. The flow factors measured with 172 kPa across the seal are very similar to those with 69 kPa across the seal at room temperature (Figure 34).

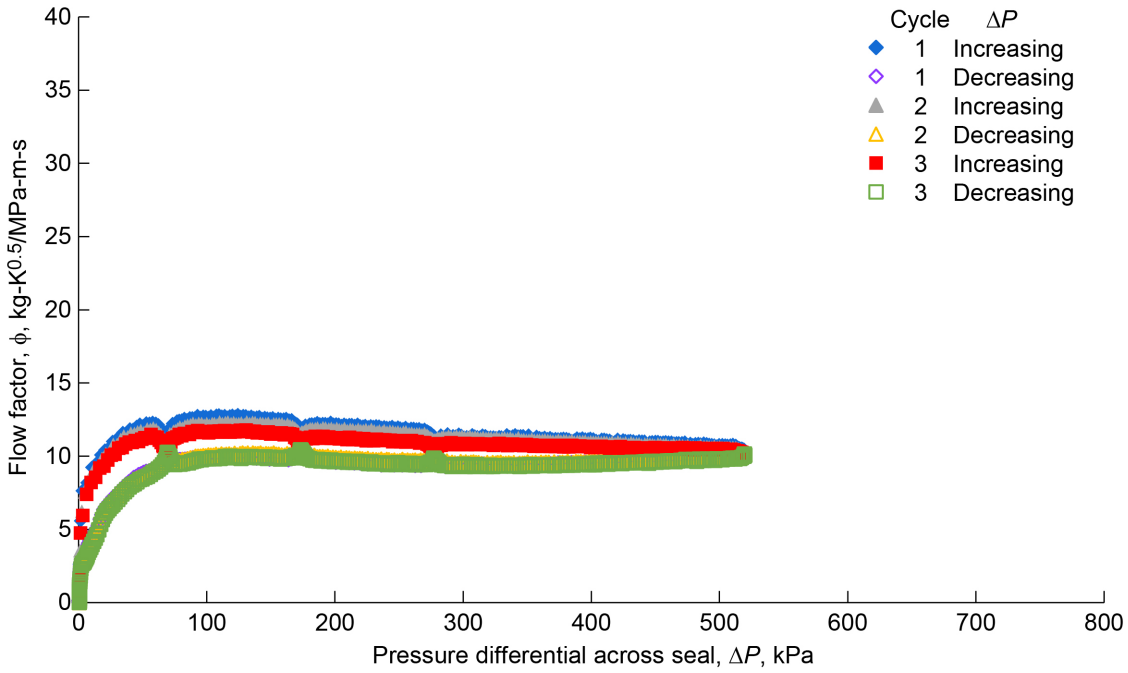

Figure 33.—Static leakage performance of NCFS Build 4 with new finger elements at average inlet air temperature of 289 K.

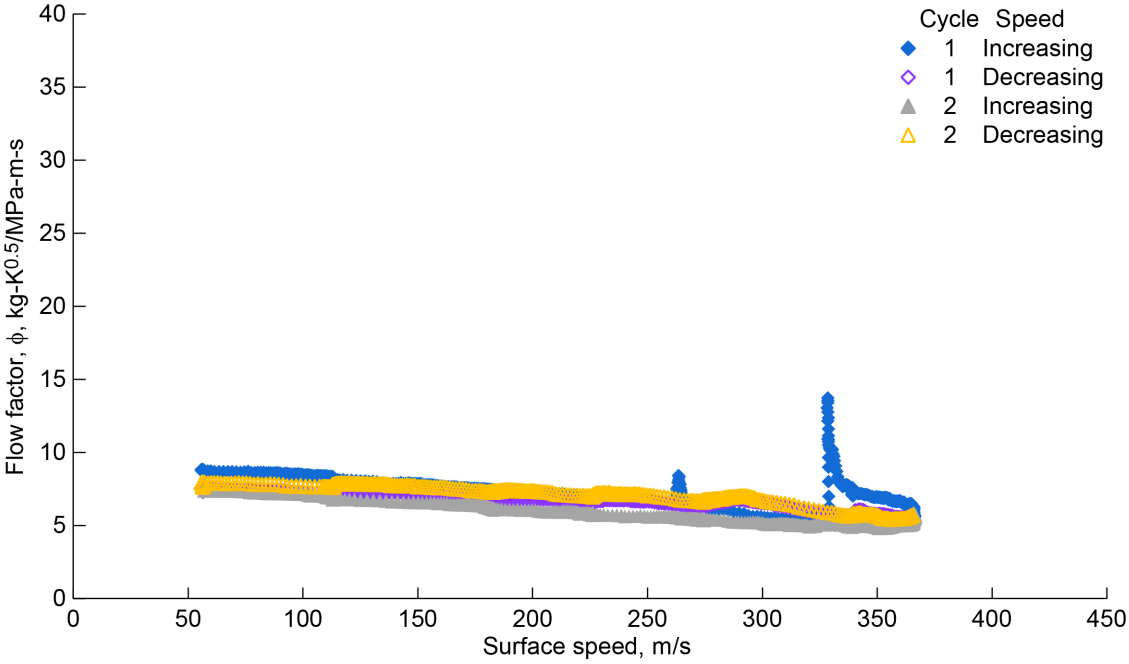

Figure 34.—Leakage performance of NCFS Build 4 with new finger elements at pressure differential of 69 kPa and initial average inlet air temperature of 287 K.

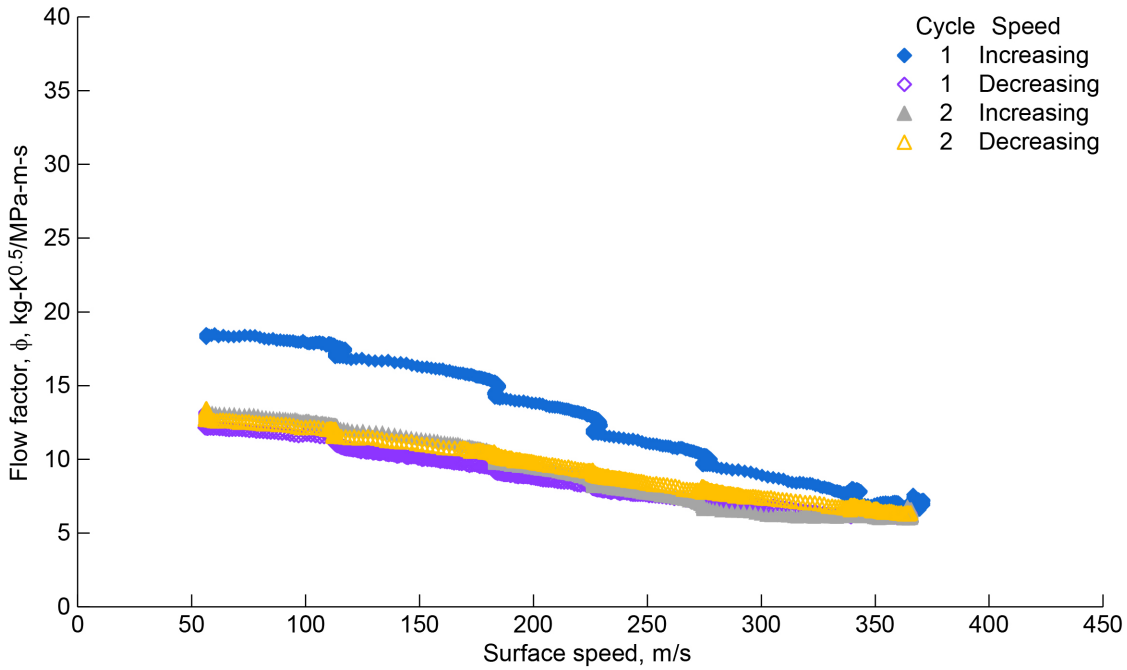

Figure 35.—Leakage performance of NCFS Build 4 with new finger elements at pressure differential of 69 kPa and average seal inlet air temperature of 631 K.

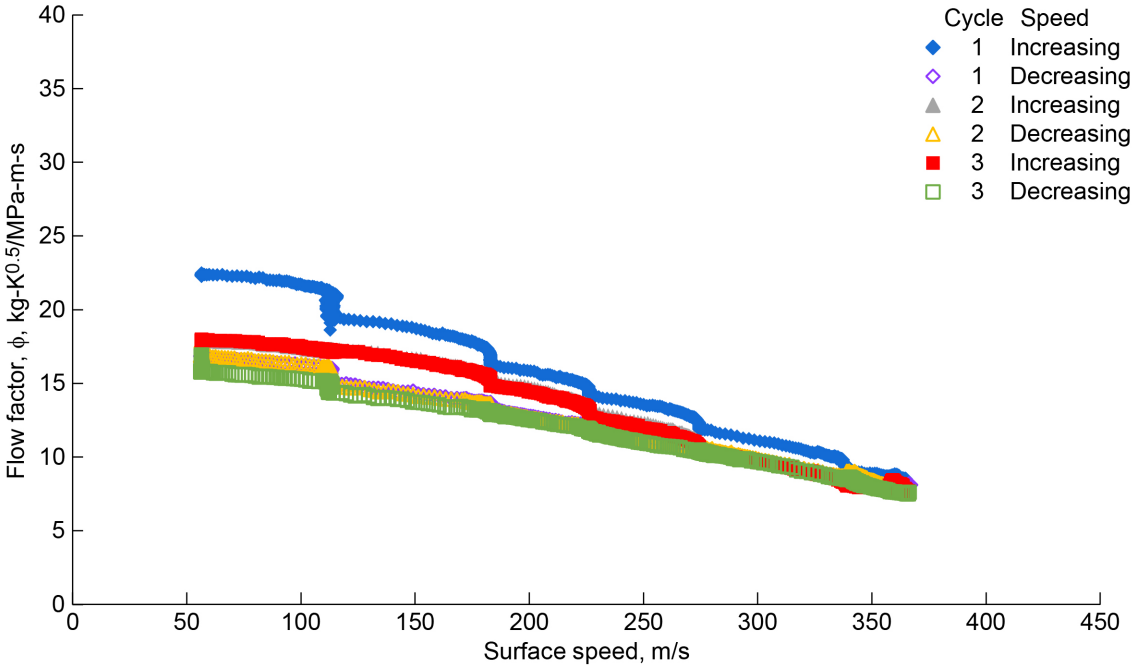

Figure 36.—Leakage performance of NCFS Build 4 with new finger elements at pressure differential of 69 kPa and average seal inlet air temperature of 689 K.

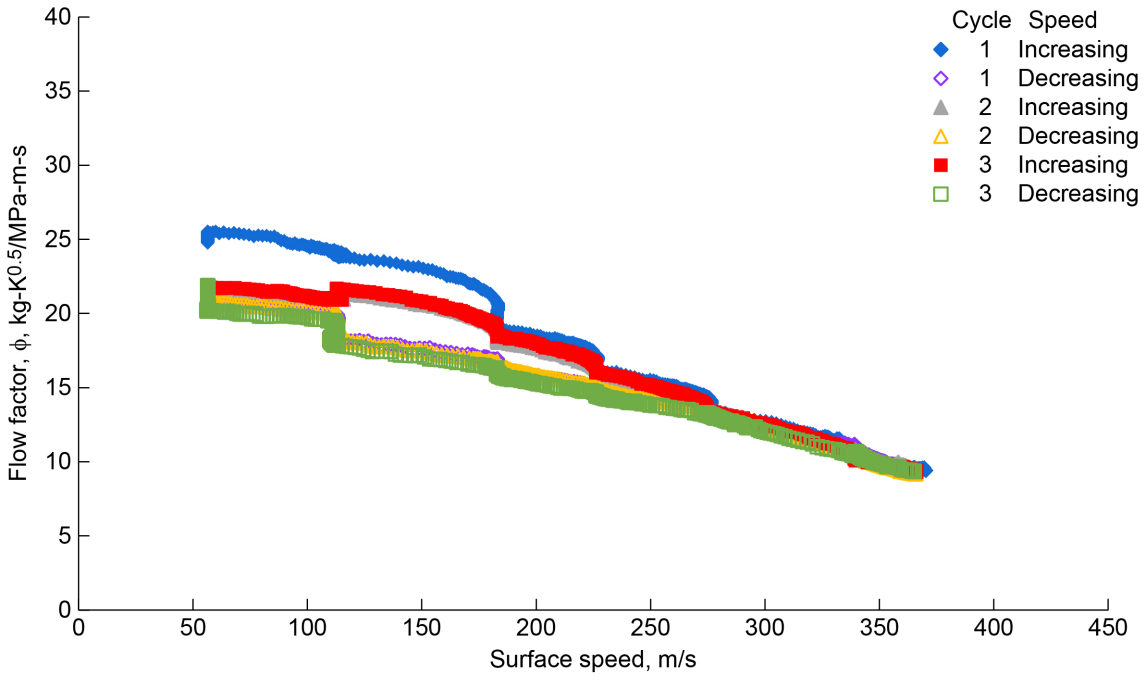

Figure 37.—Leakage performance of NCFS Build 4 with new finger elements at pressure differential of 69 kPa and average seal inlet air temperature of 882 K.

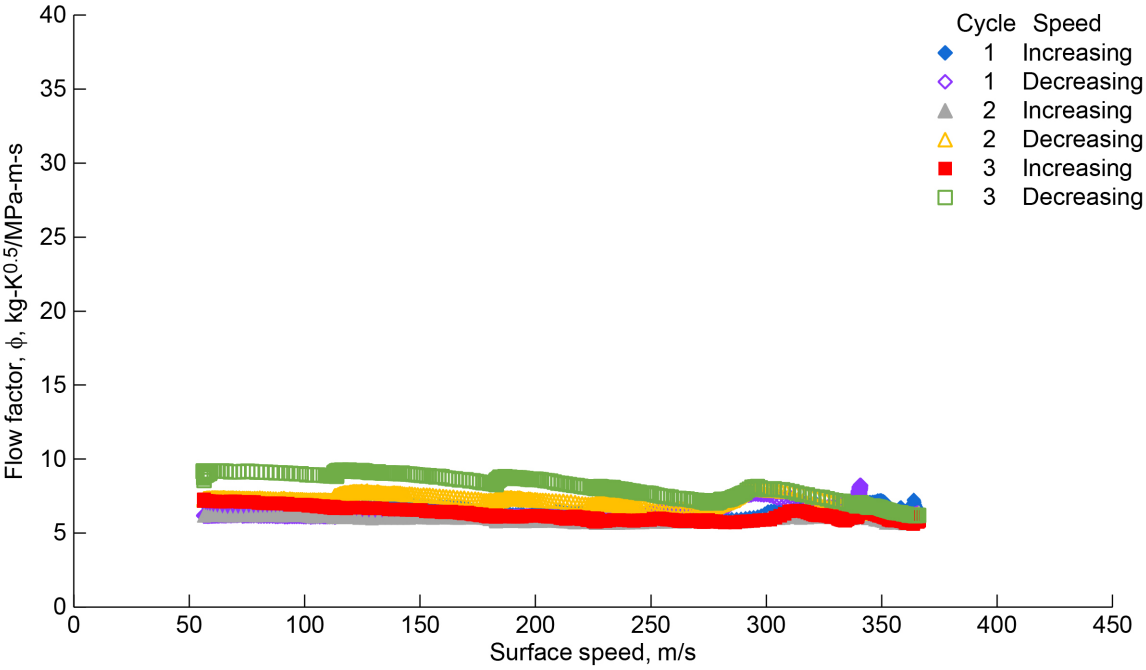

Figure 38.—Leakage performance of NCFS Build 4 with new finger elements at pressure differential of 172 kPa and average seal inlet air temperature of 315 K.

Wear Results

Build 2

A photograph of the NCFS Build 2 after hot static performance tests and prior to the room-temperature lift-off test is shown in Figure 39(a). The discoloration from high-temperature static tests gives insight into the flows within the seal, such as the wedge shape expanding from the center of the lift pad where there is a gap between the forward fingers. The seal was examined after the room-temperature lift-off test, and light burnish marks were found on some of the fingers. The burnish marks were on the ID of the forward finger and on the seal land of the aft finger near the heel of the finger foot (Figure 39(b)). More substantial rub marks were found after the room-temperature performance test at 69 kPa pressure differential across the seal as shown in Figure 39(c). Shiny burnish marks are visible on the entire ID of the forward fingers and on the seal land of the aft finger. Burnish marks are also found just downstream of the circumferential groove on the aft finger lift pad and in some cases extend to the middle of the lift pad near the trailing edge or heel of the lift pad, creating triangular wear marks. There was no measurable change in the weight of the seal after this dynamic performance test. Figure 40(a) shows the rotor surface prior to static and dynamic performance tests, and Figure 40(b) shows the rotor after the room-temperature performance test at 69 kPa pressure differential. Wear occurred around the entire circumference of the rotor surface just upstream of the herringbone grooves, on the upstream half of the upstream herringbone grooves, and in the space between the upstream and downstream herringbone grooves. Because of the wear found, no further testing was done with NCFS Build 2, and the rotor coating was removed and replaced.

Build 7

The progression of wear of NCFS Build 7 is shown in Figure 41. Figure 41(a) shows NCFS Build 7 prior to any testing, and Figure 41(b) shows it discolored after 922 K static testing. Room-temperature lift-off testing resulted in a little wear on just a few lift pads (Figure 41(c)). Room-temperature performance testing at pressure differential of 69 kPa resulted in wear on most lift pads similar to that shown in Figure 41(d). A special inspection was performed after operator error resulted in performance testing at 5,000 rpm at pressure differentials up to 556 kPa. Black particles of debris and more substantial wear were found as shown in Figure 41(e). After room-temperature performance testing at 276 kPa the NCFS Build 7 had substantial wear (Figure 41(f)), including loss of material from the toes of the forward finger feet (Figure 41(g)).

Recall that NCFS Build 7 was tested on a smooth rotor since the axial taper in the lift pads provides the hydrodynamic lift. Because wear on the seal extends over the whole axial length of the seal, it is not surprising to see the wide wear tracks on the rotor that were photographed after the room-temperature performance tests at 69 kPa (Figure 42(a)) and at 276 kPa pressure differential (Figure 42(b)).

Build 3

Figure 43(a) and (b) show the NCFS Build 3 prior to and after the room-temperature lift-off test, respectively. After the lift-off test some wear is found on some lift pads, but most lift pads have no wear. The rotor was examined while still installed in the test rig with a mirror, and the herringbone grooves were found to be in good condition as shown in Figure 44(a). After the room-temperature performance test at 69 kPa and speeds up to 25,000 rpm more wear is visible on the seal (Figure 43(c)), but the herringbone grooves still look to be in good condition (Figure 44(b)). After room-temperature performance testing at 69 kPa pressure differential and speeds up to 40,000 rpm, there was substantial wear on all lift pads as shown in Figure 43(d). The rotor also shows wear (Figure 45) that at locations C and D obliterated the herringbone grooves. The fact that the wear is uneven around the rotor indicates either a dynamic event or eccentric motion of the rotor.

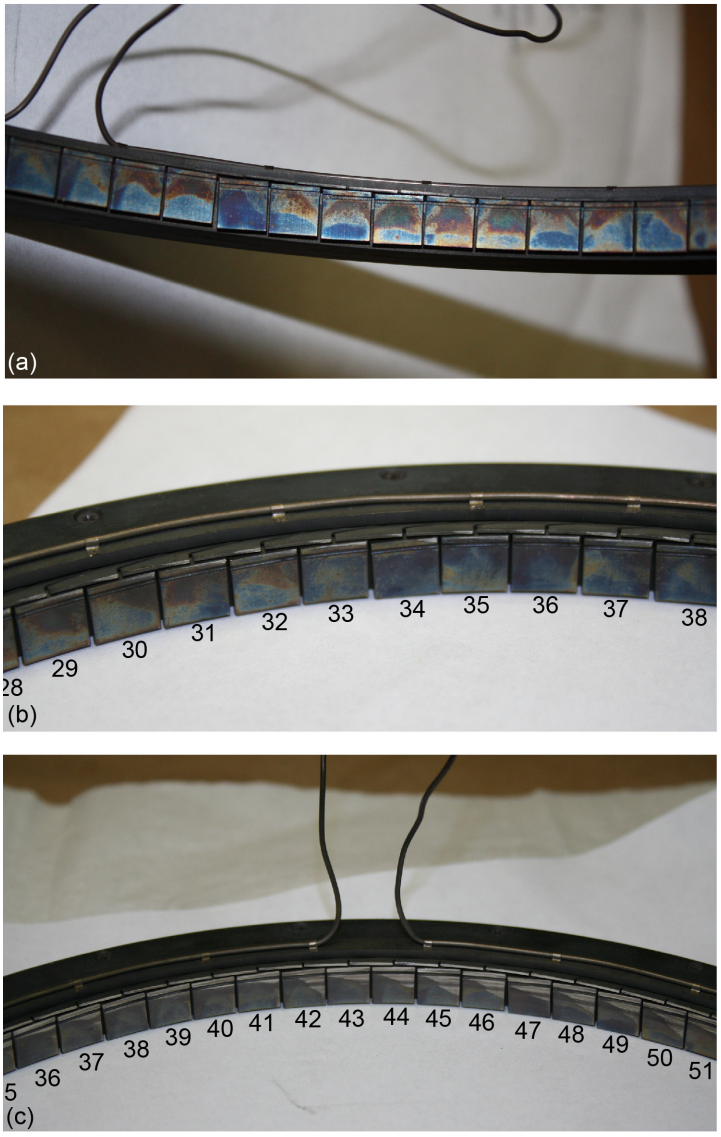

Figure 39.—NCFS Build 2 room-temperature dynamic test wear results. (a) Prior to lift-off test. (b) After lift-off test. (c) After performance test at 69 kPa pressure differential.

Figure 40.—Herringbone-grooved rotor used with NCFS Build 2. (a) Prior to static and dynamic performance tests. (b) After room-temperature performance test at 69 kPa pressure differential.

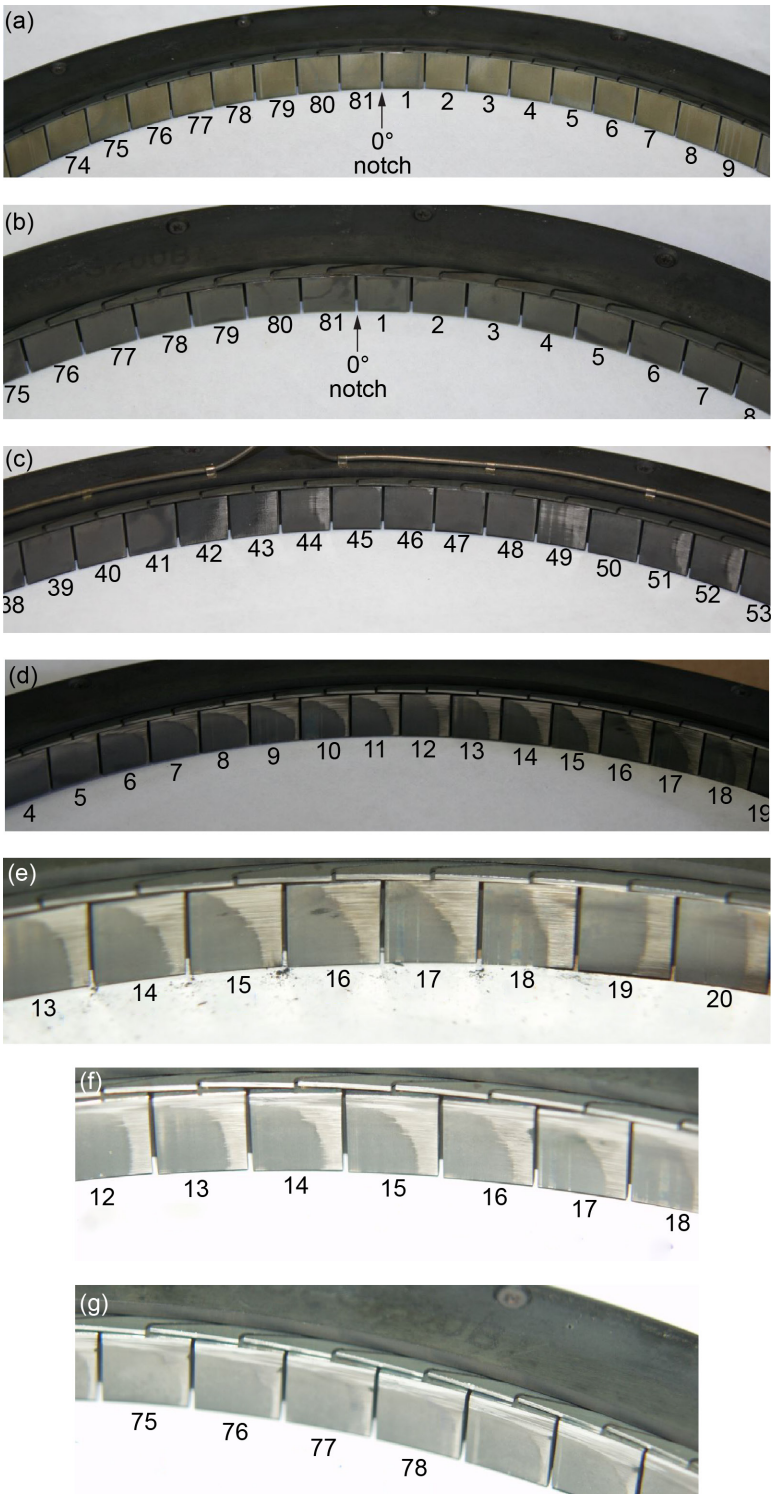

Figure 41.—Progression of wear of NCFS Build 7 during testing. (a) Before test. (b) After 922 K static performance test. (c) After room-temperature lift-off test. (d) After room-temperature performance test at 69 kPa pressure differential. (e) After room-temperature performance test at 5,000 rpm with pressure differential overshoot to 556 kPa. (f) After room-temperature performance test at 276 kPa. (g) After room-temperature performance test at 276 kPa, showing tips of forward finger feet.

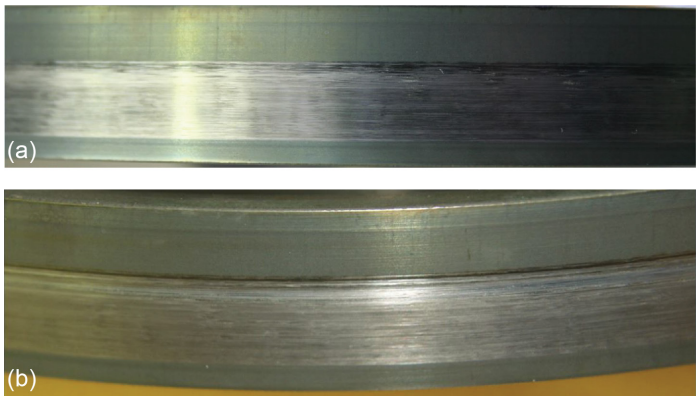

Figure 42.—Rotor wear after room-temperature performance test of NCFS Build 7. (a) At 69 kPa pressure differential. (b) At 276 kPa pressure differential.

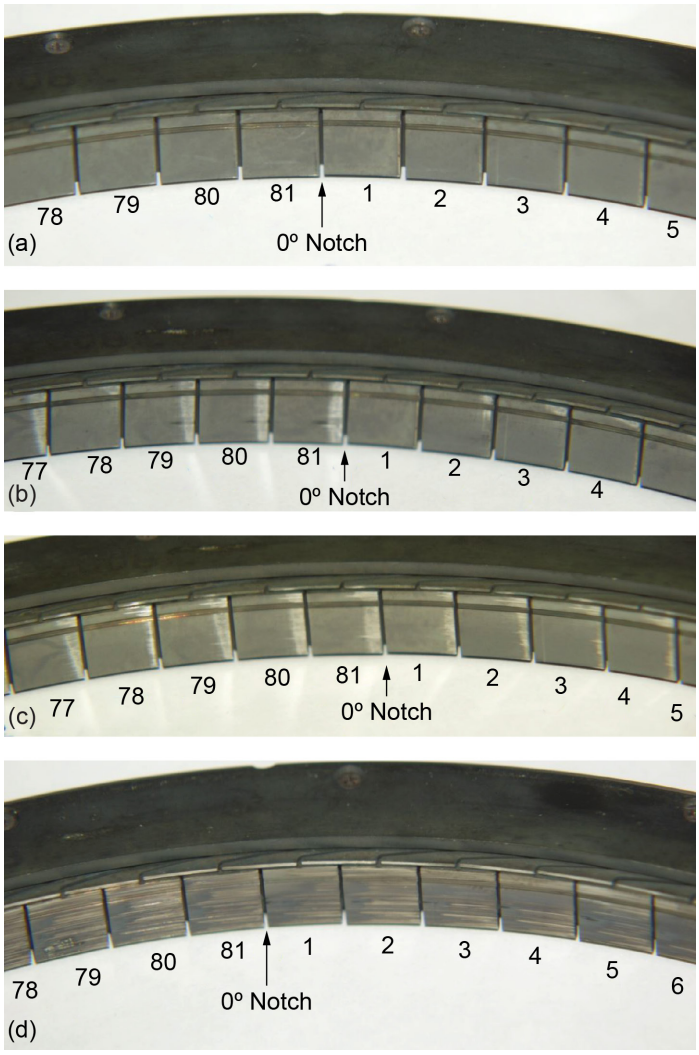

Figure 43.—NCFS Build 3 wear during room-temperature dynamic tests. (a) Prior to lift-off test. (b) After lift-off test. (c) After performance test at 69 kPa pressure differential and speeds up to 25,000 rpm. (d) After performance test at 69 kPa and 40,000 rpm.

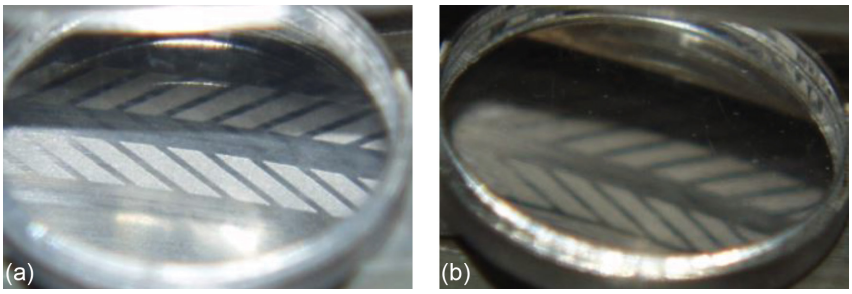

Figure 44.—Wear results for NCFS Build 3 herringbone grooves. (a) After room-temperature lift-off test. (b) After room-temperature performance test at 69 kPa pressure differential and speeds up to 25,000 rpm.

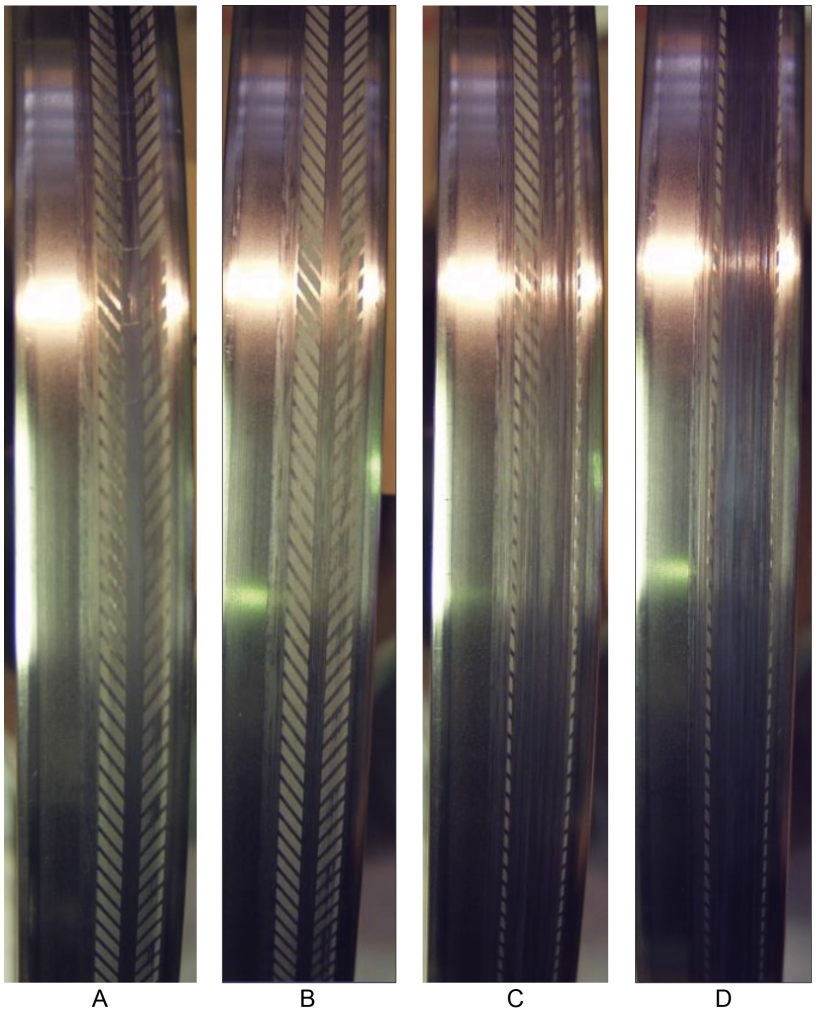

Figure 45.—Rotor OD after room-temperature performance test of NCFS Build 3 at 69 kPa pressure differential and 40,000 rpm at four equally spaced locations around the circumference: A, B, C, and D.

Build 4 With New Finger Elements

A pretest photograph of NCFS Build 4 with new finger elements is shown in Figure 46. Inspection after the room-temperature lift-off test found some fingers with no wear and some with light wear marks as shown in Figure 47. After the room-temperature performance test with 69 kPa pressure differential, the fingers that had no wear after the lift-off test show wear on the forward fingers and on the seal land of the aft fingers (Figure 48(a)), and some fingers have more wear on the aft fingers near the trailing edge of the lift pads (Figure 48(b)). The wear patterns on the seal do not change significantly after the performance tests at 69 kPa pressure differential at 533 and 922 K, as can be seen in Figure 49 and Figure 50, respectively, although the temperature did discolor the seal. Increased pressure differential plays a significant role in the seal wear. Figure 51 shows the NCFS Build 4 after the room-temperature performance test at 172 kPa pressure differential. After this test, the fingers in Figure 51(a) now show wear on the lift pads aft of the seal land, and the fingers in Figure 51(b) show more pronounced wear. Wear can be seen on the forward finger ID near the heel of the finger foot, on the seal land of the aft finger, and across the lift pad from midpad to the trailing edge.

Figure 52 shows the progression of wear on the herringbone-grooved rotor. Except for the pretest and post-room-temperature performance test at 172 kPa pressure differential, the inspections were made using a mirror while the rotor was still installed in the test rig. Compared to pretest (Figure 52(a)), the herringbone grooves look to be in excellent condition after the room-temperature lift-off test (Figure 52(b)) and after the 533 K performance test at 69 kPa (Figure 52(c)). Light wear marks on the upstream portion of herringbone grooves are first obvious after the 922 K performance test at 69 kPa pressure differential (Figure 52(d)). The herringbone grooves on the rotor after the room-temperature performance test at 172 kPa for NCFS Build 4 with new finger elements (Figure 52(e)) show substantial wear in the upstream set of grooves and on the land between the upstream and downstream grooves as well as some wear in the downstream set of grooves.

Figure 53 shows a comparison of the finger wear to the wear on the rotor.

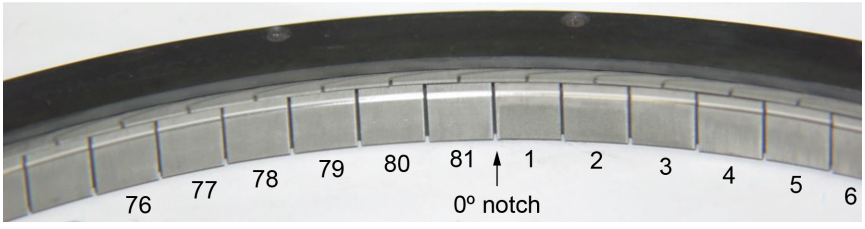

Figure 46.—NCFS Build 4 with new finger elements, pretest.

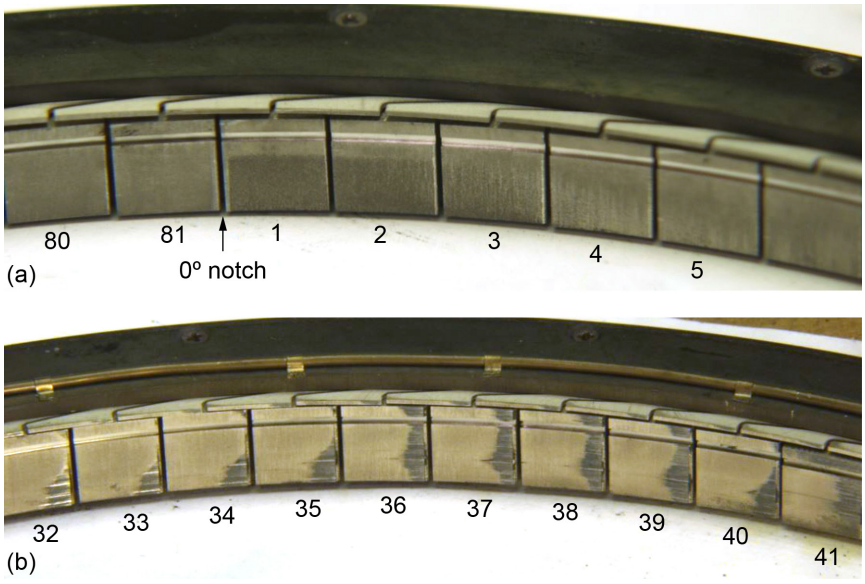

Figure 47.—NCFS Build 4 with new finger elements after room-temperature lift-off test. (a) Some fingers with no wear. (b) Some fingers with light wear.

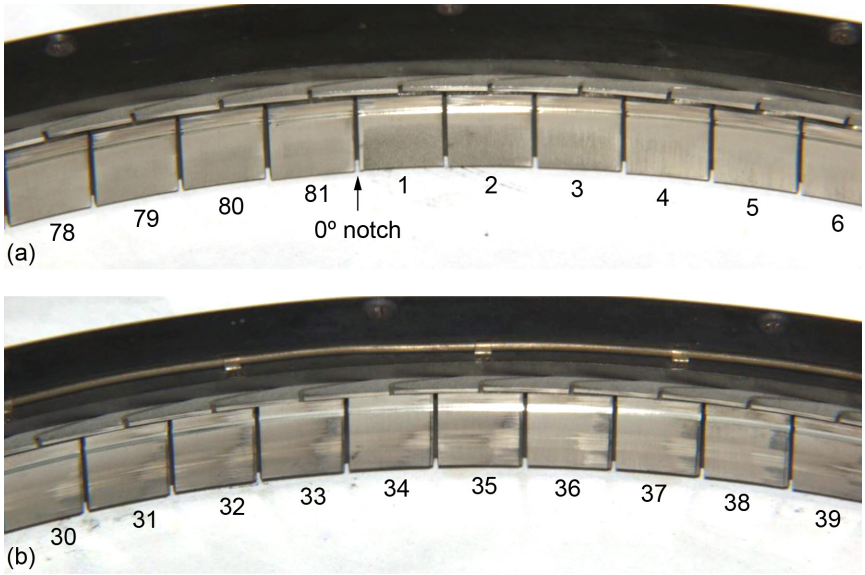

Figure 48.—NCFS Build 4 with new finger elements after room-temperature performance test at 69 kPa pressure differential. (a) Wear on some forward fingers and seal land of aft fingers. (b) Wear on some aft fingers near trailing edge of lift pads.

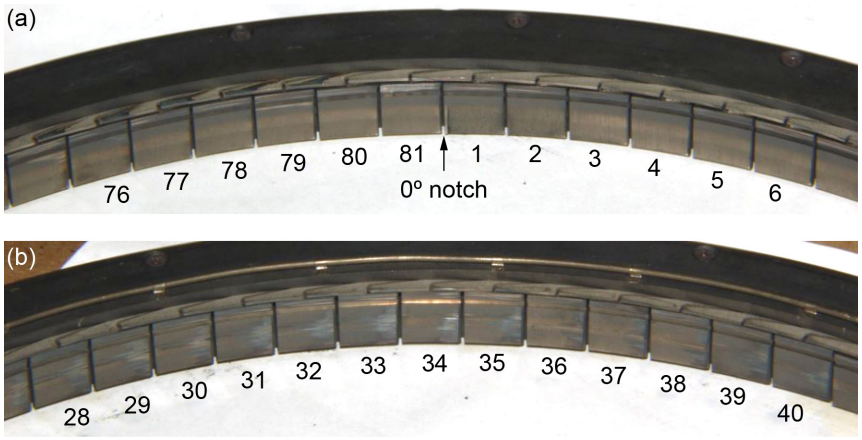

Figure 49.—NCFS Build 4 with new finger elements after 533 K performance test at 69 kPa pressure differential. (a) Wear on some forward fingers and seal land of aft fingers. (b) Wear on some aft fingers near trailing edge of lift pads.

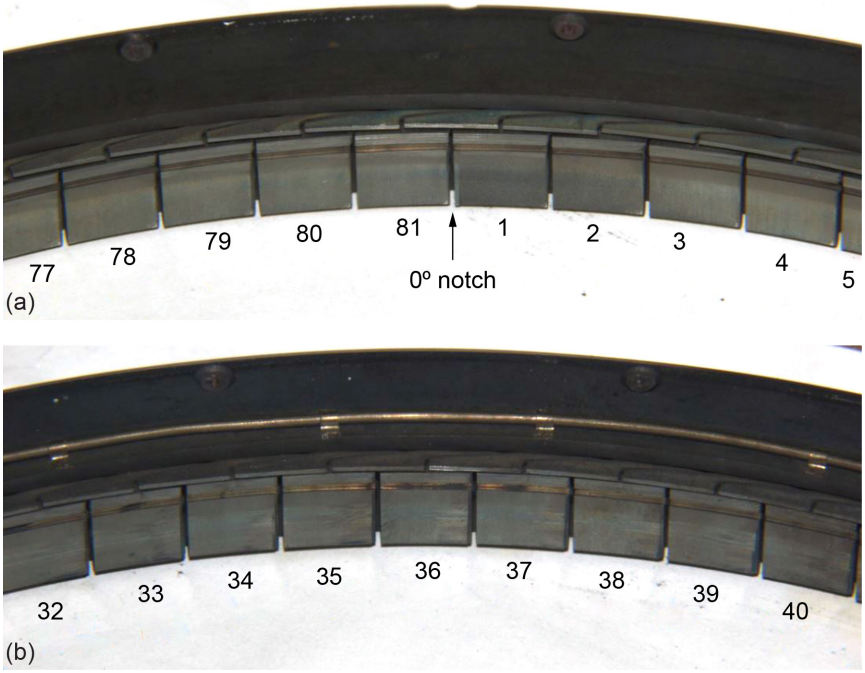

Figure 50.—NCFS Build 4 with new finger elements after 922 K performance test at 69 kPa pressure differential. (a) Wear on some forward fingers and seal land of aft fingers. (b) Wear on some aft fingers near trailing edge of lift pads.

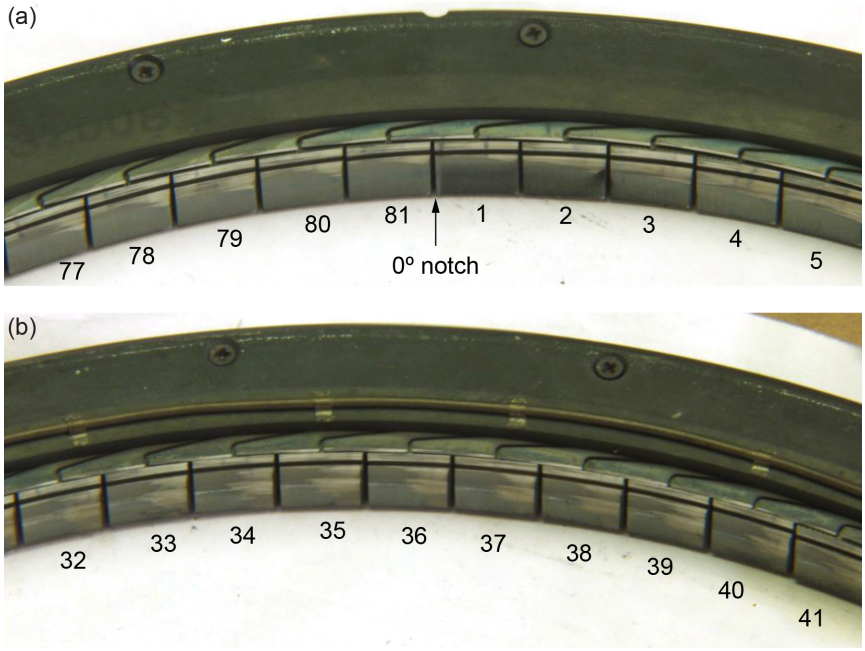

Figure 51.—NCFS Build 4 with new finger elements after room-temperature performance test at 172 kPa pressure differential. (a) Wear is on lift pads aft of seal land on these fingers. (b) More pronounced wear.

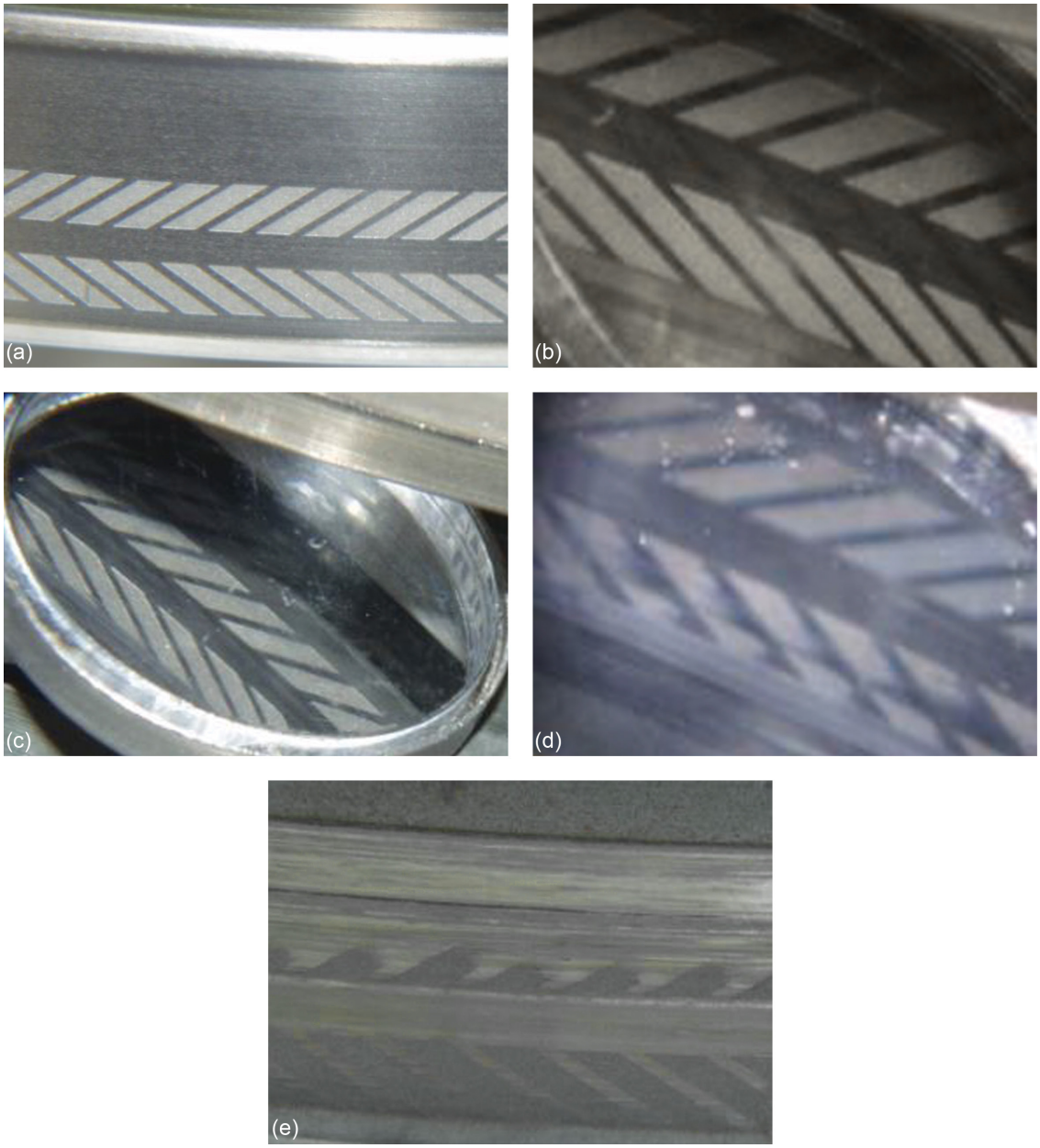

Figure 52.—Progression of wear on herringbone-grooved rotor from dynamic testing of NCFS Build 4 with new finger elements. (a) Pretest. (b) After room-temperature lift-off test. (c) After 533 K performance test at 69 kPa. (d) After 922 K performance test at 69 kPa. (e) After room-temperature performance test at 172 kPa.

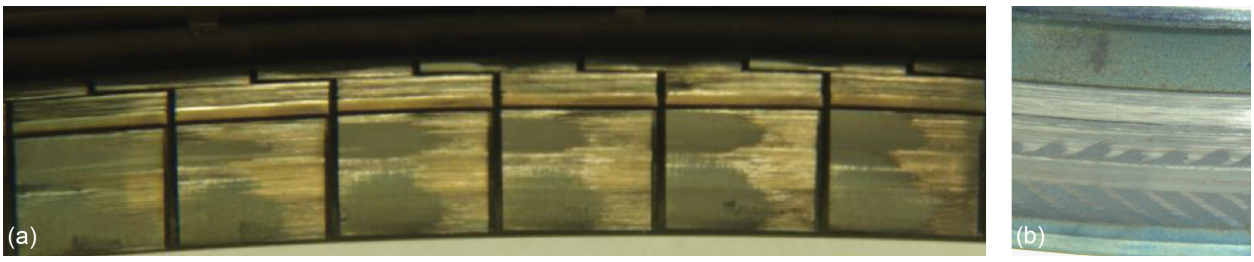

Figure 53.—Comparison of wear on rotor and on lift pads of NCFS Build 4 with new finger elements after room-temperature performance test at 172 kPa. (a) Lift pads. (b) Herringbone grooves.

Summary and Conclusions From Dynamic Testing

In summary, performance tests were conducted on four builds of the NCFS: Builds 2, 7, 3, and 4 (with new finger elements). Room-temperature performance tests were conducted at 69 kPa pressure differential and 40,000 rpm for NCFS Builds 2, 3, and 7; at 172 kPa and 38,000 rpm and at 276 kPa and 35,000 rpm for NCFS Build 7; and at 69 kPa and 32,355 rpm and at 172 kPa and 20,000 rpm for NCFS Build 4. High-temperature performance tests were conducted at 700 and 922 K at 69 kPa pressure differential for the NCFS Build 4 with new finger elements. Increased inlet air temperature resulted in higher flow factors. Spikes in the measured flow factor data indicate an opening of the seal clearance at or near resonant frequencies of the rotor. Comparison of the test results at room temperature and 69 kPa shows that the NCFS Build 4 had the lowest leakage flow factor, although flow factors for NCFS Build 7 were similar. NCFS Builds 2 and 3 had substantially higher flow factors than Build 4.

Little wear occurred during lift-off testing with pressure differential of 14 kPa across the seal and low speed of 5,000 rpm for all the seals tested dynamically. However, increased pressure differential, which increases the pressure closing force, and increased speed, which reduces the seal clearance due to centrifugal growth of the rotor, resulted in wear of the seal and rotor in all cases tested. Apparently, the seals tested did not generate enough hydrodynamic lift to overcome the pressure closing force and/or did not respond quickly enough to the inherent dynamic rotor motion to prevent rubbing contact. Wear patterns on the lift pads indicate that the lift pads are not remaining concentric to the rotor as intended. Any change to the flow path geometry affects the fluid forces on the seal and the stiffness of the fluid film between the rotor and seal. Fluid and structural modeling is needed to guide future design modifications.

Modeling Effort

During static testing it was found that the seal would bind the shaft when the pressure differential was increased to a certain level, nominally 276 kPa. To explore this phenomenon a modeling effort was undertaken to examine the loads within the seal. Both computational fluid dynamics (CFD) and structural models were developed using ANSYS FLUENT and ANSYS Mechanical software (ANSYS, Inc., Canonsburg, PA), respectively. The CFD model was used to predict the pressures within the seal and the mass leakage rate using experimental inlet and outlet conditions. These pressures were then applied to the structural model to compute deflections and assess if contact with the rotor would occur.

CFD Models

The CFD code ANSYS FLUENT, which uses a finite volume method to discretize the continuity, momentum, and energy equations, was used for the CFD modeling.

The NCFS concept presented significant complications to producing a useful CFD model. The design presents little symmetry that can be exploited to reduce the domain of the models, and the difference in scale between the smallest and largest significant volumes is quite large. The volume between the lift pads and the rotor is of critical importance and therefore must be accurately represented, which drove the density of the computational grid and carried over into the large volumes above and behind the lift pads. These considerations significantly impact the computing resources required to execute the model and the time required for it to run. These factors, along with an evaluation of the number of builds and test pressures that needed to be modeled, resulted in a limitation to the number of pads that could be included in the model. As a result, two simplified CFD models of a single forward finger and two half-aft fingers were developed. One had a horizontal channel, and the other had a vertical channel, to represent the flow from the pressure balance cavity passing between the aft fingers at the seal dam. In reality, this channel

flow is somewhere between vertical and horizontal. Figure 54 to Figure 56 show the solid model of the NCFS, the simplified CFD model of the fluid volume with a horizontal channel, and typical CFD results showing contours of Mach number, respectively. It can be seen in Figure 55 that the simplified CFD model has no curvature of the finger sticks or the finger feet, which is a reasonable assumption since the radius of curvature is very large compared to the radial clearance or the gaps between the fingers. The rotor was treated as a smooth, stationary wall, which means hydrodynamic loads created from rotation and clearance changes due to the herringbone grooves were not included. CFD models with horizontal and vertical channels were built for NCFS Builds 1, 2, 3, and 4 using as-built dimensions. The models were run with seven sets of inlet and outlet conditions obtained from the experiments with the as-built clearance. Additional cases were run with different radial clearances. Periodic boundary conditions were used with a steady-state, compressible-flow model.

Two different grid densities were examined to establish that the solutions were grid independent. For the models of the different builds, the number of cells in the coarse grid were increased approximately 300 percent for Builds 1 and 2 and approximately 150 percent for Builds 3 and 4 to arrive at the fine grids. For the differing gap heights, the number of cells in the coarse grid was increased approximately 120 percent to arrive at the fine grids. Although Reynolds numbers indicated laminar flow, the possibility that the flow could locally become turbulent led to an examination of predictions using a laminar flow model and a shear stress transport (SST) k-ω turbulence model. Polynomial expressions in terms of temperature were used for the heat capacity, thermal conductivity, and viscosity of air.

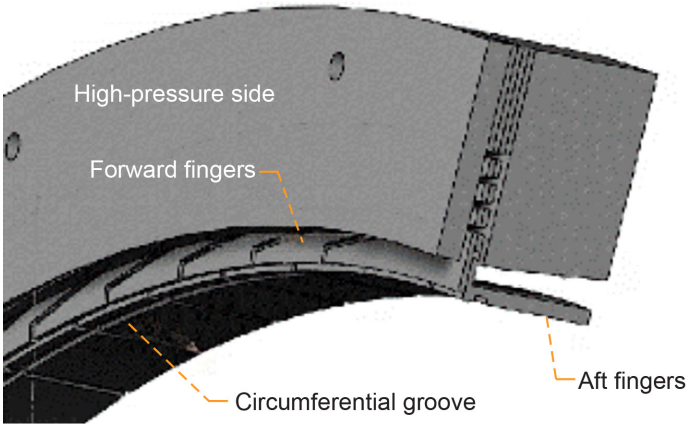

Figure 54.—Solid model of NCFS.

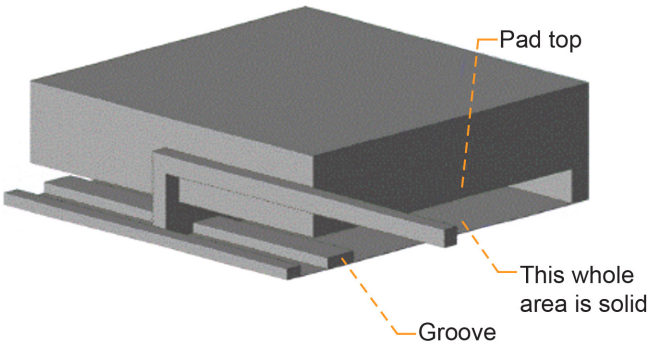

Figure 55.—Simplified CFD model of NCFS.

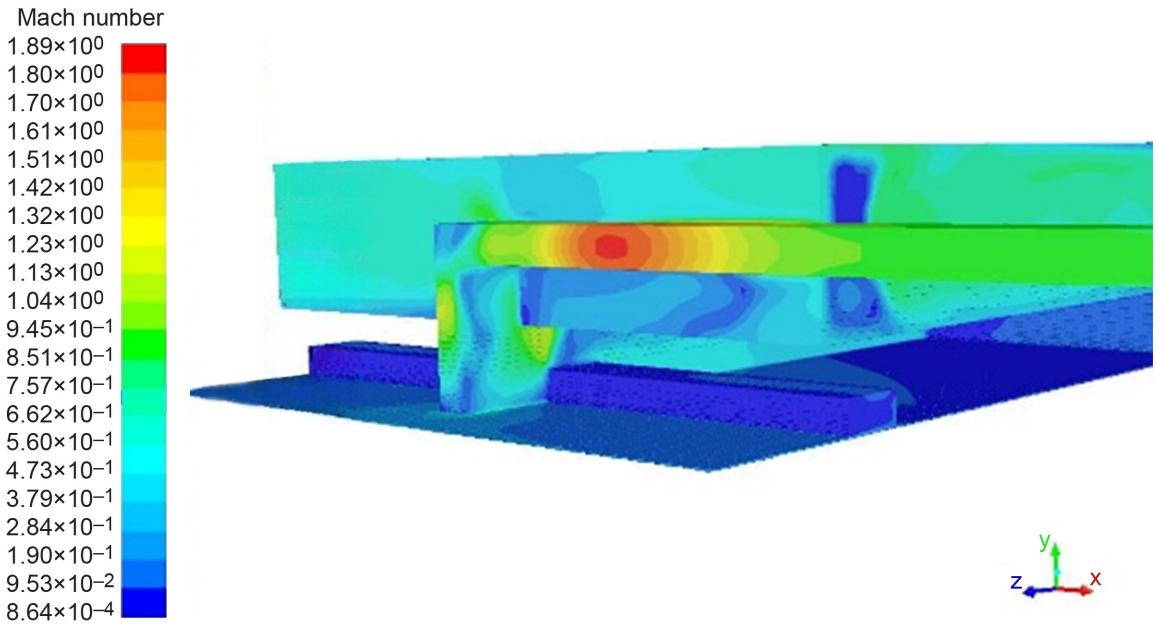

Figure 56.—Typical results of simplified CFD model of NCFS, showing contours of Mach number.

The solution setup consisted of a coupled pressure-velocity coupling scheme and a spatial discretization that is least squares cell based for the gradient; standard for pressure; second-order upwind for momentum and energy; and for the turbulent-flow models, first-order upwind of turbulent kinetic energy and specific dissipation rate. The flow Courant number was set to 50. Explicit relaxation factors of 0.5 were used for momentum and pressure. Under-relaxation factors were set at 1 for density, body forces, turbulent kinetic viscosity, and energy; for the turbulent flow models, they were set to 0.8 for turbulent kinetic energy and specific dissipation rate. There were isolated cases in which the explicit relaxation factors had to be decreased to 0.4, or the under-relaxation factor had to be decreased to 0.9, to avoid divergence in the solution. This indicates that the solution settings are not yet optimized for these models. The convergence criteria were set as scaled residuals below 1×10^{-6} for the energy equation and 1×10^{-5} for all other equations. Scaled residuals for continuity rarely met these criteria, generally going no lower than about 1×10^{-3}. Examination of results at varying numbers of iterations of the solution indicated 2,000 iterations was sufficient for the predictions to cease changing. A nonuniform grid was used over parts of the model to minimize the total number of computational cells.

Figure 57 shows the pressure contours on the NCFS Build 1 seal ID at a pressure differential of 276 kPa resulting from the CFD analysis of the simplified model with horizontal channel using periodic boundary conditions and laminar flow. The high inlet pressure acts on the ID of the forward finger since NCFS Build 1 forward finger has a large radial clearance. The contour of 179 kPa pressure extends approximately one-third of the distance between the circumferential groove and the aft edge of the pad at the center of the lift pad. (The outside edges of the two half-aft pads are the center of the lift pad.) This lines up with the gap between the forward fingers, which acts as a point source of pressure to the aft fingers. Near the gap between the lift pads, the pressure drops off quickly just after the circumferential groove. To simplify the structural modeling, area average pressures were calculated from CFD analysis results so that a uniform pressure could be applied to the different surfaces in the structural model.

Build 4 was chosen to be the verification case. The CFD model slightly underpredicts flow factor but has the same trend as experimental measurements, as shown in Figure 58. In this figure, “CFD open” means the as-built clearance is open, and “CFD closed” means the radial clearance is zero and there is no

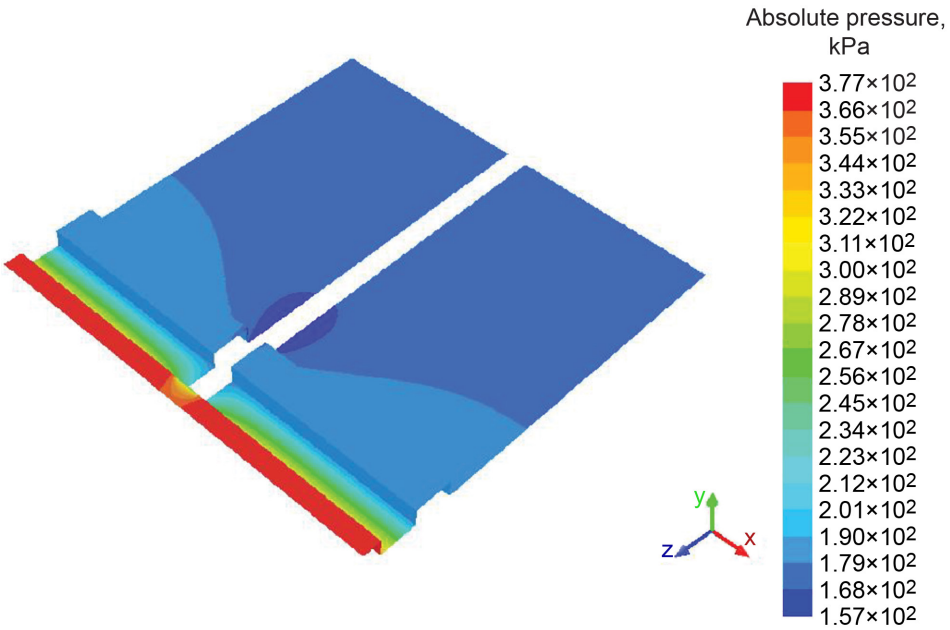

Figure 57.—Contours of absolute pressure on the NCFS Build 1 seal ID at pressure differential of 276 kPa.

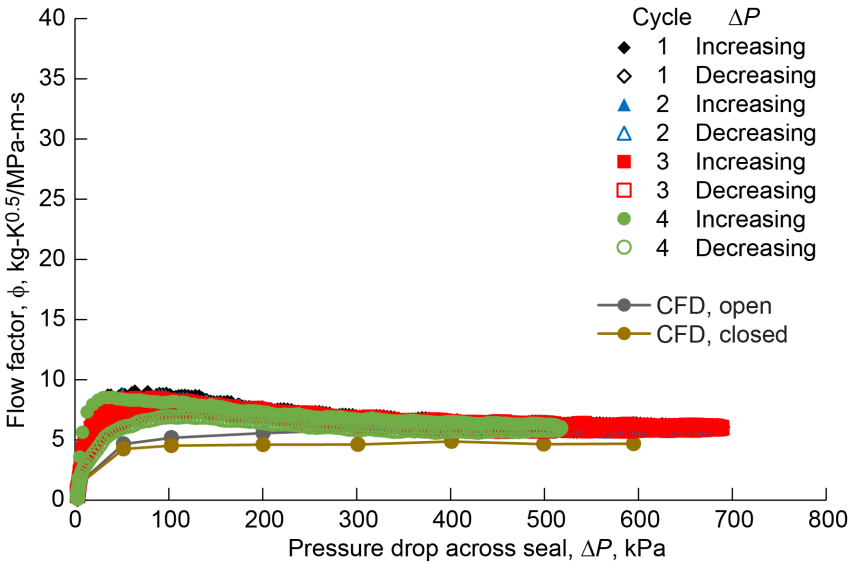

Figure 58.—Comparison of predicted and measured leakage performance of NCFS Build 4.

flow path between the rotor and the seal. Hence, the flow for CFD closed is the flow from the pressure balance cavity over the seal dam. Also, the model shows that the flow goes supersonic near the pressure differentials at which the seal binds up on the rotor.

Subsequent to and in addition to the verification case, flow factors were computed from the CFD analysis results for NCFS Builds 1, 2, and 3 with as-built radial clearances and then compared to room-temperature static leakage performance measurements. Comparisons of predicted and measured leakage performance flow factor for NCFS Builds 1, 2, 3, and 4 are shown in Figure 59 to Figure 62, respectively. Flow factors were predicted using both the model with the horizontal channel and the model with the vertical channel, with coarse and fine grids for each. The experimental data shown are from cycle 3 of the room-temperature static performance tests. In all cases, the predicted flow factors using the coarse and fine grids are in good agreement with each other, and the flow factors predicted using the model with the horizontal channel are greater than those made using the model with the vertical channel. Also, the difference between the predicted flow factors using the model with the horizontal channel and the model with the vertical channel is approximately the same for Builds 1 and 2 and nearly the same for Builds 3 and 4. However, the difference between predicted flow factors from the two models with horizontal or vertical channels for Builds 3 and 4 is greater than for Builds 1 and 2. Furthermore, the model underpredicts the flow factor for all builds, but to a larger degree (a factor of 2.5 to >3) for Builds 1, 2, and 3 compared to Build 4 (a factor of 1 to 2).

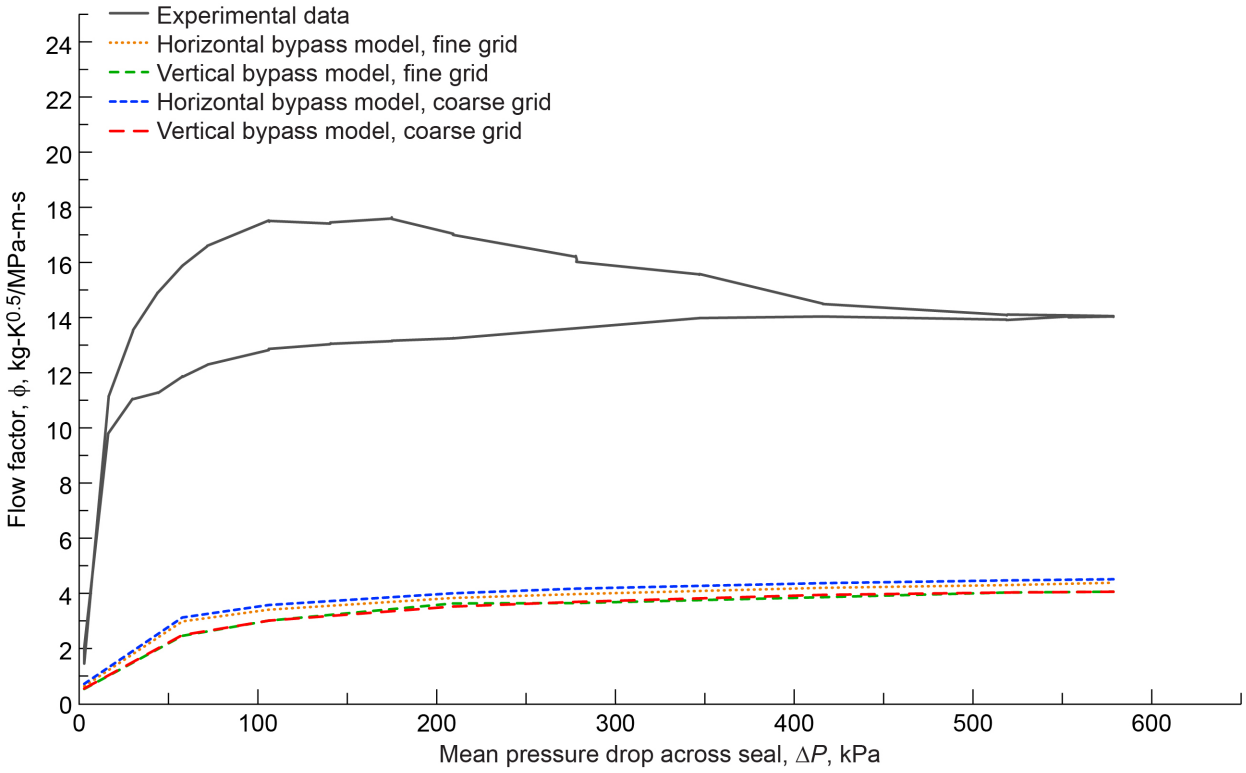

Figure 59.—Comparison of predicted and measured flow factors for NCFS Build 1.

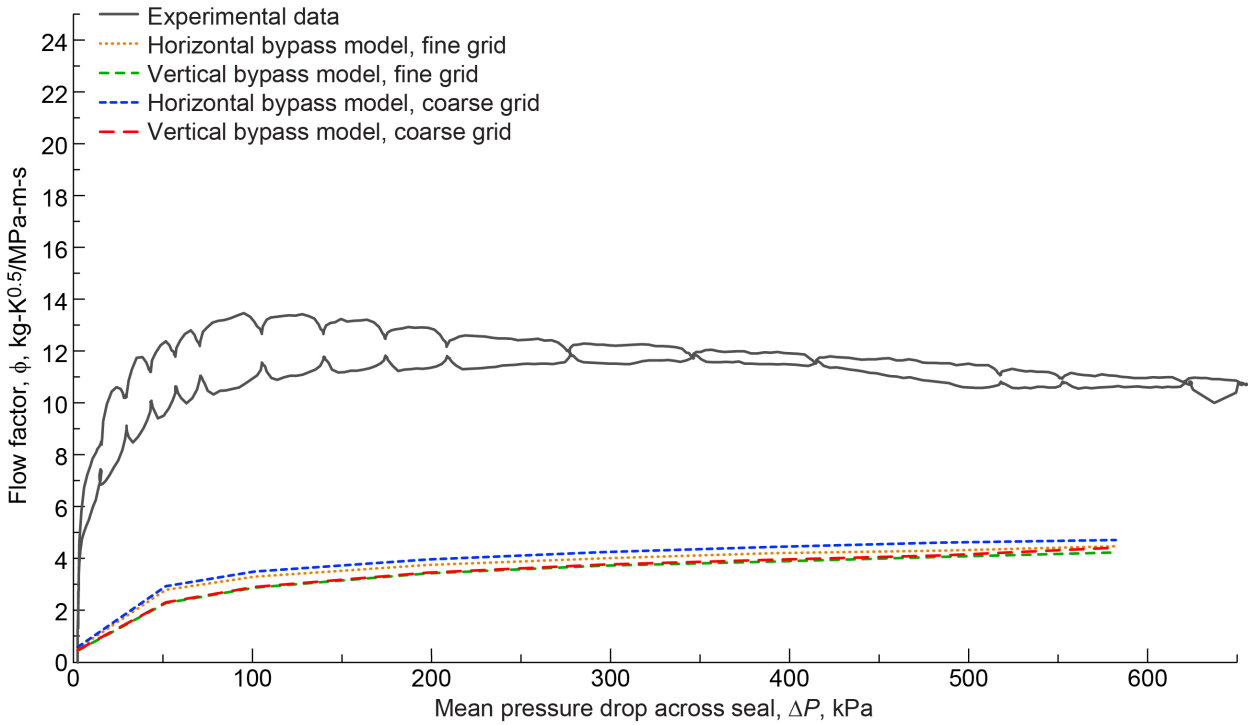

Figure 60.—Comparison of predicted and measured flow factors for NCFS Build 2.

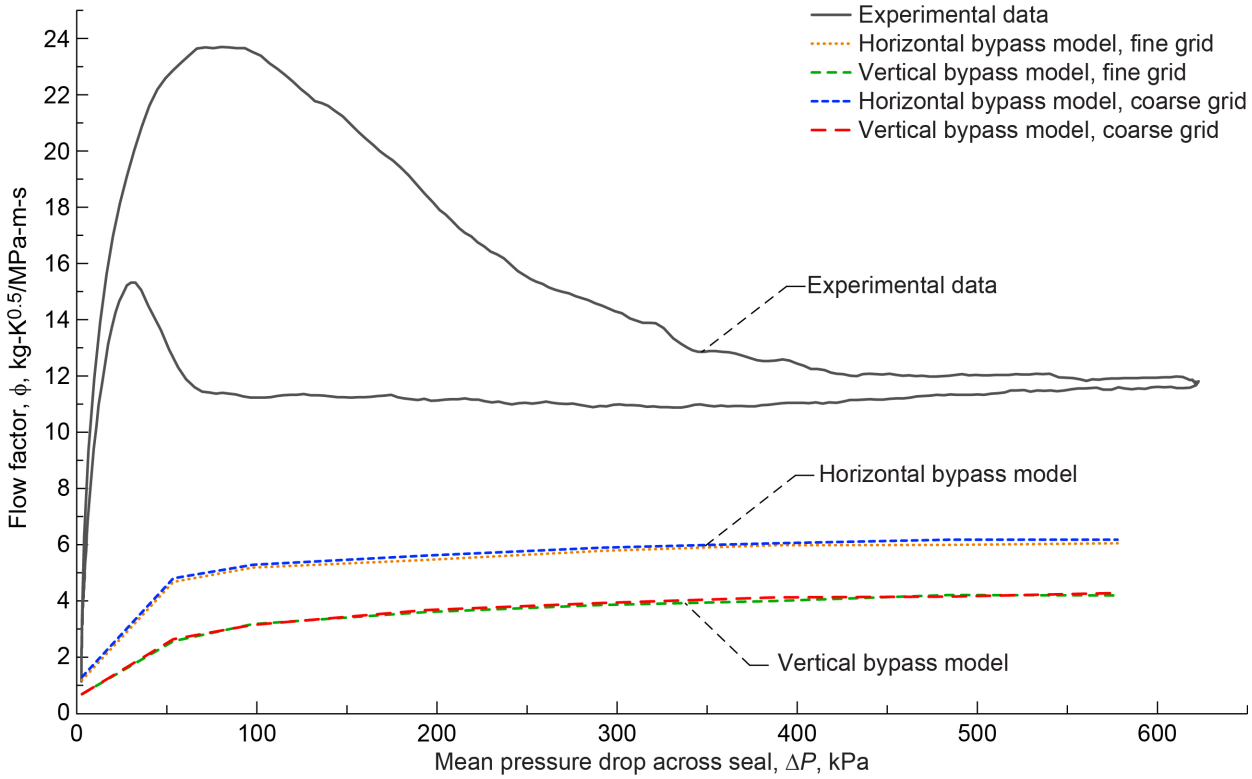

Figure 61.—Comparison of predicted and measured flow factors for NCFS Build 3.

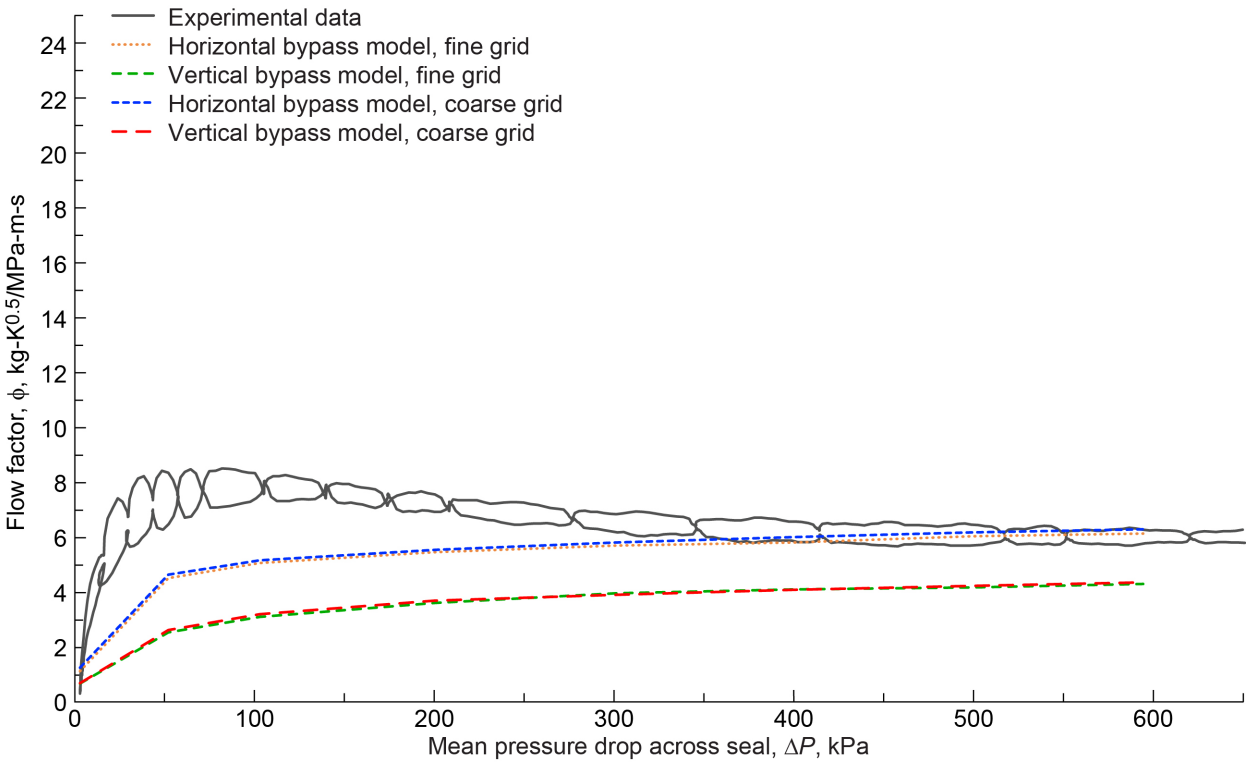

Figure 62.—Comparison of predicted and measured flow factors for NCFS Build 4.

How are these results explained? First, the difference between the predictions made with the horizontal and vertical channels can be explained by the fact that the horizontal channel has more flow resistance because of its longer length (4.6 times longer than the vertical channel) as well as the extra 90° turn compared to the vertical model. Both models have the same inlet and exit pressure conditions, so the model with more resistance requires a greater flow rate to achieve the same pressure drop.

Second, recall that Builds 3 and 4 have the 2× aft finger (i.e., has double the axial finger thickness), and therefore the axial length of the channel and the cross-sectional area of the channel is twice that of Builds 1 and 2. For the same pressure differential, the flow rate through the channel would be greater for Builds 3 and 4 than for Builds 1 and 2. Therefore, the effect of the channel flow on the flow factor would be larger for Builds 3 and 4 than for Builds 1 and 2, which would amplify the difference between the flow factors that result from the models with horizontal and vertical channels.

Third, the difference between the predicted and measured flow factors can largely be explained by the fact that the model assumes a fixed clearance and geometry; however, the fingers deform when pressure is applied to the seal, which changes the radial clearance between the seal and rotor. Figure 63 shows predicted flow factors for NCFS Build 4 with several different radial clearances compared to the measured flow factor as a function of pressure differential. Clearly, flow factor increases with increased radial clearance. Hence it is important to examine the results of the structural model to explain the differences between the measured and predicted leakage performance.

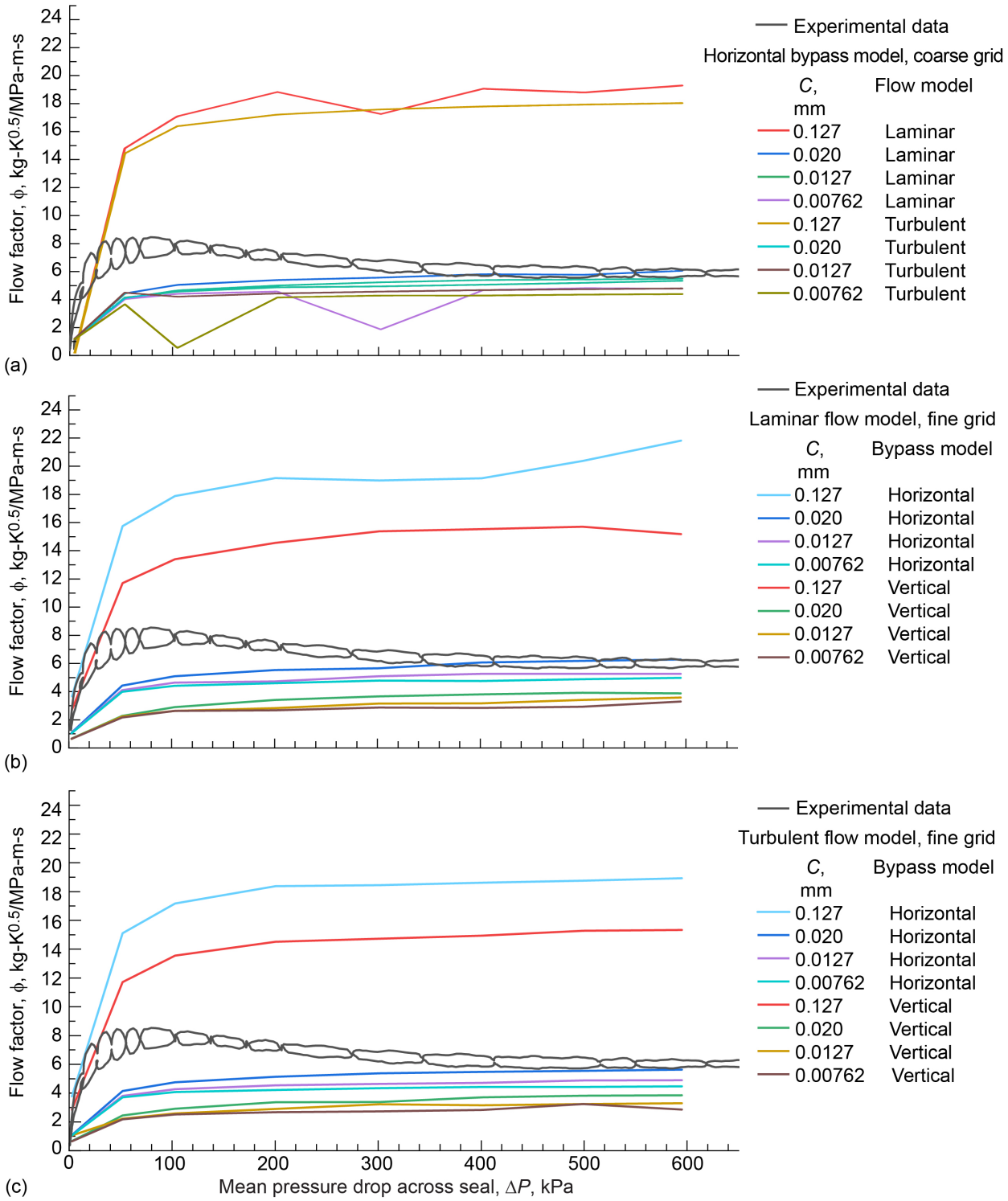

Figure 63.—Comparison of NCFS Build 4 measured room-temperature static performance and predictions made using CFD model for various radial clearances. (a) Coarse grid, horizontal bypass, laminar and turbulent flow models. (b) Fine grid, laminar, horizontal and vertical bypass models. (c) Fine grid, turbulent, horizontal and vertical bypass models.

Structural Models

Based on the experiments and CFD model results, NCFS Build 4 was selected for detailed structural analysis. Two models were developed. The first and simplest model was of a single aft finger. The other was a six-finger model. The six-finger model consists of six entire aft fingers and five entire forward fingers along with two partial forward fingers. The seal dam of the aft spacer was included in the models. The aft face of the aft spacer was treated as a fixed support since it is supported by the back plate. The outer rings of the aft spacer and of the forward and aft fingers were also treated as fixed supports since they are bolted together. The contacts between the forward and aft fingers, and the aft fingers and aft spacer, were assumed to be frictional, with a coefficient of friction of 0.7. The coefficient of friction chosen for the analysis was based on tests performed with Haynes 188, by Coskun, Aksoy, and Aksit (Ref. 13). Both models used room-temperature physical properties of the seal material, Haynes-188, shown in Table VII.

Seven pressure load cases were analyzed using ANSYS Mechanical. The pressures were obtained from the CFD model using experimental inlet and outlet conditions. To simplify the structural modeling, the CFD pressures were averaged for application to 11 different faces in the structural model of the seal. The applied pressure load cases for the seal are summarized in Table VIII. The names of the surfaces in Table VIII refer to the fluid model and require some clarification as to where they are applied. In the single-finger model, the inlet pressure was applied to the forward or upstream face of the aft finger. In the six-finger model it was applied to the forward face of the forward finger as well. The pressure called front finger top was applied to the ID of the forward finger. The location of the surfaces to which the pressures were applied is shown in Figure 64. For the single-finger model and the six-finger model, the pressure for the pad bottom aft was set equal to the pressure on the pad top because the structural analysis failed to solve when the pressure results from the CFD model were used on the pad bottom aft surface. The average pressures from the CFD model for the pad bottom aft surface were larger than those for the pad top, which would tend to lift and tilt the lift pad away from the rotor.

TABLE VII.—PHYSICAL PROPERTIES OF HAYNES 188

Property		Source
Density	8.98 g/cm^3	Haynes International
Dynamic modulus of elasticity	232 GPa	Haynes International
Poisson’s ratio	0.31	MMPDS table 6.4.2.0(b)
Ultimate tensile strength	945 MPa	Haynes International
Yield strength	465 MPa	Haynes International

TABLE VIII.—CFD PRESSURE RESULTS AVERAGED OVER EACH FACE OF NCFS BUILD 4 AND APPLIED TO STRUCTURAL MODEL

Load case	Pressure differential across seal, kPa	Inlet pressure, kPa	Pressure (load), kPa										
			Front finger top	Pad bottom forward (seal land)	Groove			Bypass duct 2	Gap between pads	Pad back	Pad top	Back pad arm	Outlet
					Rear	Front	Top						
1	51.73	149.82	141.29	125.54	117.09	117.05	117.04	103.58	99.03	97.98	98.03	97.23	98.08
2	102.79	201.45	185.34	159.53	145.51	145.36	145.30	109.67	101.35	98.37	98.50	98.22	98.66
3	200.45	300.19	268.84	228.26	206.91	206.51	206.31	116.39	106.29	99.22	99.32	96.78	99.73
4	301.33	402.35	352.40	298.03	271.69	270.99	270.55	124.39	109.93	99.98	100.26	99.74	101.02
5	400.47	503.47	432.42	364.02	334.43	333.43	332.78	128.30	116.01	101.62	101.37	97.91	102.50
6	499.30	603.54	508.12	423.87	392.25	390.93	390.07	139.56	119.01	103.18	102.84	98.14	104.31
7	594.86	701.09	577.18	473.28	440.91	439.18	438.21	151.46	121.39	104.79	104.69	98.27	106.23

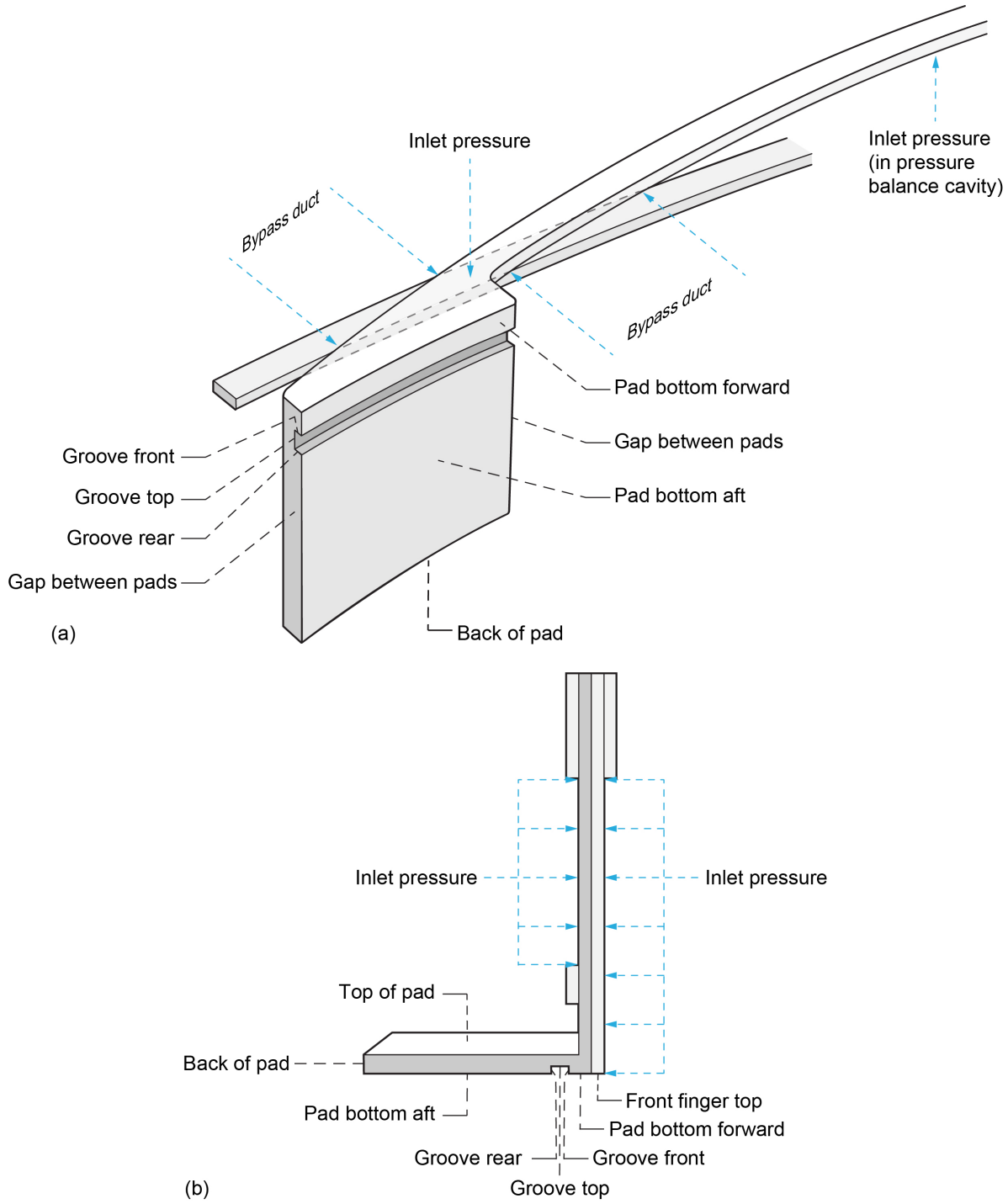

Figure 64.—Surfaces of NCFS Build 4 structural models where CFD model pressures were applied. (a) Single-finger model. (b) Six-finger model.

Single-Finger Model Results

Radial deflections and equivalent stresses for the single-finger model resulting from seven applied pressure differentials are summarized in Table IX. The highlighted radial deflections exceed the as-built radial clearance of 0.02 mm for the aft finger and therefore indicate contact with the seal rotor. Using linear interpolation of the results, the seal would first contact the rotor at a pressure differential of 314 kPa, which is the predicted pressure differential at which bind-up could first occur. Plots of the radial deflection and equivalent stress results for load case 4 at a pressure differential of 301.3 kPa are shown in Figure 65 and Figure 66, respectively, and illustrate typical trends. Radial deflection results are displayed in the cylindrical coordinate system, where the positive x-axis is in the radially outward direction, positive y-axis is in the circumferentially counterclockwise direction when looking at the seal from the high-pressure side, and positive z-axis is in the axially upstream direction. The deflections (Figure 65) show that the downstream edge of the lift pad moves radially outward or away from the rotor with a twist such that the heel of the finger foot at upstream edge moves radially inward. The von Mises equivalent stress is greatest at the inner corner where the finger stick expands to form the finger foot as shown in Figure 66. The stress in the finger foot and lift pad are near zero except near this stress concentration. Most of the stress occurs in the finger stick itself. The stresses from Table IX show that as the pressure differential across the seal increases, stresses increase as well. However, the stresses in the single-finger model do not exceed the 465 MPa yield strength or 945 MPa ultimate strength.

TABLE IX.—RADIAL DEFLECTION AND STRESS RESULTS FROM NCFS BUILD 4 SINGLE-FINGER MODEL

[Model: 2017-07-10_build4_1finger.]

Load case	Applied pressure differential, kPa	Aft finger radial deflection, mm	Max. equivalent stress, kPa	Max. principal stress, kPa
1	51.7	-1.58×10^{-03}	36,568	34,439
2	102.8	-4.23×10^{-03}	68,803	70,906
3	200.5	-1.15×10^{-02}	140,212	148,734
4	301.3	-1.91×10^{-02}	217,054	230,244
5	400.5	-2.59×10^{-02}	292,296	310,057
6	499.3	-3.34×10^{-02}	364,629	386,782
7	594.9	-4.05×10^{-02}	445,450	459,529

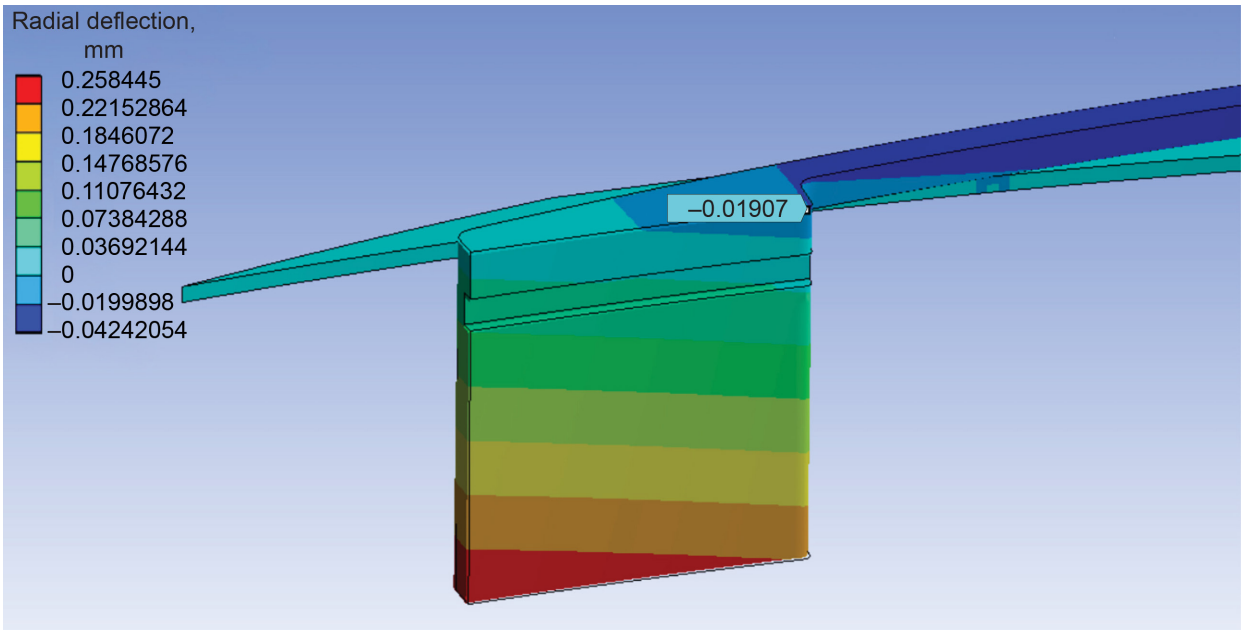

Figure 65.—Radial deflections for single-finger model of NCFS Build 4, load case 4 (301.3 kPa pressure differential).

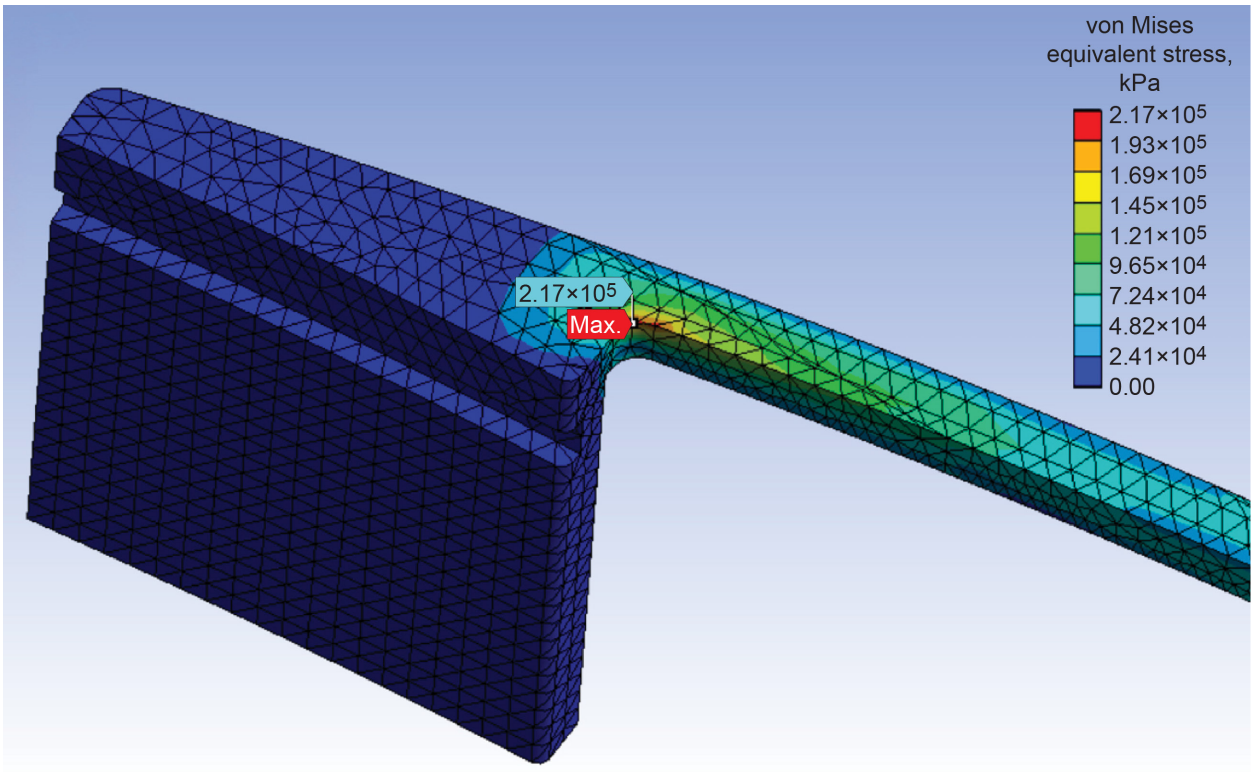

Figure 66.—Equivalent stress in single aft finger of NCFS Build 4, load case 4 (301.3 kPa).

Six-Finger Model Results

Radial deflection and equivalent stress predictions from the six-finger model for the seven applied pressure load cases are summarized in Table X. Maximum deflections and stresses are recorded for the third full finger from the left to avoid unrealistic data from partial fingers. Again, highlighted radial deflections exceed the as-built radial clearance of 0.019 mm of the forward finger and therefore indicate contact with the seal rotor. Although this model is nonlinear because of friction, having an estimate of the bind-up pressure is helpful for comparison with experimental results. So, using linear interpolation of the results, the forward finger of the seal would first contact the rotor at a pressure differential of 414 kPa, which is about 100 kPa higher than predicted by the single-finger model. In this analysis the aft fingers did not deflect enough to hit the rotor.

Stresses are higher on the aft finger than on the forward finger. Therefore, the stresses shown are primarily for the aft fingers. The stresses from Table X show that as the pressure differential across the seal increases, stresses increase as well. As in the single-finger model, the stresses in the six-finger model do not exceed the 465 MPa yield strength or the 945 MPa ultimate strength. However, the stresses in the six-finger model are much lower than the stresses in the single-aft-finger model—because the six-finger model includes both the forward and aft fingers to carry the pressure load.

Radial deflection and equivalent stress results are plotted for load cases 5 and 6, corresponding to 400.5 and 499.3 kPa applied pressures (Figure 67 to Figure 70). Again, the angled contours of deflection indicate a twist with the downstream edge of the lift pad moving away from the rotor and the heel of the finger feet moving towards the rotor. The forward fingers move radially inward. The stress patterns are similar for the forward and aft fingers as seen by comparing Figure 66 and Figure 69. Again, most of the stress occurs in the finger sticks with a concentration near the finger foot.

TABLE X.—RADIAL DEFLECTION AND STRESS RESULTS FOR NCFS BUILD 4 SIX-FINGER MODEL
[Model: 2017-07-07_build4_6finger.]

Load case	Applied pressure differential, kPa	Forward finger deflection, mm	Aft finger deflection, mm	Max. equivalent stress (on third aft finger), kPa	Max. principal stress (on third aft finger), kPa
1	51.7	-9.78×10^{-04}	-6.92×10^{-04}	13,230	8,846
2	102.8	-2.69×10^{-03}	-1.68×10^{-03}	20,380	19,676
3	200.5	-7.01×10^{-03}	-3.44×10^{-03}	67,633	68,565
4	301.3	-1.24×10^{-02}	-6.00×10^{-03}	115,832	118,142
5	400.5	-1.82×10^{-02}	-8.87×10^{-03}	164,247	168,425
6	499.3	-2.39×10^{-02}	-1.21×10^{-02}	205,788	210,614
7	594.9	-2.95×10^{-02}	-1.54×10^{-02}	243,571	249,197

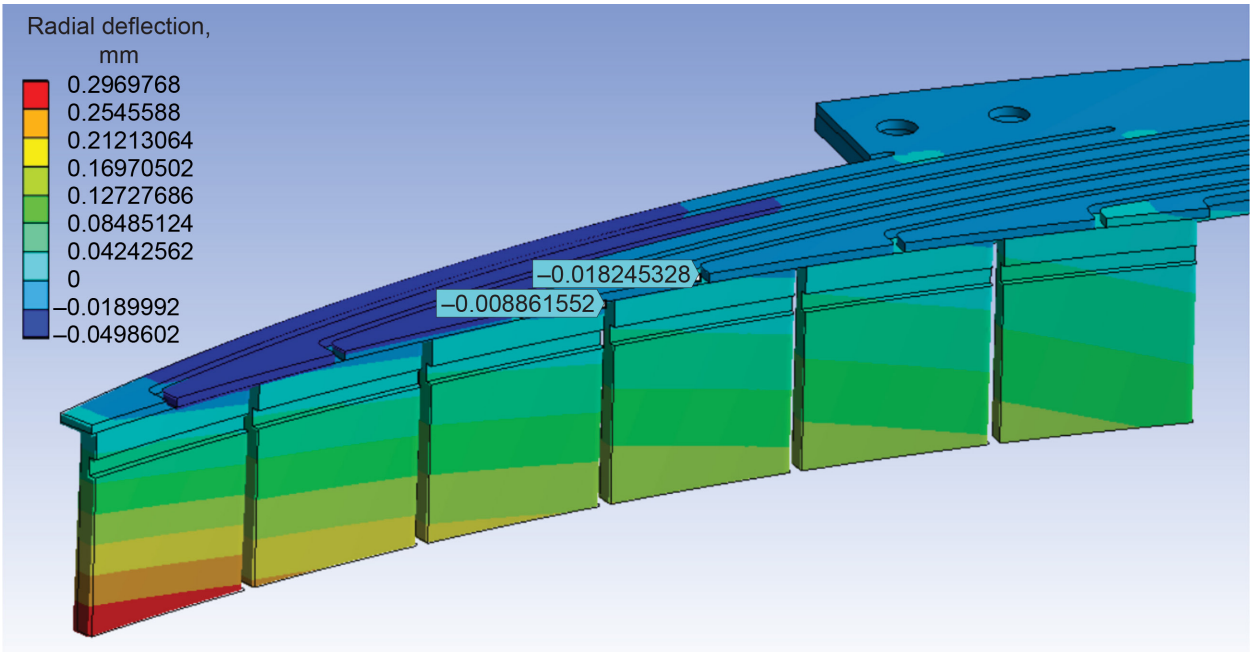

Figure 67.—Radial deflections of NCFS Build 4 predicted with six-finger model at load case 5 (400.5 kPa).

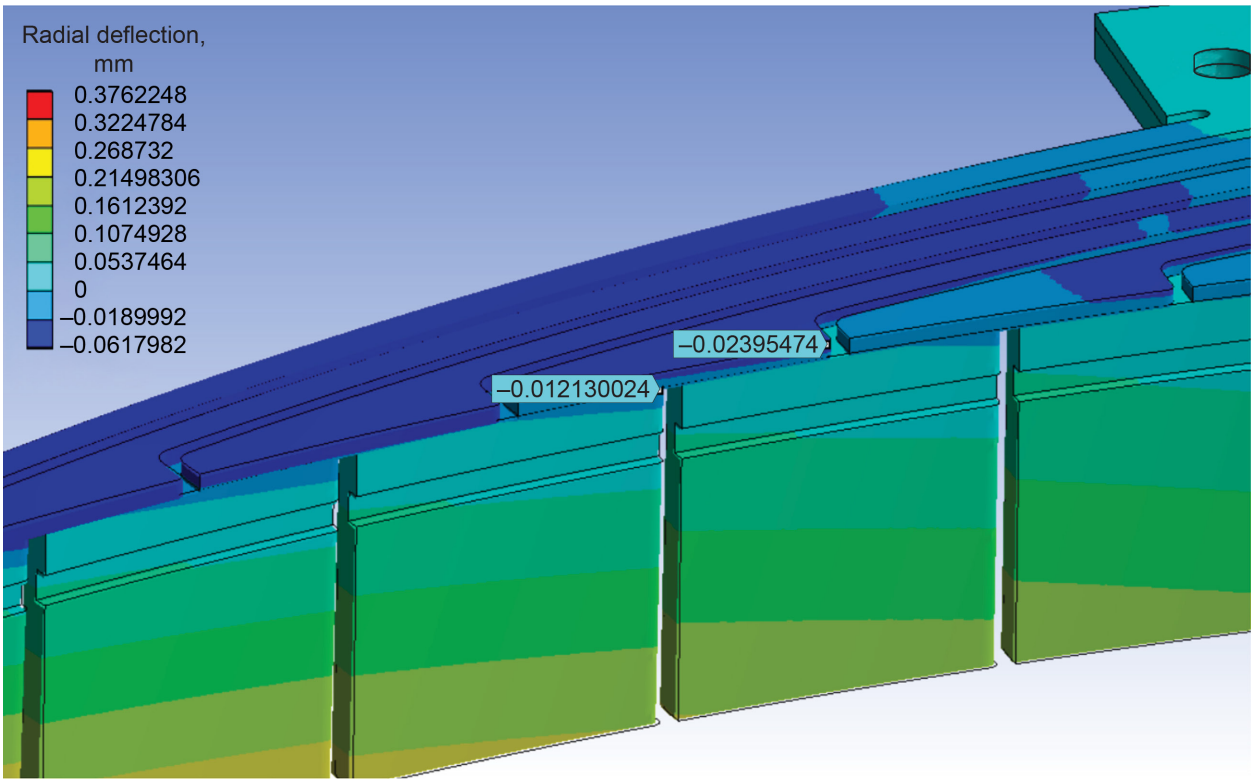

Figure 68.—Radial deflections of NCFS Build 4 predicted with six-finger model at load case 6 (499.3 kPa).

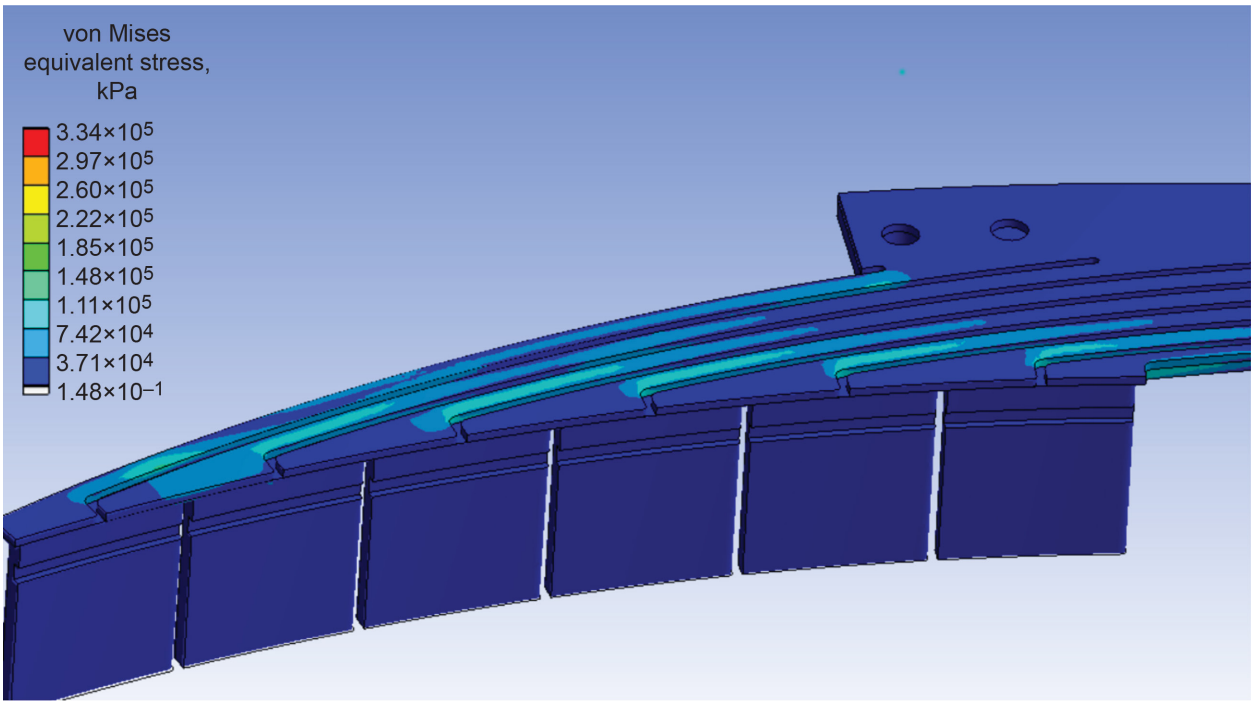

Figure 69.—Equivalent stresses on NCFS Build 4 forward and aft fingers predicted with six-finger model, load case 5 (400.5 kPa).

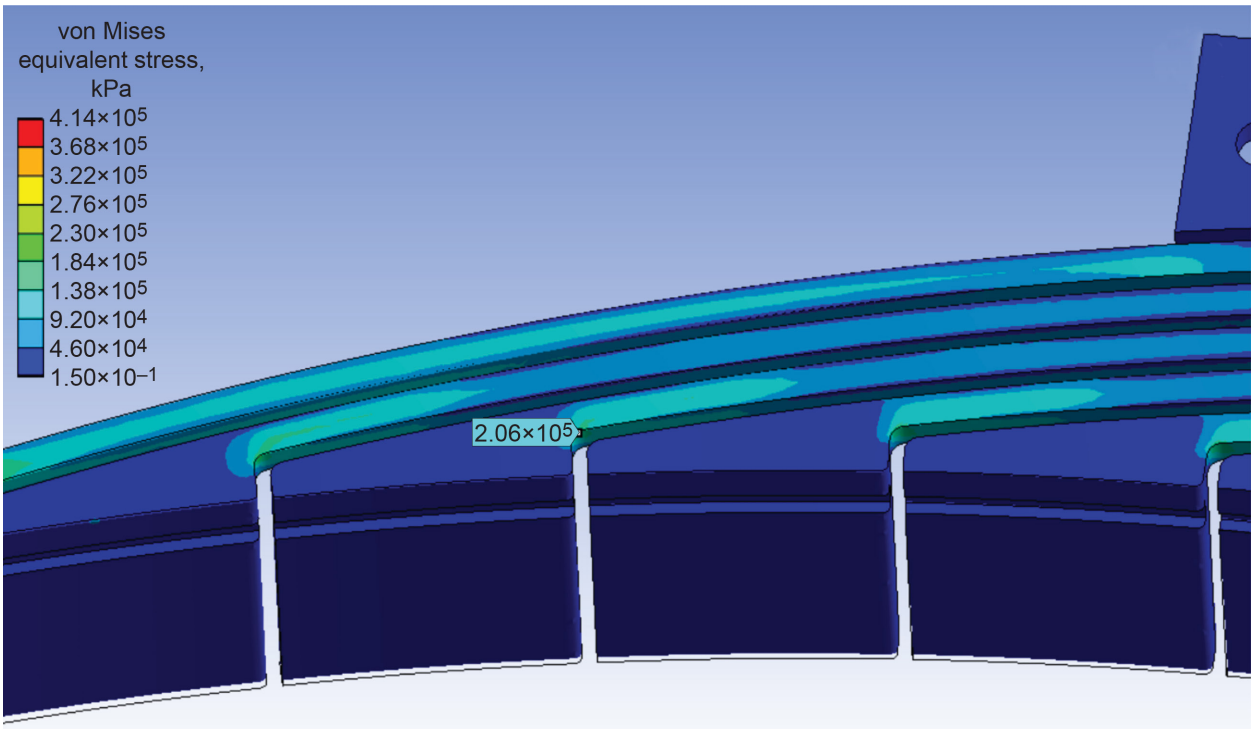

Figure 70.—Equivalent stresses on NCFS Build 4 aft finger predicted with six-finger model, load case 6 (499.3 kPa).

Comparison to Experimental Results

Recall that the bind-up pressure is the pressure differential at which attempting to manually turn the shaft felt tight. The bind-up pressure for Build 4 was 344 kPa (Table VI). The single-finger model predicts that the finger touches the rotor at 314 kPa, which is 9 percent lower than the bind-up pressure. The six-finger model predicted that the fingers touch the rotor at 414 kPa, which is 20 percent higher than the bind-up pressure differential. Whether having some portion of the fingers simply touch the rotor will bind the shaft has not been determined. That would require knowing the reaction force and area of the contact and the coefficient of friction between the seal and rotor to calculate the tangential friction force at the rotor OD. With that information one could compute a torque needed to overcome the binding force. The difference in the pressure differential at which the fingers touch the rotor predicted by the two models is likely because the six-finger model has both forward and aft fingers to carry pressure loads and has more frictional surfaces. It thus makes sense that more pressure would be required to deflect the fingers of the six-finger model the same distance deflected in the single-finger model. The other thing to consider is that the fluid model has a fixed geometry and clearance. However, as pressure is applied and the fingers begin to deflect, the geometry changes and the internal pressures in the seal will change also. Ideally, updated geometry and pressures would pass back and forth between the fluid and structural models, and the pressure profiles from the fluid model would be applied to the structural model rather than a single averaged pressure for each surface, but that is computationally intensive and time consuming. In any event, the simplified modeling approach provides trends consistent with experimental results. This can be seen by comparing the predicted radial deflection shown in Figure 65 and Figure 67 to the wear patterns shown in Figure 51. The locations of maximum inward radial deflections obtained from the analysis are similar to the locations of burnished wear marks on the ID of the low-pressure lift pads near the high-pressure edge. Some pads had this burnishing over the entire circumferential length, and others just had it near a corner near the heel of the finger foot.

Now, the difference between the predicted and measured flow factors will be addressed. The single-aft-finger model for NCFS Build 4, load case 4, with pressure differential of 301 kPa predicted radial deformation at the upstream edge toe and heel of 0.0216 and –0.0194 mm, respectively, which results in an average radial clearance of 0.02148 mm. This clearance is 7.4 percent larger than the as-built clearance used in the CFD model. Knowing that for laminar flow the mass flow rate is proportional to clearance cubed, the mass leakage rate, and hence the flow factor, for the deformed seal would be 1.24 times that of the seal with the as-built radial clearance. This is very nearly the same ratio of the measured and predicted flow factor using the horizontal bypass model for NCFS Build 4 at 301 kPa (load case 4) shown in Figure 62. Similarly, looking at the deformations predicted for the NCFS Build 1 with 276 kPa pressure differential, the flow factor with the deformed average radial clearance of 0.0354 mm would be 3.21 times that of seal with the as-built radial clearance. This too is very nearly the ratio of measured and predicted leakage rates shown in Figure 59 for NCFS Build 1 at 276 kPa pressure differential. These findings show the validity of the leakage predictions and the importance of doing both fluid and structural modeling for this compliant seal design.

Conclusions

The simplified computational fluid dynamics (CFD) models underpredicted the experimentally measured static flow factors for all builds, but they had the same trend as the experimental data. The difference between the predicted and measured flow factors can largely be explained by the fact that the model assumes a fixed clearance and geometry, but the fingers deform when pressure is applied to the seal and changes the radial clearance between the seal and rotor. Iterating between the fluid and structural

models to update the geometry would improve the leakage predictions. The predicted deflections show that the downstream edge of the lift pad moves radially outward from the rotor with a twist such that the heel of the finger foot at the upstream edge moves radially inward. Stresses in the six-finger structural model are much lower than the stresses in the single-aft-finger model, because the six-finger model includes both the forward and aft fingers to carry the pressure load. The computed stresses from either model did not exceed yield or ultimate strength. Most of the stress occurs in the finger stick, and a stress concentration occurs at the inner corner near where the finger stick expands to form the finger foot. Wear patterns on the inner surfaces of the seal are consistent with predicted radial deflections of the lift pad and validate the modeling.

Because wear occurred for all the noncontacting finger seal (NCFS) builds dynamically tested at the relatively low pressure differential of 69 kPa, these specific geometries of the NCFS would not be suitable for the high-overall-pressure-ratio (OPR) engine application. The deflection of the lift pad changes the seal geometry in a way that the features intended to create hydrodynamic lift cannot work. Specifically, the lift pad inner surface does not remain parallel to the rotor surface. Further, it appears that dynamic response of the NCFS to shaft dynamics is important to address. For applications with high pressure differentials use of hydrostatic forces to control seal clearance will likely be more effective in developing compliant, low-leakage seal designs. The modeling effort has provided understanding and insight to the challenges of designing and analyzing compliant seal designs. Continued efforts to develop noncontacting, low-leakage seal technologies for the advanced aircraft engines of the future are recommended.

References

1. Steinetz, Bruce M.; Hendricks, Robert C.; and Munson, John: Advanced Seal Technology Role in Meeting Next Generation Turbine Engine Goals. NASA/TM—1998-206961, 1998. https://ntrs.nasa.gov
2. Arora, Gul, et al.: Pressure Balanced, Low Hysteresis, Finger Seal Test Results. NASA/TM—1999-209191 (AIAA 99–2686), 1999. https://ntrs.nasa.gov
3. Arora, Gul K.; and Proctor, Margaret P.: JTAGG II Brush Seal Test Results. NASA TM–107448 (AIAA 97–2632), 1997. https://ntrs.nasa.gov
4. Arora, Gulshan K.: Noncontacting Finger Seal With Hydrodynamic Foot Portion. U.S. Patent 5,755,445, May 26, 1998.
5. Proctor, Margaret P.; and Steinetz, Bruce M.: Noncontacting Finger Seal. U.S. Patent 6,811,154 B2, Nov. 2, 2004.
6. Braun, M.J., et al.: A Three Dimensional Thermofluid Analysis and Simulation of Flow, Temperature, and Pressure Patterns in a Passive-Adaptive Compliant Finger Seal. Presented at the 10th International Symposium on Transport Phenomena and Dynamics of Rotating Machinery, Honolulu, HI, 2004, pp. 191–192.
7. Braun, Minel J., et al.: Structural and Dynamic Considerations Towards the Design of a Padded Finger Seal. AIAA 2003–4698, 2003.
8. Marie, Hazel: A Study of Non-Contacting Passive-Adaptive Turbine Finger Seal Performance. Ph.D. Dissertation, University of Akron, 2005.
9. Braun, Minel J.; Marie, Hazel; and Smith, Ian: Double Padded Finger Seal. U.S. Patent 7,735,833 B2, June 15, 2010.

10. Proctor, Margaret P.; and Delgado, Irebert R.: Preliminary Test Results of a Non-Contacting Finger Seal on a Herringbone-Grooved Rotor. NASA/TM—2008-215475 (AIAA 2008–4506), 2008. https://ntrs.nasa.gov
11. Proctor, Margaret P., et al.: Comparison of Performance Test Results to CFD and Structural Models of Non-Contacting Finger Seals. Presented at the 2018 STLE Annual Meeting and Exhibition, Minneapolis, MN, 2018. https://ntrs.nasa.gov
12. Proctor, Margaret P.: Non-Contacting Finger Seals Static Performance Test Results at Ambient and High Temperatures. AIAA 2016–4921, 2016.
13. Coskun, M. Bulut; Askoy, Serdar; and Aksit, Mahmut F.: Friction and Wear Characteristics of Haynes 25, 188, and 214 Superalloys Against Hastelloy X up to 540 °C. Tribol. Lett., vol. 45, 2012, pp. 497–503.